Diss. ETH No. xxxxx

Numerical simulations of bosons and fermions in three dimensional optical lattices

A dissertation submitted to

ETH ZURICH

for the degree of

Doctor of Sciences

presented by

Ping Nang Ma

M.Phil., Hong Kong University
born 27.05.1982

citizen of
Hong Kong

accepted on the recommendation of

Prof. Dr. M. Troyer, examiner
Prof. Dr. L. Pollet, co-examiner

2013

For my loved one, Yangyang

學海無涯，回頭是岸。

Abstract

The quest for new exotic materials lies in our theoretical understanding of strong correlations, which could only be sought via quantum emulators at large scale. Optical lattices, being clean and easily tunable, become natural candidates. This thesis is regarding numerical simulations of bosons and fermions in 3D optical lattices, which bridges the theory to the relevant experiments today as well as in the near future. The first part is devoted to the various thermometry schemes which are made possible due to the state-of-art probing techniques in experiments. These schemes are quantitatively tested in this thesis to give realiable estimates of the thermodynamic temperature even in the presence of different experimental imperfections, therefore proving itself to be a feasible standard thermometer for bosonic optical lattices. The second part is about the robust implementation of the QMC directed worm algorithm capable of scaling up to some 10 million sites with any lattice geometry, of which some manage to converge in merely a couple of hours. The current version is in fact one of the fastest, if not the fastest, in the world till date, specially designed for the needs of future experiments which will involve bigger bosonic clouds beyond parabolic trapping. Large-scale simulations involving large datasets are flexibly supported with chain automations in this new version. The third part illustrates the use of density functional theory for fermionic shallow optical lattices. We find that Stoner ferromagnetism, which was recently discovered to exist in fermionic gases, gets stablized by the optical lattice due to band structure effects. At half-filling in the Hubbard model limit, the antiferromagnetic phase is recovered by density functional theory with the presence of a spin-density-wave gap that could be an indirect probe for antiferromagnetism in future experiments. As a whole, the numerical simulations in this thesis are performed as numerically exact as possible, at least in some limit, with minimal assumptions, so as to ensure that our results here will remain relavant to both theoreticans and experimentalists in the coming future.

Zusammenfassung

Die Suche nach neuen exotischen Materialien liegt in unserem theoretischen Verständnis starker Korrelationen, die nur über Quanten-Emulatoren hoher Größenordnung angestrebt werden konnten. Optische Gitter sind natürliche Kandidaten, da sie geordnet und leicht kontrollierbar sind. Diese Thesis betrachtet numerische Simulationen von Bosonen und Fermionen in 3D optischen Gittern, und schlägt eine Brücke zwischen Theorie und sowohl heute als auch in der nahen Zukunft relevanter Experimente. Der erste Teil ist den zahlreichen Methoden der Temperaturmessung gewidmet, die durch die momentanen Techniken in Experimenten möglich gemacht werden. Diese Methoden werden in dieser Thesis quantitativ darauf getestet, ob sie insbesondere in Gegenwart verschiedener experimenteller Imperfektionen verlässliche Abschätzungen der thermodynamischen Temperatur liefern, und sich somit als Kandidaten für Standard-Thermometer bosonischer optischer Gitter erweisen. Der zweite Teil befasst sich mit der robusten Implementierung des QMC bestimmten Wurm-Algorithmus, mit der bei jeder Gittergeometrie auf einige 10 Millionen Gitterplätze hochskaliert werden kann, wobei einige bereits innerhalb weniger Stunden konvergieren. Die momentane Version ist tatsächlich eine der schnellsten Implementierungen der Welt bis heute, wenn nicht die schnellste, und ist speziell entworfen um den Bedürfnissen zukünftiger Experimente, die größere, über parabolisches trapping hinausgehende bosonische clouds beinhalten, gerecht zu werden. In dieser neuen Version werden large-scale Simulationen mit großen Datenmengen durch Kettenautomatisierungen flexibel unterstützt. Der dritte Teil zeigt den Nutzen von DFT für fermionische flache optische Gitter. Wir zeigen, dass der Stoner Ferromagnetismus, der vor kurzem in fernionischen Gasen entdeckt wurde, durch das optische Gitter aufgrund von Bandstruktureffekten stabilisiert wird. Bei half-filling im Limit des Hubbard Modells erreicht man wieder die Antiferromagnetische Phase durch DFT mit der Anwesenheit einer Spin-density-wave Lücke, was ein indirekter Test für Antiferromagnetismus in zukünftigen Experimenten sein könnte. Im Großen und Ganzen sind die numerischen Simulationen in dieser Arbeit so numerisch exakt wie möglich durchgeführt, zumindest in einem gewissen Limit, mit minimalen Annahmen, um so sicherzustellen, dass unsere Ergebnisse hier sowohl für Theoretiker als auch für

Experimentatoren in der näheren Zukunft relevant bleiben.

Contents

Chapter 1

Introduction

1.1 Birth of a quantum era

The entire human civilization was brought to believe that nature were certain and deterministic prior the 20^{th} century. This belief is in fact the principle behind Newtonian classical mechanics [1], which lays the foundation of the tallest architecture and the fastest bullet train on Earth. Further evidence for the belief came in 1861-2 when James Clerk Maxwell unified classical electromagnetism under his four Maxwell equations [2]. At that time, science and technology could all be explained by classical mechanics. Its extraordinary beauty had in fact blinded many scientists up to the mid-twentieth century, including the mighty Albert Einstein who once made the following comment.

> "God does not play dice with the universe."
>
> — Albert Einstein, *The Born-Einstein Letters 1916-55*

The beginning of the 20^{th} century marked a revolutionary period among the scientific community, where a series of microscopic experiments[1], one after another, failed to comply by the law of classical mechanics. [3] Evidence provided by these experiments slowly convinced some scientists at that time that all microscopic particles are waves. In 1926, Erwin Schrdingier formulated the wave interpretation of quantum mechanics by the proposal of his Schrödingier equation [4]

$$i\hbar\frac{\partial}{\partial t}\psi(\mathbf{x},t) = \left(-\frac{\hbar^2}{2m}\nabla^2 + V(\mathbf{x},t)\right)\psi(\mathbf{x},t) \tag{1.1}$$

[1] Classical mechanics became inadequate in explaining a series of microscopic experiments. Some examples include the black-body radiation, the photoelectric effect, the Compton effect, the discretization of atomic energy spectra, and the quantization of angular momentum. [3]

that dictates the particle wavefunction $\psi(\mathbf{x}, t)$ in the presence of an external potential $V(\mathbf{x}, t)$. In the same year, Max Born proposed a probabilistic interpretation for $|\psi(\mathbf{x}, t)|^2$ [5], such that the underlying microscopic particle could never be located with certainty at any spatial position in general. Surprisingly, nature reveals itself to be stochastic and unpredictable at the microscopic level, and all subsequent experiments prove quantum mechanics to be fundamentally correct. Other remarkable scientists, who had greatly contributed to the development of quantum mechanics, include Werner Heisenberg, Paul Dirac, and Richard Feynmann.

> " ... nobody understands quantum mechanics."
>
> — Richard Feynmann, *The Character of Physical Law 1965*

Quantum mechanics exhibits many peculiar phenomenons that are not easily understood. Microscopically, the wave nature of particles makes them identical or indistinguishable, leading the many-body wavefunction to be either symmetric or antisymmetric under particle permutation [6]. As a consequence, identical particles could either behave like bosons exhibiting symmetric statistics [7], or fermions exhibiting antisymmetric statistics [8, 9]. In fact, bosons and fermions are the only two types of particles that exist in nature. Their statistical effects give rise to many new phases of matter, like superfluidity and antiferromagnetism [10]. After a century, quantum mechanics has become the fundamental pillar of all modern technology today.

1.2 Quantum engineering of materials

The modern description of solids came in 1928 when Felix Bloch invented the electronic band theory for crystals based on lattice translational symmetries in quantum mechanics [11]. A remarkable consequence is the classification of semiconductor materials characterized by a finite band gap of the order of a few eV, distinct from either a conductor or an insultor [12]. The historical moment came in 1947 when Bardeen, Shockley, and Brattain invented the first germanium-based semiconductor point contact npn-transistor that marked the beginning of the robust semiconductor industry [13]. Today, we are in a nanotechnology era, whereby modern commercial transistors size about 45 nm in size, and modern graphic cards have over 3 billion transistors beautifully engineered as integrated circuits [14]. Excitingly, researchers have been successful in creating new exotic transistors which are based on carbon nanotubes in 1998 [15], and biomolecules like DNA, RNA, proteins in 2013 [16]. The theoretical description of these conventional materials is completely known from Kohn-Sham density functional theory [17], including higher-order diagrammatic corrections [18]. Its success enables scientists to make

accurate predictions of new semiconductor and biological materials.

An entirely different class of strongly correlated materials exists in nature which yields fascinatingly captivating properties beyond those merely from conventional materials. These materials are derived from transition metals or/ and rare earth metals, having incompletely filled d- or f- electron orbitals respectively with narrow energy bands [19]. Typical examples include 1) ferromagnetic materials such as nickel Ni, cobalt Co, and iron Fe; 2) ferrimagnetic materials such as hematite Fe_2O_3, and yttrium iron garnet $Y_3Fe_2(FeO_4)_3$; and 3) antiferromagnetic materials such as chromium Cr, and nickel oxide NiO. [20] Of particular engineering interest lies probably in the high temperature cuprate superconductors that exhibit zero electrical resistivity when cooled below some particular transition temperature T_c [19]. Since its first discovery by Bednorz and Müller in 1986 [21], subsequent discoveries have revealed unconventional superconductivity up to a temperature of 133K in mercury-barium-calcium-based cuprates $HgBa_2Ca_2Cu_3O_8$ [22]. Unconventional superconductivity has also been recently found in iron pnictides [23] which is another class of strongly correlated materials.

The physics of strongly correlated materials remains theoretically uncertain after many decades since their discoveries. The inadequency of the single-electron picture makes density functional theory alone unsuitable for studying strongly correlated materials qualitatively. Instead, physicists turn to toy models and hope that they could capture most of the essential physics of strongly correlated materials. Unfortuantely, the Hubbard model [24]

$$\hat{H} = -t \sum_{\langle i,j\rangle,\sigma} \hat{c}^{\dagger}_{i\sigma}\hat{c}_{j\sigma} + U \sum_{i} n_{i\uparrow}n_{i\downarrow} \ , \tag{1.2}$$

having been believed to capture unconventional superconductivity in doped cuprates for instance, turns out to be too challenging for the most powerful machines to be solved numerical exactly via Quantum Monte Carlo methods due to the notorious sign problem till today. As a consequence, there exists no quantitative phase diagram for the Hubbard model to be directly compared with experiments, therefore seriously handicapping our understanding towards these materials, needless to mention further about prediction and engineering. Recently, optical lattices have been proposed to be alternative quantum emulators [25], in hoping that they could solve such quantum models and bring greater insights to strongly correlated materials.

1.3 Optical lattice as a quantum emulator

1.3.1 Optical lattice

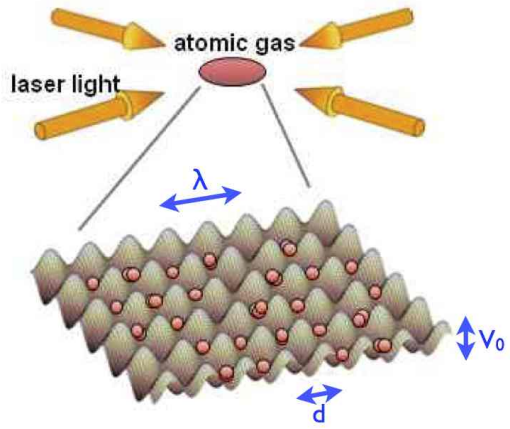

Figure 1.1: Atomic gases in a 2D optical lattice. Counter-propagating laser light form a standing wave, or an optical lattice, due to wave interference effect. The lattice intensity is V_0, the wavelength λ and thus spacing $d = \lambda/2$. *This figure is modified from its original version, courtesy of M. Yamashita.*[26].

The physics of wave interference, generated by counter-propagating laser light, dictates the presence of a standing wave. [27] The environment of standing waves is called an optical lattice with intensity V_0 and spacing $d = \frac{\lambda}{2}$, which is conceptually illustrated in figure 1.1. For instance, the potential of an isotropic 3D optical lattice reads

$$V(\mathbf{x}) = \sum_{x^i=x,y,z} V_0 \sin^2(kx^i) \tag{1.3}$$

with wavevector $k = \frac{2\pi}{\lambda} = \frac{\pi}{d}$ [28]. In addition, quantum particles in an optical lattice have to be confined by a trapping potential $V_T(\mathbf{x})$, otherwise they would fly apart. In the Greiner experiment, the confinement has been realised with a tight Gaussian laser focus, as schematically illustrated by figure 1.2. Here, the 3D optical lattice is radially confined by the trapping envelope

$$V_0 \exp\left(-\frac{2r^2}{w_0^2}\right) \tag{1.4}$$

of waist (or $1/e^2$-radius) w_0 [28]. Particles in current experiments are trapped in

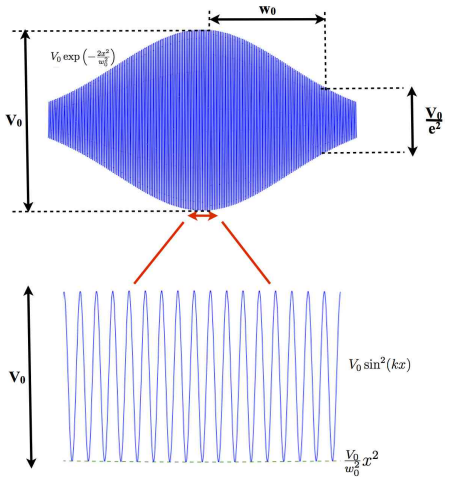

Figure 1.2: Schematic illustration of the Gaussian confinement of bosons.[28] Top: A pair of counter-propagating laser beams interfere in the x-direction to form an enveloped standing wave of intensity V_0, with trapping envelope of waist w_0. Bottom: Near the centre, the optical potential is almost uniformly periodic, i.e. $V_0 \sin^2(kx)$, with an additional parabolic trapping term $\frac{V_0}{w_0^2}x^2$.

the vicinity close to the center of the gaussian trap, therefore effectively confined by the first order parabolic trapping term. Taking into account also all other parabolic trapping, the trapping potential can be effectively written as

$$V_T(\mathbf{x}) = V_T \mathbf{x}^2 \tag{1.5}$$

where V_T is the strength of the parabolic trapping.

1.3.2 Single particle in an optical lattice

To better conceptualise the physics, let us hypothetically consider a single particle of mass m in an optical lattice. Within non-relativisitic regime, its quantum mechanical nature is captured by the Schrdingier equation in reciprocal space $\hat{H}_{\mathbf{k}} u_{\mathbf{k}} = E_{\mathbf{k}} u_{\mathbf{k}}$. [29] Due to the periodicity of the optical lattice, the Bloch Hamiltonian is given by

$$\hat{H} = \frac{\hbar^2}{2m} \left(-i\nabla + \mathbf{k}\right)^2 + V(\mathbf{x}) \ , \tag{1.6}$$

where the $\mathbf{k}$-points in reciprocal space take values depending individually on different lattice geometries. Figure 1.3 illustrates the energy band structure $E_{\mathbf{k}}$ of an optical lattice, where one could clearly observe the opening of a energy band gap

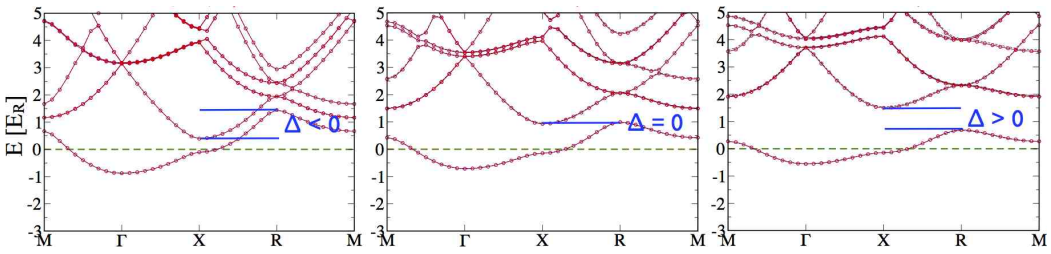

Figure 1.3: Single particle energy band structure $E_{\mathbf{k}}$ of a simple cubic lattice. Energy band gap Δ opens up with increasing lattice intensity V_0, i.e. from $1.0E_R$ (left), to $2.2E_R$ (centre), and finally $3.4E_R$ (right). Here, the high-symmetry $\mathbf{k}$-points of a simple cubic lattice are namely $\Gamma(0,0,0)$, $X(\frac{\pi}{d},0,0)$, $M(\frac{\pi}{d},\frac{\pi}{d},0)$ and $R(\frac{\pi}{d},\frac{\pi}{d},\frac{\pi}{d})$. In addition, energy is expressed in units of recoil energy $E_R = \frac{h^2}{2m\lambda^2}$. Typically, for a Rb-87 particle in an optical lattice with $\lambda = 800nm$, the recoil energy is $E_R = 172nK$.

Δ as the shallow lattice (small V_0) becomes deep (large V_0).

In the limit of larger V_0 such that $\Delta \gg k_B T$ where T is the thermodynamical temperature, only the ground state band becomes relevant. By taking the Fourier transform of ground state Bloch functions $u^{(0)}_{\mathbf{k}}(\mathbf{x})$, i.e.

$$w(\mathbf{x}-\mathbf{x}_i) = \frac{1}{\sqrt{\Omega}} \sum_{\mathbf{k}} u^{(0)}_{\mathbf{k}}(\mathbf{x}) e^{i\mathbf{k}\cdot(\mathbf{x}-\mathbf{x}_i)} \ , \tag{1.7}$$

where Ω is the volume of the primitive unit cell, we obtain an orthonormal basis of Wannier functions $\{w(\mathbf{x}-\mathbf{x}_i)\}$ that are maximally localized at every individual lattice site. [38] Next, we define the hopping strength of a particle from site i to j as

$$t_{ij} = -\int d\mathbf{x}\, w(\mathbf{x}-\mathbf{x}_i) \left(-\frac{\hbar^2}{2m}\nabla^2 + V(\mathbf{x}) \right) w(\mathbf{x}-\mathbf{x}_j) \tag{1.8}$$

and the onsite energy $\epsilon_i = t_{ii}$. Often, only the hopping strength between nearest neighbouring sites is relevant to the physics, and is simply denoted by t for the case of homogeneous lattice. Two identical particles in an optical lattice interact through short-range potential, hereby modelled by contact interaction in real space, i.e.

$$U(\mathbf{x},\mathbf{x}') = \frac{4\pi a_s \hbar^2}{m} \delta(\mathbf{x},\mathbf{x}') \ , \tag{1.9}$$

where the scattering mechanism is effectively described by the s-wave scattering length a_s, which can be easily tuneable in experiments via Feshbach resonance

technique. [28, 31] Next, we define interaction strength among site i, j, k, l as

$$U_{ijkl} = \frac{4\pi a_s \hbar^2}{m} \int d\mathbf{x}\, w(\mathbf{x}-\mathbf{x}_i)\, w(\mathbf{x}-\mathbf{x}_j)\, w(\mathbf{x}-\mathbf{x}_l)\, w(\mathbf{x}-\mathbf{x}_k)\ . \tag{1.10}$$

Often, only the onsite interaction strength is relevant to the physics, and is simply denoted by U for the case of homogeneous lattice.

1.3.3 Bosons in an optical lattice

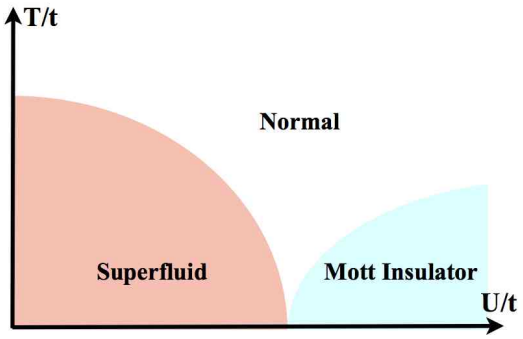

Figure 1.4: Phases of boson Hubbard model for 3D lattices. [32] At lower temperatures T/t, an homogeneous bosonic optical lattice exhibits superfluid (Mott insulator) phase in the limit of small (large) interaction U/t. At higher temperatures T/t, the system becomes normal fluid.

The hamiltonian for single-component bosons in an optical lattice is

$$\hat{H} = \int d\mathbf{x}\, \hat{\psi}^\dagger(\mathbf{x}) \left(-\frac{\hbar^2}{2m}\nabla^2 + V(\mathbf{x}) \right) \hat{\psi}(\mathbf{x}) + \frac{1}{2} \int d\mathbf{x}\, d\mathbf{x}' \hat{\psi}^\dagger(\mathbf{x}) \hat{\psi}^\dagger(\mathbf{x}')\, U(\mathbf{x},\mathbf{x}')\, \hat{\psi}(\mathbf{x}') \hat{\psi}(\mathbf{x}) \tag{1.11}$$

where the field operators

$$\hat{\psi}(\mathbf{x}) = \sum_i w(\mathbf{x}-\mathbf{x}_i)\, \hat{b}_i \tag{1.12}$$

are expanded in the wannier basis $\{w(\mathbf{x}-\mathbf{x}_i)\}$ for every site i in the optical lattice [6]. Here, $\hat{b}_i$ and $\hat{b}_i^\dagger$ are annihilation and creation operators respectively at site i that satisfy the following commutation relations

$$[\hat{b}_i, \hat{b}_j] = 0 \quad , \quad [\hat{b}_i^\dagger, \hat{b}_j^\dagger] = 0 \quad , \quad [\hat{b}_i, \hat{b}_j^\dagger] = \delta_{ij}\ . \tag{1.13}$$

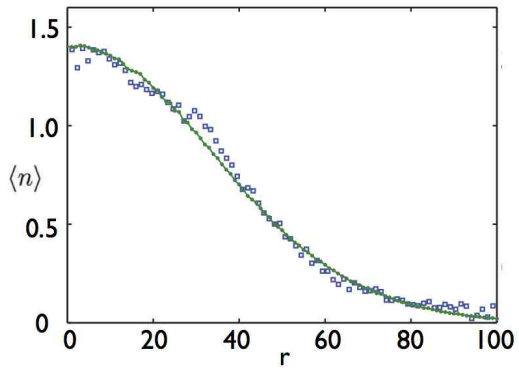

Figure 1.5: Comparison between theory and experiment. Average density profile $\langle n \rangle$ with respect to radial distance r in units of lattice spacing d. Blue dots - optical lattice experiment[31]: 9400 Cs-133 bosons are confined in a 2D square optical lattice with intensity $V_0 = 5E_R$ and trapping strength $V_T = 0.01nK$. Band structure calculations give the hopping strength $t = 4.18nK$ and onsite repulsion strength $U = 10.79nK$. Red line - numerical-exact Quantum Monte Carlo simulation[37]: Single-band boson Hubbard model with interaction $U/t = 2.58$, temperature $T/t = 5.98$ and trapping strength $V_T/t = 0.00239$, thereby exhibiting normal-fluid phase. An excellent agreement has been observed.

In the limit of deep lattice (large V_0), the bosonic homogeneous optical lattice 1.11 can be effectively mapped to the boson Hubbard model [34]

$$\hat{H} - \mu\hat{N} = -t\sum_{\langle i,j \rangle} \hat{b}_i^\dagger \hat{b}_j + \frac{U}{2}\sum_i n_i(n_i - 1) - \mu\sum_i n_i \tag{1.14}$$

where the summation $\langle i, j \rangle$ extends over all nearest neighbouring lattice sites, and the chemical potential μ determines the total number of bosons in the system. The boson Hubbard model 1.14 has been completely solved at least numerically [32], with its phase diagram illustrated in figure 1.4 for different interactions U/t and temperatures T/t. The first indirect evidence of a superfluid-insulator phase transition was derived from the time-of-flight images obtained from the experiment by M. Greiner *et al* in 2002 [33], which had been numerically confirmed by Quantum Monte Carlo simulations 7 years later [32]. Recent experimental advancement has enabled density probing within single-site resolution, [35, 36] and quantitative agreement has been found in the direct comparison between theory and experiment as illustrated in figure 1.5.

In the presence of parabolic trapping, the trapped boson Hubbard hamiltonian [38] reads

$$\hat{H} = -t \sum_{\langle i,j \rangle} \hat{b}_i^\dagger \hat{b}_j + \frac{U}{2} \sum_i n_i(n_i - 1) - \sum_i (\mu - V_T \mathbf{x}_i^2) n_i \ . \tag{1.15}$$

1.3.4 Fermions in an optical lattice

The hamiltonian for 2-component fermions in an optical lattice is

$$\begin{aligned} \hat{H} \ = \ & \sum_{\sigma=\uparrow,\downarrow} \int d\mathbf{x}\, \hat{\psi}_\sigma^\dagger(\mathbf{x}) \left(-\frac{\hbar^2}{2m} \nabla^2 + V(\mathbf{x}) \right) \hat{\psi}_\sigma(\mathbf{x}) \\ & + \frac{1}{2} \sum_{\sigma,\sigma'=\uparrow,\downarrow} \int d\mathbf{x}\, d\mathbf{x}' \hat{\psi}_\sigma^\dagger(\mathbf{x}) \hat{\psi}_{\sigma'}^\dagger(\mathbf{x}')\, U(\mathbf{x},\mathbf{x}')\, \hat{\psi}_{\sigma'}(\mathbf{x}') \hat{\psi}_\sigma(\mathbf{x}) \end{aligned} \tag{1.16}$$

where the field operators

$$\hat{\psi}(\mathbf{x}) = \sum_i w(\mathbf{x} - \mathbf{x}_i)\, \hat{c}_i \tag{1.17}$$

are expanded in the wannier basis $\{w(\mathbf{x}-\mathbf{x}_i)\}$ for every site i in the optical lattice [6]. Here, $\hat{c}_i$ and $\hat{c}_i^\dagger$ are annihilation and creation operators respectively at site i that satisfy the following anti-commutation relations

$$\{\hat{c}_i, \hat{c}_j\} = 0 \quad , \quad \{\hat{c}_i^\dagger, \hat{c}_j^\dagger\} = 0 \quad , \quad \{\hat{c}_i, \hat{c}_j^\dagger\} = \delta_{ij} \ . \tag{1.18}$$

In the limit of deep lattice (large V_0), the fermionic homogeneous optical lattice 1.16 can be effectively mapped to the Hubbard model [24]

$$\hat{H} = -t \sum_{\langle i,j \rangle, \sigma} \hat{c}_{i\sigma}^\dagger \hat{c}_{j\sigma} + U \sum_i n_{i\uparrow} n_{i\downarrow} \tag{1.2}$$

where the summation $\langle i, j \rangle$ extends over all nearest neighbouring lattice sites, and $\sigma = \uparrow, \downarrow$. Unlike the bosonic case, the Hubbard model 1.2, being the simplest correlation model for fermions, remains generally unsolved till today. Only for specific cases like half-filling ($\langle n \rangle = 1$) could the Hubbard model 1.2 be solved exact numerically via Quantum Monte Carlo methods [39]. At half-filling towards larger interaction U/t, the Hubbard model is driven from the Mott insulating phase to the antiferromagnetic phase with decreasing temperature T/t [39]. Unfortunately, this cannot yet be confirmed by current experiments, due to tough challenges in cooling the fermionic optical lattice system beyond the Neel temperature [40].

Away from half-filling is perhaps where the Hubbard model 1.2 is being the most interesting with the conjecture of a superconductivity phase at low temperature. With a belief of relevance to unconventional superconductivity, the Hubbard model is probably one of the many scientific puzzles that remains urgently to be solved. Numerically, the notorious negative-sign problem forbids the use of Quantum Monte Carlo methods, which then brings up the interest of designing fermionic optical lattices to be quantum emulators of the Hubbard model [25].

Chapter 2

Quantum Monte Carlo

This chapter introduces an efficient Quantum Monte Carlo method [41], implemented via the directed worm algorithm [42], that is used to solve the boson Hubbard model 1.14 exact numerically at finite temperature.

2.1 Quantum statistical mechanics

2.1.1 Feynman path-integral formalism

Rewriting the boson Hubbard hamiltonian 1.14 as $\hat{H} - \mu\hat{N} = \hat{H}_0 - \hat{V}$ such that

$$\hat{H}_0 = \frac{U}{2}\sum_i n_i(n_i - 1) - \sum_i \mu_i n_i \tag{2.1}$$

$$\hat{V} = t\sum_{\langle i,j\rangle} \hat{b}_i^\dagger \hat{b}_j \ , \tag{2.2}$$

the equation of motion for the evolution operator $\hat{U}(\tau, \tau_0)$ becomes

$$\frac{\partial}{\partial\tau}\hat{U}(\tau, \tau_0) = \hat{V}(\tau)\hat{U}(\tau, \tau_0) \tag{2.3}$$

in the interaction picture, taking $\hbar = 1$ [43]. With

$$\hat{U}(\tau, \tau_0) = e^{\hat{H}_0\tau}\, e^{-\hat{H}(\tau-\tau_0)}\, e^{-\hat{H}_0\tau_0} \tag{2.4}$$

$$\hat{V}(\tau) = e^{\hat{H}_0\tau}\, \hat{V}\, e^{-\hat{H}_0\tau} \ , \tag{2.5}$$

equation (2.3) becomes

$$\hat{U}(\tau, \tau_0) - \hat{U}(\tau_0, \tau_0) = \int_{\tau_0}^{\tau} d\tau_1 \hat{V}(\tau_1)\hat{U}(\tau_1, \tau_0) \tag{2.6}$$

or ($\tau = \beta$, $\tau_0 = 0$),

$$\begin{aligned} \hat{U}(\beta) &= 1 + \int_0^\beta d\tau_1 \hat{V}(\tau_1)\hat{U}(\tau_1) \\ &= 1 + \int_0^\beta d\tau_1\, \hat{V}(\tau_1) + \int_0^\beta d\tau_1 \int_0^{\tau_1} d\tau_2\, \hat{V}(\tau_1)\hat{V}(\tau_2) + \cdots \end{aligned} \tag{2.7}$$

According to equation (2.4), we have $\hat{U}(\beta) = e^{\beta\hat{H}_0}\, e^{-\beta\hat{H}}$, thus the partition function

$$Z = \operatorname{Tr} e^{-\beta\hat{H}} = \operatorname{Tr} e^{-\beta\hat{H}_0}\, \hat{U}(\beta) \tag{2.8}$$

In Fock basis $\{|i\rangle\}$, the partition function can be written as

$$Z = \sum_{m=0}^{\infty} \sum_{i_1 \cdots i_m} e^{-\beta\epsilon_1} \int_0^\beta d\tau_1 \cdots \int_0^{\tau_{m-1}} d\tau_m \left(e^{-\tau_1\epsilon_1}\, V_{i_1 i_2}\, e^{\tau_1\epsilon_2}\right) \cdots \left(e^{-\tau_m\epsilon_m}\, V_{i_m i_1}\, e^{\tau_m\epsilon_1}\right) \tag{2.9}$$

where $\hat{H}_0|i\rangle = \epsilon_i|i\rangle$ and $V_{ij} = \langle i|\hat{V}|j\rangle$.

2.1.2 Configuration and worldlines diagram

The integrand of the partition function Z in equation 2.9 is uniquely determined if the *configuration* $\mathcal{C} = \{m,\, i_1 \cdots i_m\,,\, \tau_1 \cdots \tau_m \,|0 < \tau_1 < \cdots < \tau_m < \beta\}$ is known. Defining the configuration weight

$$Z(\mathcal{C}) = e^{-\beta\epsilon_1} \left(e^{-\tau_1\epsilon_1}\, V_{i_1 i_2}\, e^{\tau_1\epsilon_2}\right) \cdots \left(e^{-\tau_m\epsilon_m}\, V_{i_m i_1}\, e^{\tau_m\epsilon_1}\right)\ , \tag{2.10}$$

we have now a simpler notation

$$Z = \sum_{\mathcal{C}} Z(\mathcal{C}) \tag{2.11}$$

$$\langle\mathcal{O}\rangle = \frac{1}{Z}\sum_{\mathcal{C}} \mathcal{O}(\mathcal{C}) Z(\mathcal{C}) \tag{2.12}$$

for diagonal observables $\langle\mathcal{O}\rangle = \frac{1}{Z}\operatorname{Tr}\hat{\mathcal{O}}e^{-\beta\hat{H}}$ [41]. Here, $\mathcal{O}(\mathcal{C})$ is called the measurement of $\hat{\mathcal{O}}$ for configuration $\mathcal{C}$. In practice, configurations are visualized as worldlines diagrams. Figure 2.1.2 illustates an example of a worldlines diagram that corresponds to the configuration $\mathcal{C} = \{m = 8\,;\, i_1 \cdots i_8\,;\, \tau_1 \cdots \tau_8 \,|\, 0 < \tau_1 < \cdots < \tau_8 < \beta\}$. In this example,

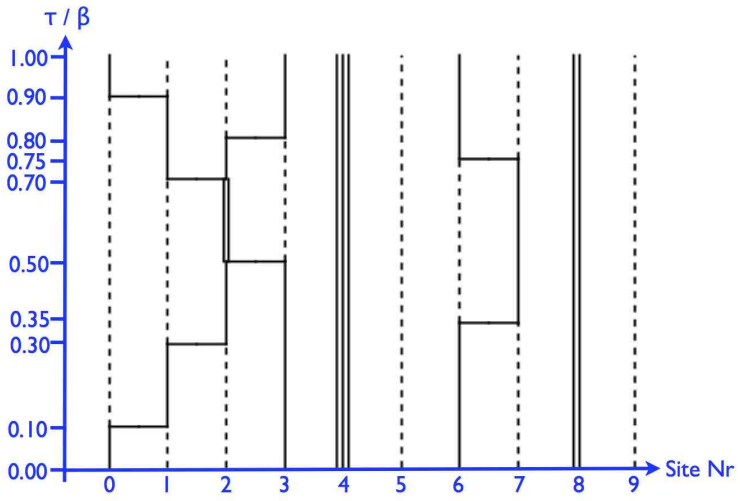

Figure 2.1: Example of a worldlines diagram of 1D boson Hubbard model with 10 sites. Horizontal axis: Site number $0, \cdots, 9$. Vertical axis: Imaginary time $\tau/\beta \in [0, 1)$ periodic. Dotted line: 0 particle; Solid line: 1 particle; Double solid line: 2 particles; Triple solid line: 3 particles. In this example, we set $t = 1$, $U = 4$, $\mu_0 = \cdots \mu_9 = 0$, $\beta = 2$.

1. $\forall\, i, \tau \in \mathcal{C}$, we have

$$\begin{aligned}
\tau_1/\beta = 0.10 \quad &: |i_1\rangle = |0,1,0,1,3,0,1,0,2,0\rangle \quad ; \epsilon_1 = 16 \\
\tau_2/\beta = 0.30 \quad &: |i_2\rangle = |0,0,1,1,3,0,1,0,2,0\rangle \quad ; \epsilon_2 = 16 \\
\tau_3/\beta = 0.35 \quad &: |i_3\rangle = |0,0,1,1,3,0,0,1,2,0\rangle \quad ; \epsilon_3 = 16 \\
\tau_4/\beta = 0.50 \quad &: |i_4\rangle = |0,0,2,0,3,0,0,1,2,0\rangle \quad ; \epsilon_4 = 20 \\
\tau_5/\beta = 0.70 \quad &: |i_5\rangle = |0,1,1,0,3,0,0,1,2,0\rangle \quad ; \epsilon_5 = 16 \\
\tau_6/\beta = 0.75 \quad &: |i_6\rangle = |0,1,1,0,3,0,1,0,2,0\rangle \quad ; \epsilon_6 = 16 \\
\tau_7/\beta = 0.80 \quad &: |i_7\rangle = |0,1,0,1,3,0,1,0,2,0\rangle \quad ; \epsilon_7 = 16 \\
\tau_8/\beta = 0.90 \quad &: |i_8\rangle = |1,0,0,1,3,0,1,0,2,0\rangle \quad ; \epsilon_8 = 16
\end{aligned}$$

2. $\forall\, i \in \mathcal{C}$, we have

$$\begin{aligned}
&V_{i_1 i_2} = 1\ ,\ V_{i_2 i_3} = 1\ ,\ V_{i_3 i_4} = 1\ ,\ V_{i_4 i_5} = \sqrt{2} \\
&V_{i_5 i_6} = \sqrt{2}\ ,\ V_{i_6 i_7} = 1\ ,\ V_{i_7 i_8} = 1\ ,\ V_{i_8 i_1} = 1
\end{aligned}$$

3. For some diagonal observables $\mathcal{O}$, we have

$$\begin{aligned}
N \quad &: \quad N(\mathcal{C}) = 8 \\
E_0 \quad &: \quad E_0(\mathcal{C}) = 16
\end{aligned}$$

2.2 Markov chain sampling

The whole spirit of Quantum Monte Carlo (QMC) simulation is to obtain statistics for $\langle \mathcal{O} \rangle$ in equation 2.12 through random walking in the configuration space efficiently according to some stochastic algorithm in mind. A Markov chain random walk is a sequence of configurations , i.e. $\{\mathcal{C}_1, \mathcal{C}_2, \cdots, \mathcal{C}_M\}$, such that any configuration $\mathcal{C}_{i+1}$ in the sequence is in fact derived from its parent $\mathcal{C}_i$, thus preserving memory [44]. With importance sampling in accordance to the configuration weight 2.10, the Monte Carlo estimate

$$\langle \mathcal{O} \rangle_{\mathrm{MC}} = \frac{1}{M} \sum_{i=1}^{M} \mathcal{O}_i \xrightarrow{M \to \infty} \langle \mathcal{O} \rangle$$

converges to $\langle \mathcal{O} \rangle$ with increasing statistics[1]. The stochastic algorithm which governs the Markov chain random walk does not need to be unique, so long it satisfies both the principle of ergodicity, as well as the principle of detailed balance [44]

$$\Gamma(\mathcal{C}_i \to \mathcal{C}_{i+1}) Z(\mathcal{C}_i) = \Gamma(\mathcal{C}_{i+1} \to \mathcal{C}_i) Z(\mathcal{C}_{i+1}) \ . \tag{2.13}$$

Here, the transition matrix Γ has been chosen to follow Metropolis, i.e.

$$\Gamma(\mathcal{C}_i \to \mathcal{C}_{i+1}) = \min \left\{ 1, \frac{Z(\mathcal{C}_{i+1})}{Z(\mathcal{C}_i)} \right\} \tag{2.14}$$

which satisfies detailed balance automatically [46].

Metropolis algorithm

1. From the present configuration $\mathcal{C}_i$, propose configuration $\mathcal{C}$ randomly.
2. Generate a random number $u \in [0, 1]$.
3. Accept or reject the proposal, i.e.

$$\mathcal{C}_{i+1} = \begin{cases} \mathcal{C} & , \quad u < \min \left\{ 1, \frac{Z(\mathcal{C})}{Z(\mathcal{C}_i)} \right\} \\ \mathcal{C}_i & , \quad \text{otherwise} \end{cases} \tag{2.15}$$

4. Perform a measurement every certain number of MC steps[2].

[1] This convergence is guaranteed by the law of large numbers [45].

[2] The frequency of measurements should be adjusted according to the autocorrelation time in the measurments.

2.3 Directed worm algorithm

2.3.1 Local updates and non-ergodicity

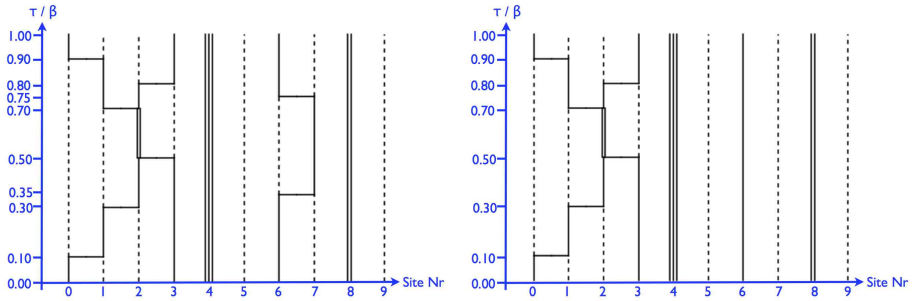

Figure 2.2: Left $\rightarrow$ ($\leftarrow$) Right : insertion (deletion) of vertices

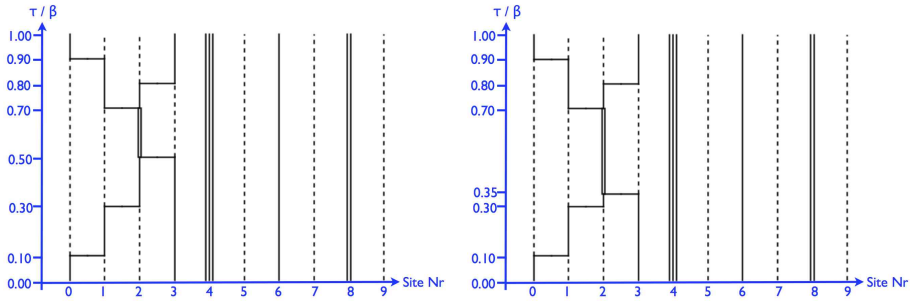

Figure 2.3: Left $\rightarrow$ ($\leftarrow$) Right : move vertex over time

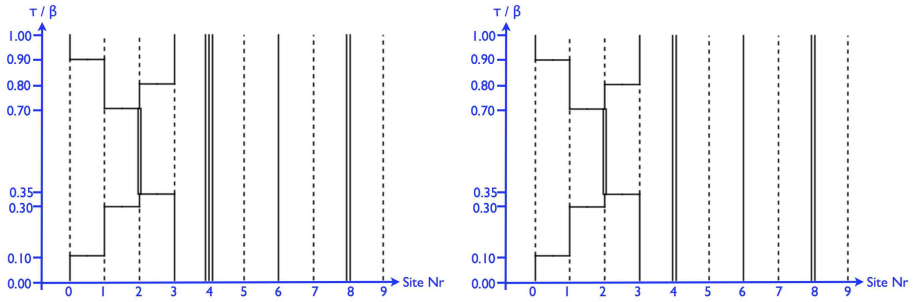

Figure 2.4: Left $\rightarrow$ ($\leftarrow$) Right : delete (insert) 1 particle

Figure 2.2, 2.3, and 2.4 illustrate some possible moves to update configurations in the Markov chain random walk. These moves result in local updates of closed worldlines that is unfortunately not universal. For instance, the Markov process is not capable of creating a particle that winds over a periodic system (i.e. horizontally from one boundary to another) starting from any configuration. Unless one can "cut" some closed lines and move these segments randomly before "joining" them eventually, the Markov process will never be ergodic with only these moves. Having realised this, Prokof'ev and Svistunov proposed the *worm algorithm* in 1998 [41], which is capable of sampling all configurations ergodically and efficiently. After nearly a decade, Pollet proposed the *directed worm algorithm* [42] which is a faster implementation compared to the original version.

2.3.2 Worms and extended configurations

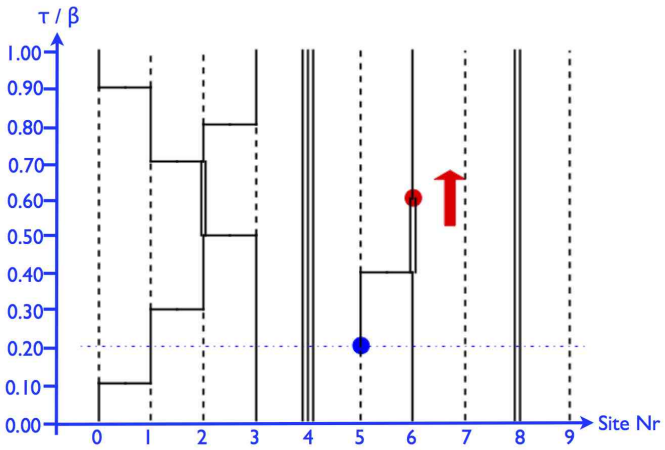

Figure 2.5: Example of an extended worldlines diagram of 1D boson Hubbard model with 10 sites. Horizontal axis: Site number $0, \cdots, 9$. Vertical axis: Imaginary time $\tau/\beta \in [0, 1)$ periodic. Dotted line: 0 particle; Solid line: 1 particle; Double solid line: 2 particles; Triple solid line: 3 particles. In this example, we set $t = 1$, $U = 4$, $\mu_0 = \cdots \mu_9 = 0$, $\beta = 2$.

An open worldline has 2 end points, called *worms* [41], as illustrated by a blue and a red dot in figure 2.5. The blue dot, called the *wormtail*, is fixed at a specific location in space-time, whereas the red dot, called the *wormhead*, moves around. In the directed worm algorithm, the wormhead moves in a specific direction until bouncing occurs. In fact, worms are either $\hat{b}(\tau_p)$ or $\hat{b}^\dagger(\tau_q)$ operators, that extend a configura-

tion to an *extended configuration* $\mathcal{E}_{pq} = \{m\,,\, i_1 \cdots i_p \cdots i_q \cdots i_m\,,\, \tau_1 \cdots \tau_p \cdots \tau_q \cdots \tau_m \,|\, 0 < \tau_1 < \cdots < \tau_p < \cdots < \tau_q < \cdots < \tau_m < \beta\}$ of m vertices at imaginary times $\tau_1 \cdots \tau_m$, and the annihilation (creation) operator at time τ_p (τ_q). The extended configuration weight is naturally defined as

$$Z(\mathcal{E}_{pq}) = e^{-\beta\epsilon_1} \left(e^{-\tau_1\epsilon_1}\, V_{i_1 i_2}\, e^{\tau_1\epsilon_2}\right) \cdots \left(e^{-\tau_p\epsilon_p}\, b_p\, e^{\tau_p\epsilon'_p}\right) \cdots \left(e^{-\tau_q\epsilon_q}\, b_q^\dagger\, e^{\tau_q\epsilon'_q}\right) \cdots \left(e^{-\tau_m\epsilon_m}\, V_{i_m i_1}\, e^{\tau_m\epsilon_1}\right) \tag{2.16}$$

which sums up to the Green's function [43] after normalization

$$\begin{aligned} G(x_p, \tau_p\,;\, x_q, \tau_q) \;=\; & \frac{1}{Z} \sum_{m=0}^{\infty} \sum_{i_1 \cdots i_m} \sum_{i_p, i_q} e^{-\beta\epsilon_1} \int_0^\beta d\tau_1 \cdots \int_0^{\tau_{m-1}} d\tau_m \\ & \times \left(e^{-\tau_1\epsilon_1}\, V_{i_1 i_2}\, e^{\tau_1\epsilon_2}\right) \cdots \\ & \times \cdots \left(e^{-\tau_p\epsilon_p}\, b_p\, e^{\tau_p\epsilon'_p}\right) \cdots \left(e^{-\tau_q\epsilon_q}\, b_q^\dagger\, e^{\tau_q\epsilon'_q}\right) \cdots \\ & \times \cdots \left(e^{-\tau_m\epsilon_m}\, V_{i_m i_1}\, e^{\tau_m\epsilon_1}\right) \end{aligned} \tag{2.17}$$

Density matrices are Green's functions at equal time, i.e.

$$\langle b_q^\dagger b_p \rangle = G(x_p, \tau\,;\, x_q, \tau)\ . \tag{2.18}$$

2.3.3 Updates in extended configuaration space

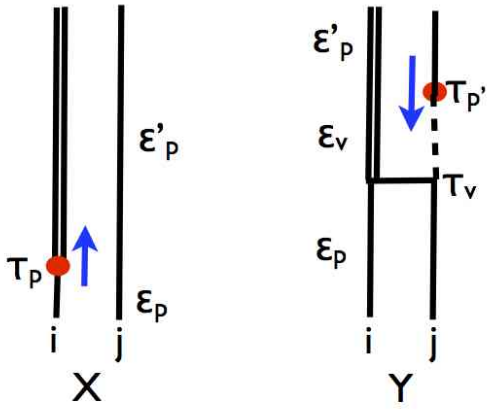

We begin studying detailed balance by looking at the movement of wormhead from extended configuration X to Y as illustrated above. From X to Y, the $\hat{b}^\dagger$ wormhead

1. moves forward in time from τ_p to τ_v unhalted,
2. jumps from site i to site j, thus creating a $\hat{b}_i^\dagger \hat{b}_j$ vertex at time τ_v,

3. moves forward in time from τ_v^+ to $\tau_{p'}$ halted.

The reverse move, from Y to X, invokes the $\hat{b}^\dagger$ wormhead to

1. move backward in time from $\tau_{p'}$ to τ_v^+ halted,
2. jump from site j to site i, thus annihilating the $\hat{b}_i^\dagger \hat{b}_j$ vertex at time τ_v,
3. move backward in time from τ_v^- to τ_p halted.

According to equation 2.16, we have

$$\frac{Z(Y)}{Z(X)} = \frac{\left(e^{-\tau_{p'}\epsilon_v}\,\langle i'_p|\hat{b}_j^\dagger|i_v\rangle\, e^{\tau_{p'}\epsilon'_p}\right)\left(e^{-\tau_v\epsilon_p}\,\langle i'_p|t\,\hat{b}_i^\dagger\hat{b}_j|i_v\rangle\, e^{\tau_v\epsilon_v}\right)}{\left(e^{-\tau_p\epsilon_p}\,\langle i'_p|\hat{b}_i^\dagger|i_p\rangle\, e^{\tau_p\epsilon'_p}\right)} \ . \tag{2.19}$$

Since $Z(X)P(X\to Y) = Z(Y)P(Y\to X)$, i.e.

$$\frac{P(X\to Y)}{P(Y\to X)} = \left(\frac{\epsilon_p\, e^{-\epsilon_p\tau_{vp}}\, e^{-\epsilon_v\tau_{p'v}}}{e^{-\epsilon'_p\tau_{p'v}}\, e^{-\epsilon'_p\tau_{vp}}}\right) \times \left(\frac{t\langle i'_p|\hat{b}_j^\dagger|i_v\rangle\langle i'_p|\hat{b}_i^\dagger\hat{b}_j|i_v\rangle}{\epsilon_p\langle i'_p|\hat{b}_i^\dagger|i_p\rangle}\right) \tag{2.20}$$

(eg. $\tau_{vp} = \tau_v - \tau_p$), what remains is simply to allocate the balanced probabilities for the sub-moves.

Unhalted move in time

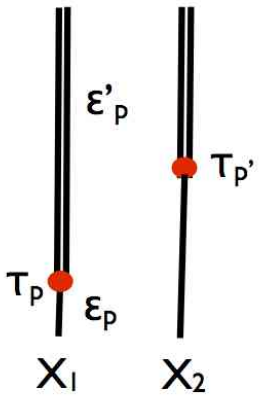

The first sub-move involves the movement of wormhead over time, as illustrated in the above figure. Here, the transition probability from extended configuration X_1 to X_2 is set as

$$P(X_1 \to X_2) = \epsilon_p e^{-\epsilon_p\tau_{p'p}} \ . \tag{2.21}$$

1. By unhalted move over time itself, it does not satisfy detailed balance. To balance it, the unhalted move must be immediately followed by an attempt to create a vertex at that new time $\tau_{p'}$. (See later section.)
2. In probability theory, the event of an attempt to create a vertex is naturally regarded as a Poisson process, a direct consequence of definition 2.21, ie. the time interval until the random new time $\tau_{p'}$ follows an exponential distribution.
3. For the transition probability to make sense, the mean occurrence of such a Poisson event is ϵ_p must be strictly positive, ie. $\epsilon_p > 0$. In implementation, the new time $\tau_{p'}$ is stochastically generated with acceptance probability 1 such that
$$\tau_{p'} - \tau_p = \tau_{p'p} = -\frac{\log(1-u)}{\epsilon_p} \tag{2.22}$$
where $u \in [0, 1)$ is an uniformly distributed random number. If $\tau_{p'} > \beta$, then $\tau_{p'}$ will be "modulus"-ed by β, i.e. $\tau_{p'} \to \tau_{p'} \,\%\, \beta$.
4. In practice, the value of ϵ_p can turn out to be enormous, when the system size gets large for instance. When this happens, the algorithm becomes very inefficient. See later section for a clever fix.

Halted move in time

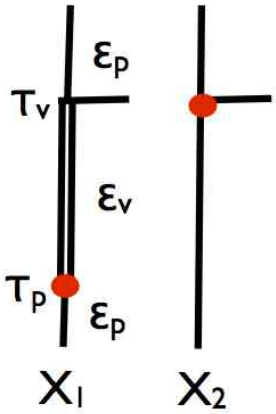

Implementing equation 2.22, a new time $\tau_{p'}$ is stochastically generated with chances that it exceeds τ_v such that $\tau_{p'} > \tau_v$ β-periodically. When that happens, the algorithm halts the wormhead just before the vertex at time τ_v^-. For the halted movement of wormhead over time, the transition probability from extended configuration X_1 to X_2 must therefore be
$$P(X_1 \to X_2) = \int_{\tau_{vp}}^{\infty} \epsilon_p \, e^{-\epsilon_p \tau_{p'p}} \, d\tau_{p'p} \tag{2.23}$$

or

$$P(X_1 \to X_2) = e^{-\epsilon_p \tau_{vp}} \tag{2.24}$$

1. By halted move over time itself, it does not satisfy detailed balance. To balance it, the halted move must be immediately followed by an attempt to delete or relink the vertex at time τ_v. (See later section.)
2. Halting of this kind only happens when the wormhead collides with a vertex of conjugate type, ie. either a $\hat{b}^\dagger$ wormhead colliding with a $\hat{b}$-vertex (in this example), or a $\hat{b}$ wormhead colliding with a $\hat{b}^\dagger$-vertex.
3. There are occasions whereby the wormhead collides with a vertex of the same type. See the following figure. When this happens, the algorithm first halts

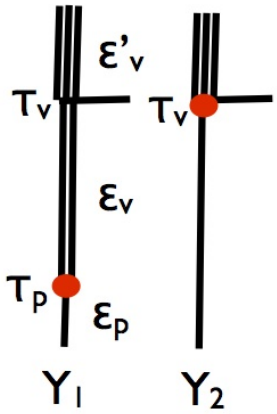

the wormhead just before the vertex at time τ_v^-. Next, the wormhead crosses the vertex with new time τ_v^+ with probability 1, which is a consequence of the commutation relations $[\hat{b}, \hat{b}] = [\hat{b}^\dagger, \hat{b}^\dagger] = 0$. Finally, a new time is stochastically generated again according to equation 2.22. Its validity will be justified in a later section.
4. An useful property of Poisson events is its *memorylessness*, ie. the event whereby the wormhead moves unhaltedly to a new time $\tau_{p'}$ is stochastically equivalent to the event whereby the wormhead first moves haltedly to an intermediate time τ_v, then moves unhaltedly to $\tau_{p'}$. One can check easily from equations 2.21 and 2.24.

Inserting, deleting, and relinking vertex

The figure below is a class of extended configurations that illustrate vertex insertion, deletion, and relinking for 1D systems. (2D and 3D are natural generalisations.) Meanwhile, note that the time interval shown on the figure from τ_v to τ_v^+

is indeed over-exaggerated only for the purpose of clarity. In fact, being at time τ_v^+, the wormhead is just infinitesimally above the vertex at time τ_v for extended configurations Y_1, Y_2. The following are the only 2 sub-moves in the algorithm

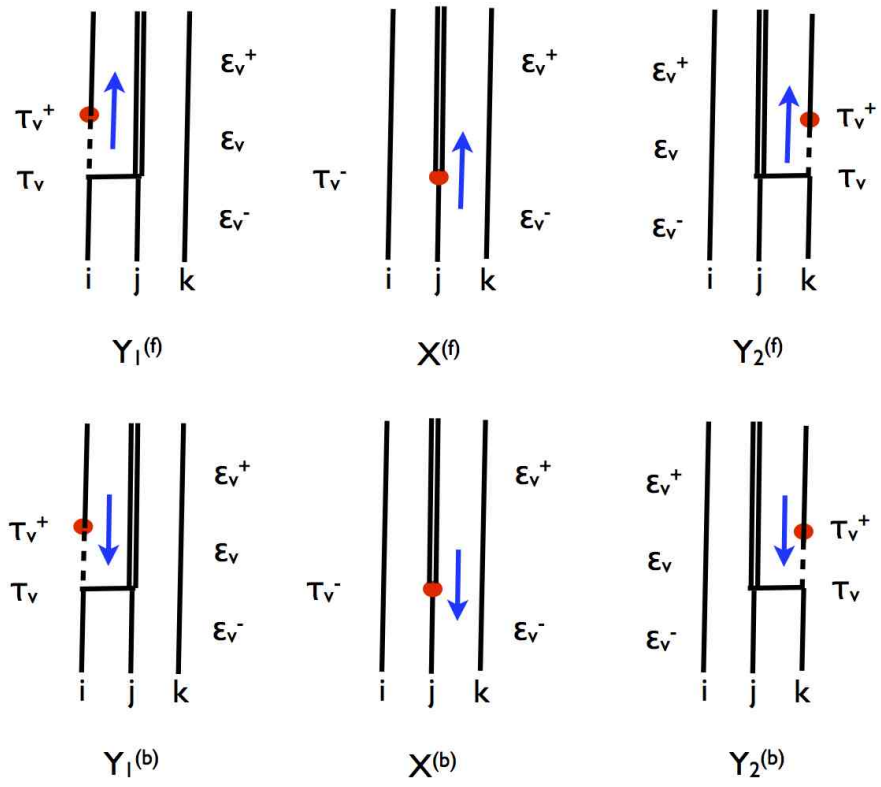

that involves an attempt to jump wormhead across sites.

1. Starting from $X^{(f)}$,
   (a) the wormhead could jump to either $Y_1^{(f)}$ or $Y_2^{(f)}$, and inserts a vertex along the way;
   (b) the wormhead could bounce, or turn around, to $X^{(b)}$.
2. Starting from $Y_1^{(b)}$,
   (a) the wormhead could jump to $X^{(b)}$, and deletes the vertex along the way;
   (b) the wormhead could jump to $Y_2^{(f)}$, and relinks the vertex along the way;
   (c) the wormhead could bounce, or turn around, to $Y_1^{(f)}$.

The algorithm fixes the following transition probabilities.

$$P(X, Y_1, Y_2 \to X) = \epsilon_{v^-} \langle i_{v^+} | \hat{b}_j^\dagger | i_{v^-} \rangle \tag{2.25}$$

$$P(X, Y_1, Y_2 \to Y_1) = t \langle i_{v^+} | \hat{b}_i^\dagger | i_v \rangle \langle i_v | \hat{b}_i \hat{b}_j^\dagger | i_{v^-} \rangle \tag{2.26}$$

$$P(X, Y_1, Y_2 \to Y_2) = t \langle i_{v^+} | \hat{b}_k^\dagger | i_v \rangle \langle i_v | \hat{b}_k \hat{b}_j^\dagger | i_{v^-} \rangle \tag{2.27}$$

To choose which of the sub-moves, one has either the choice of heatbath algorithm or Metropolis algorithm. It is the preference of the author to choose the latter. This completes the discussion for all sub-moves of the algorithm in the extended configuration space.

Crossing vertex

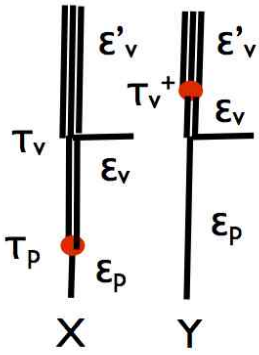

For the above extended configurations, the relevant weights are

$$Z(X) = e^{-\epsilon_p \tau_p} \langle i_v | \hat{b}^\dagger | i_p \rangle e^{\epsilon_v \tau_p} \times e^{-\epsilon_v \tau_v} \langle i'_v | \hat{b}^\dagger | i_v \rangle e^{\epsilon'_v \tau_v}$$

$$Z(Y) = e^{-\epsilon_p \tau_v} \langle i_v | \hat{b}^\dagger | i_p \rangle e^{\epsilon_v \tau_v} \times e^{-\epsilon_v \tau_v^+} \langle i'_v | \hat{b}^\dagger | i_v \rangle e^{\epsilon'_v \tau_v^+}$$

or

$$\frac{Z(Y)}{Z(X)} = \frac{e^{-\epsilon_p \tau_{vp}}}{e^{-\epsilon_v \tau_{vp}}}$$

Balancing with $Z(X)P(X \to Y) = Z(Y)P(Y \to X)$, the algorithm sets

$$P(X \to Y) = e^{-\epsilon_p \tau_{vp}}$$

$$P(Y \to X) = e^{-\epsilon_v \tau_{vp}}$$

The above transition probability suggests that whenever the wormhead collides with a vertex of the same type at time τ_v, it first halts at time τ_v^- and then crosses the vertex with probability 1 to a new time τ_v^+. This global move is balanced.

Summary of moves in extended configuration space

The following is the flow which summarises all balanced moves in the extended configuration space. Without loss of generality, suppose that the wormhead is $\hat{b}^\dagger$ and moves forward at time τ_p.

1. Propose a new time $\tau_{p'}$ for the wormhead according to equation 2.22.
2. If the wormhead is not halted by any upcoming vertex during the move, then
   (a) either the wormhead jumps to a neighbouring site at time τ_v^+ (moving in the same direction) and creates a vertex along the way,
   (b) or the wormhead turns around in direction (i.e.. bounces).
3. If the wormhead is halted by an upcoming vertex at time τ_v during the move, then it is halted just before the vertex at time τ_v^-. Either one of the following will occur.
   (a) If the upcoming vertex is the wormtail, the wormpair (both the wormhead and wormtail) will be removed. (See next section.)
   (b) If the upcoming vertex is of the same type ($\hat{b}^\dagger$), the wormhead crosses over the vertex to a new time τ_v^+ with probability 1.
   (c) If the upcoming vertex is of conjugate type ($\hat{b}$), the wormhead
      i. either the wormhead jumps to the neighbouring site at time τ_v^+ (moving in the same direction), and deletes the vertex along the way,
      ii. or the wormhead jumps to the neighbouring site of its neighbouring site at time τ_v^- (moving in opposite direction), and relinks the vertex along the way,
      iii. or the wormhead turns around in direction (i.e. bounces).
4. If the wormpair still exists, repeat step 1. Note that if the wormhead now moves backward in time, then the time signs all change in the above.

Rescaling the diagonal energy

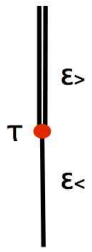

For the algorithm to be more efficient, the diagonal energy should be rescaled. A smart choice is

$$\epsilon_< \leftarrow \epsilon_< - \min\{\epsilon_<, \epsilon_>\} + \epsilon_{\text{offset}} \tag{2.28}$$
$$\epsilon_> \leftarrow \epsilon_> - \min\{\epsilon_<, \epsilon_>\} + \epsilon_{\text{offset}} \tag{2.29}$$

where the offset energy ϵ_{offset} can be any choice of positive number, i.e. $\epsilon_{\text{offset}} > 0$. Advanced users tune ϵ_{offset} for better algorithmic efficiency. This choice ensures that $\epsilon_<, \epsilon_> > 0$.

Updating density matrix

Whenever the wormhead touches the imaginary plane crossing the time of the wormtail, the worms are at equal time. When this happens, the corresponding density matrix element is updated.

2.3.4 Updates in configuration space

The objective of the directed worm algorithm is to generate new configurations via the extended configuration space stochastically. A configuration becomes an extended configuration upon the creation of a wormpair, and the vice versa upon its annihilation.

Wormpair creation/ annihilation

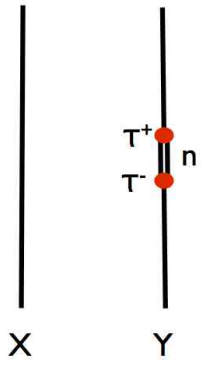

To insert randomly a wormpair, at any time $\tau \in [0, \beta)$, and at any of the L sites, there are $4\beta L$ ways of doing so to any existing configuration, say X. The factor 4 comes from the fact that, first, either a $\hat{b} - \hat{b}^\dagger$ or $\hat{b}^\dagger - \hat{b}$ wormpair is created, and second, either the $\hat{b}$ or $\hat{b}^\dagger$ worm is the wormhead, thus the other the wormtail.

Therefore, any configuration must be $4\beta L$-degenerate in the extended configuration space, and the relevant weights become

$$Z(X) = 4\beta L \tag{2.30}$$
$$Z(Y) = n \tag{2.31}$$

where n is the number of particles enclosed within the wormpair. Since $Z(X)P(X \to Y) = Z(Y)P(Y \to X)$, the algorithm defines the transition probabilities as

$$P(X \to Y) = \frac{1}{4\beta L} \tag{2.32}$$
$$P(Y \to X) = \frac{1}{n}\ . \tag{2.33}$$

1. In the wormpair-creation process, the probability of locating a random time and a random site is $\frac{1}{4\beta L}$. Therefore, the wormpair is always created with probability 1.
2. In the wormpair-annihilation process, the probability of choosing any 1 of the n particles to be annihilated is $\frac{1}{n}$. Therefore, the wormpair is always removed with probability 1.

Summary of moves in configuration space

1. Starting from any configuration, randomly pick a time and a site.
2. At that location, either insert a $\hat{b} - \hat{b}^\dagger$ or a $\hat{b}^\dagger - \hat{b}$ wormpair with 50-50 chance. The following exceptions may arise.
   (a) If there is no particle at that location, then insert a $\hat{b}^\dagger - \hat{b}$ wormpair with 50% chance. The other 50% chance goes to not inserting any wormpair.
   (b) If the number of particles at that location has reached a maximum, then insert a $\hat{b} - \hat{b}^\dagger$ wormpair with 50% chance. The other 50% chance goes to not inserting any wormpair.
3. Pick with 50-50 chance either $\hat{b}$ or $\hat{b}^\dagger$ as the wormhead, and thus the other being the wormtail.
4. The wormhead random-walks in the extended configuration space, until the wormhead collides into the wormtail.
5. Remove the wormpair.
6. Repeat step 1.

Updating density matrix

1. Just before the annihilation of the wormpair, the diagonal density matrix element is updated.

2. Should any insertion of wormpair fail, the diagonal density matrix element is updated.

Chapter 3

Thermometry

This chapter discusses the theoretical thermometry schemes regarding optical lattices. Throughout, I restrict the discussion to bosons. The chapter is based on one of my publications [47].

3.1 Introduction

3.1.1 Temperature determination

Temperature is one of the important physical quantity that determines the phase of any particular system. In the classical world, for instance, water exists as either solid ice, liquid water or gaseous steam at different temperature and pressure. In this example, the temperature can be indicated by a mercury-in-glass thermometer, only because its temperature dependence of the volume property has been previously known and calibrated. In general, a thermometer measures a temperature-dependent property of a subsystem in thermal equilibrium with the rest of the system. Here, the disturbance to the subsystem is assumed to be negligible in the measurement process, such that it gets quickly relaxed back to equilibrium by the bulk.

In the quantum limit towards atomic scale, temperature determination poses tough challenges to experimentalists [48]. To be specific, validity and accuracy are the two concerns. First, quantum measurements can cause a non-negligible disturbance to the subsystem, because in the atomic limit, the latter is not small after all with respect to the bulk. We say such measurements to be *destructive*, i.e. destroying the quantum state of the system, thus questioning fundamentally on the validity of such temperature determination. Second, the accuracy of quantum measurements is largely challenged by the Heisenberg uncertainty principle in the

atomic limit. No longer could a single measurement be sufficient to determine the temperature accurately. To enhance on its accuracy, either more information regarding the system must be made available, or more repetitive measurements have to be performed. The latter, unfortunately, makes temperature determination of quantum systems very *expensive*.

In particular, this chapter is only devoted to the subject matter of accurate temperature determination for bosons parabolically-trapped in quantum optical lattices.

3.1.2 Physical system

In the tight-binding limit, parabolically-trapped bosons in a 3D optical lattice can be accurately modelled by the single-band boson Hubbard Hamiltonian [38]

$$\hat{H} - \mu N = -t \sum_{\langle i,j \rangle} \hat{b}_i^\dagger \hat{b}_j + \frac{U}{2} \sum_i n_i(n_i - 1) - \sum_i (\mu - V_T r_i^2) n_i \tag{1.15}$$

where $\hat{H}$, in this chapter, specifically refers to the canonical Hamiltonian, and a total number of N bosons exists in the optical lattice with chemical potential μ and external harmonic trapping V_T. The nearest-neighbour hopping t, and the onsite repulsion strength U are derived from the lattice laser potential V_0 through band-structure calculations. In the Fock representation $\{|n_i\rangle\}$, n_i represents the number of bosons at site i, and $\hat{b}_i$ ($\hat{b}_j^\dagger$) is the annihilation (creation) operator at site i (j). In the last term, $\mathbf{r}_i$ denotes the displacement vector of site i from the centre of the parabolic trap.

The thermodynamical properties of the system are theoretically summarised in the partition function $Z = \mathrm{Tr} \exp[-\beta(\hat{H} - \mu N)]$ with inverse temperature $\beta = 1/k_B T$ [10]. The physics of trapped bosons in an optical lattice (equation 1.15) is summarized in the phase diagram illustrated in figure 1.4, where its phase is also determined by the local density

$$\langle n(\mathbf{r}) \rangle = \frac{1}{Z} \mathrm{Tr}\, n(\mathbf{r}) \exp[-\beta(\hat{H} - \mu N)] \ . \tag{3.1}$$

In the limit towards lower densities, the system becomes a normal fluid. In the presence of a confining harmonic trap, the densities become inhomogeneous. In particular, the densities become sparse in the wings due to huge potential energy barrier. Therefore, the wings of the bosonic trapped system exhibit always the normal-fluid phase.

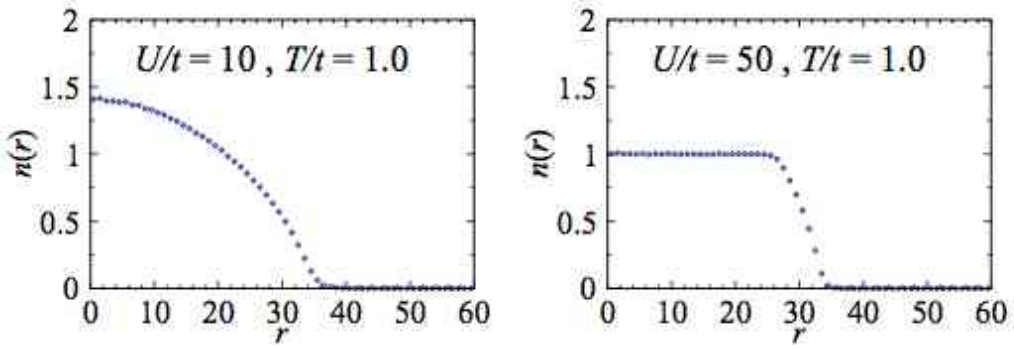

Figure 3.1: Cross sectional density $n(r)$ of a 3D bosonic ^{87}Rb optical lattice system with $N = 125000$, averaged over 1000 independent measurements obtained from a QMC simulation. Here, the parameters are $U/t = 10$ (left), 50 (right), $T/t = 1$, and $V_T/t = 0.0277$.

Recently, direct comparisons over time-of-flight images [32], and radial density profiles [37], of bosonic optical lattices between theory and experiment have been studied. Excellent quantitative agreements have been observed, and this builds the confidence over the use of ab-initio Quantum Monte Carlo (QMC) (see chapter 2) simulations of the single-band boson Hubbard Hamiltonian as a mimic of the bosonic optical lattice experiments. In this chapter, independent experimental measurements are mimicked by uncorrelated QMC measurements, where the autocorrelation time of $\tau < 0.2$ has been strictly imposed for the uncorrelation criterion. Figure 3.1 is an example.

3.1.3 Single site addressability

Recent progress over the use of florescence techniques in bosonic optical lattice experiments has enabled single-site resolution/addressability of in-situ density images [36]. Figure 3.2 illustrates a single measurement of atom distribution for a 2D bosonic optical lattice at different interaction strengths U/t [36]. The single-site resolution gives the possibility to extract more information from the system. Having more inputs such as density-density correlations and incompressibility enhance the accuracy of temperature determination.

For 3D optical lattices, only the integrated densities

$$\langle n(\rho) \rangle = \int \langle n(\mathbf{r}) \rangle \, dz \tag{3.2}$$

along the line-of-sight, i.e. z-direction, can be captured by density imaging.

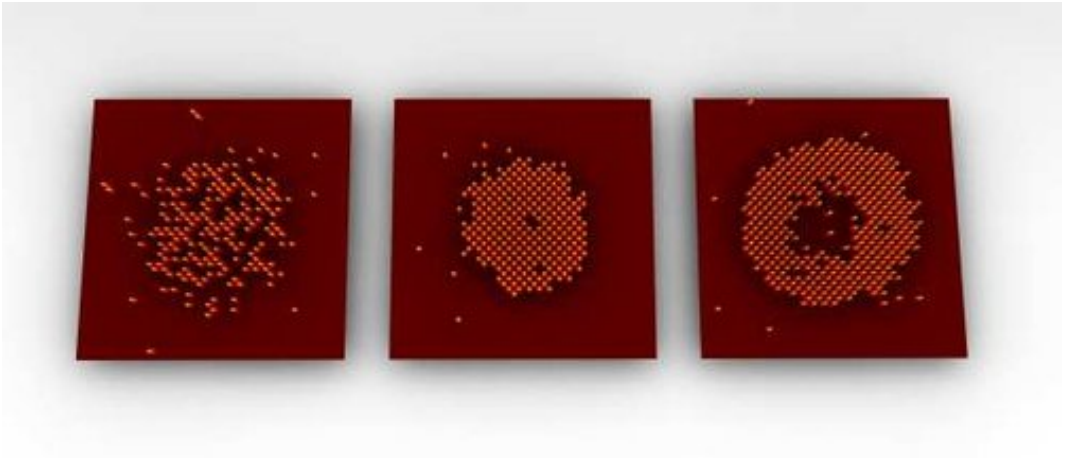

Figure 3.2: A single measurement of atom distribution for an ultracold quantum gas held in a two-dimensional optical lattice. The bosons, indicated by bright spots, are confined towards the parabolic trap centre. The interaction strength U/t increases from left to right, and thus transiting the system from being a superfluid into being a Mott insulator. Recent experimental advancement enables good visualisation of the Mott plateau (middle) around the trap centre up to single-site resolution. At extremely large interaction strength U/t, there exists a high probability to locate 2 bosons per site in the vicinity around the trap centre. However, current fluorescence experiments could not distinguish a doublon from a hole, therefore indicating dark spots around the centre (right). *This figure is replicated from Nature 467, 68 (2010).* [36]

3.2 Fluctuation-dissipation thermometry

3.2.1 Theory

The theory behind fluctuation-dissipation thermometry starts with the differentiation of $\langle n(\rho)\rangle$ w.r.t. μ, i.e.

$$\begin{aligned}
\frac{\partial\langle n(\boldsymbol{\rho})\rangle}{\partial\mu} &= \frac{\partial}{\partial\mu}\int dz\,\frac{1}{Z}\mathrm{Tr}\,n(\mathbf{r})\exp[-\beta(\hat{H}-\mu N)] \\
&= \int dz\,\frac{1}{Z}\mathrm{Tr}\,\beta N\,n(\mathbf{r})\exp[-\beta(\hat{H}-\mu N)] \\
&\quad -\int dz\,\frac{1}{Z^2}\Big(\mathrm{Tr}\,\beta N\exp[-\beta(\hat{H}-\mu N)]\Big)\Big(\mathrm{Tr}\,n(\mathbf{r})\exp[-\beta(\hat{H}-\mu N)]\Big) \\
&= \beta\left(\langle n(\boldsymbol{\rho})N\rangle - \langle n(\boldsymbol{\rho})\rangle\langle N\rangle\right) \qquad (3.3)
\end{aligned}$$

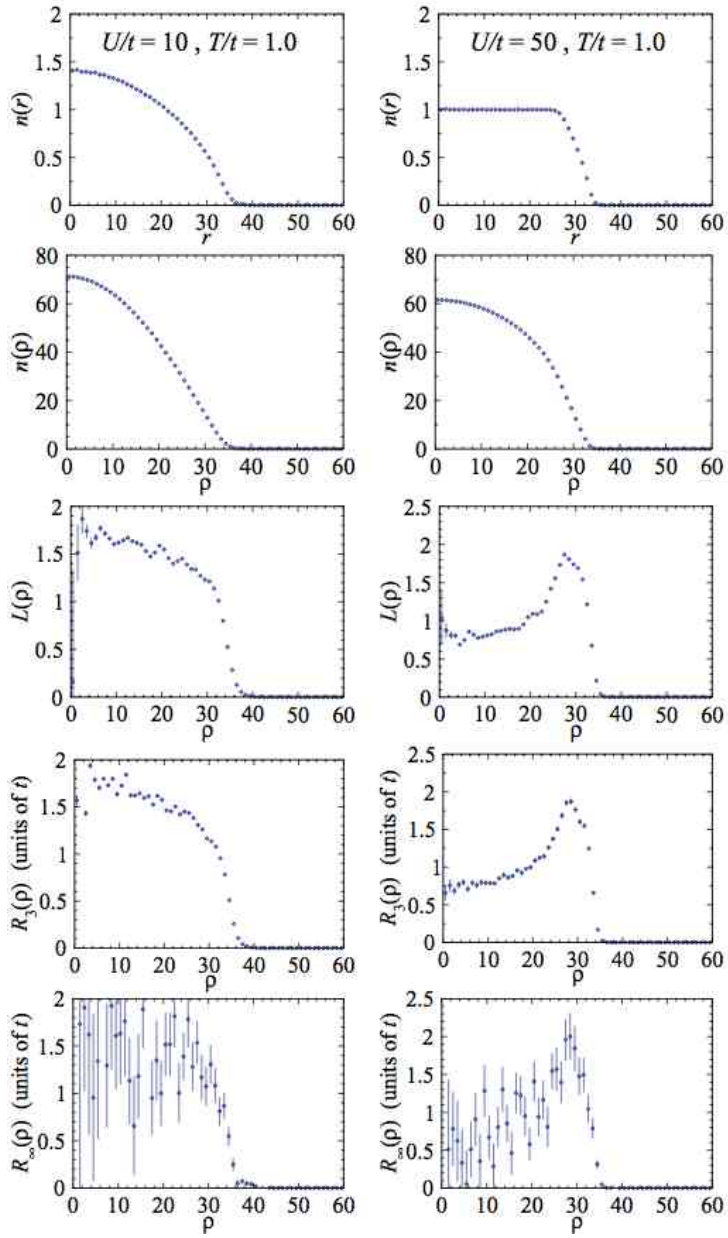

Figure 3.3: Illustration of the quantities entering the FD thermometry formula. Shown from top to bottom are: (1) cross-sectional density $n(r)$, (2) column-integrated density $n(\rho)$, (3) dissipation term $L(\rho)$, (4) fluctuation term ($\xi = 3$) $R_3(\rho)$, and (5) fluctuation term ($\xi = \infty$) $R_\infty(\rho)$. We take a 3D bosonic ^{87}Rb optical lattice system with $N = 125000$, and we average over 1000 independent measurements obtained from a QMC simulation. The parameters in the left column are $U/t = 10$, $T/t = 1$, and the parameters in the right column are $U/t = 50$, $T/t = 1$. The trapping frequency is $V_T/t = 0.0091$ (left), 0.0277 (right).

or

$$k_B T \frac{\partial \langle n(\boldsymbol{\rho}) \rangle}{\partial \mu} = \langle n(\boldsymbol{\rho}) N \rangle - \langle n(\boldsymbol{\rho}) \rangle \langle N \rangle \ . \tag{3.4}$$

In the validity of the local density approximation (LDA), the column-integrated density becomes

$$\langle n(\boldsymbol{\rho}) \rangle \overset{\text{LDA}}{=} \langle n(\mu; \boldsymbol{\rho}) \rangle \tag{3.5}$$

where μ here refers to the local chemical potential in equation 3.5. The dissipation term is therefore

$$L(\boldsymbol{\rho}) = \frac{\partial \langle n(\boldsymbol{\rho}) \rangle}{\partial \mu} \overset{\text{LDA}}{=} -\frac{1}{2V_T} \frac{1}{\rho} \frac{\partial \langle n(\boldsymbol{\rho}) \rangle}{\partial \rho} \ . \tag{3.6}$$

Defining the fluctuation term as

$$R(\boldsymbol{\rho}) = \langle n(\boldsymbol{\rho}) N \rangle - \langle n(\boldsymbol{\rho}) \rangle \langle N \rangle \ , \tag{3.7}$$

the temperature T can be derived from the slope of the linear equation

$$k_B T L(\boldsymbol{\rho}) = R(\boldsymbol{\rho}) \ . \tag{3.8}$$

This is the proposal by Jason and Ho [49].

For some reasons, we have to generalize their proposal. Interested only in fluctuations

$$R_\xi(\boldsymbol{\rho}) = \int d\boldsymbol{\rho}' \left\{ \langle n(\boldsymbol{\rho}) n(\boldsymbol{\rho}') \rangle - \langle n(\boldsymbol{\rho}) \rangle \langle n(\boldsymbol{\rho}') \rangle \right\} \theta(\xi - |\boldsymbol{\rho} - \boldsymbol{\rho}'|) \tag{3.9}$$

within a window size ξ, the linear equation

$$k_B T L(\boldsymbol{\rho}) = R_\xi(\boldsymbol{\rho}) \ . \tag{3.10}$$

remains still valid only if the value of ξ exceeds the density-density correlation length of the system. Here, $\theta(\cdot)$ is the Heaviside step function. For radial symmetric lattices, both the dissipation and fluctuation terms could be averaged over the angular variable ϕ, i.e.

$$L(\rho) = \frac{1}{2\pi} \int L(\boldsymbol{\rho}) \, d\phi \tag{3.11}$$

$$R(\rho) = \frac{1}{2\pi} \int R(\boldsymbol{\rho}) \, d\phi \tag{3.12}$$

where $\boldsymbol{\rho} = \boldsymbol{\rho}(\rho, \phi)$. Figure 3.3 illustrates the scheme, and highlights the importance of noise control with correct window sizing. In the limit of infinite window size, i.e. $\xi \to \infty$, the noise in $R_\xi(\rho)$ grows beyond control which makes the FD

thermometry scheme infeasible for accurate temperature determination.

Finally, the temperature T can be estimated from a least-squares fit taking the measurement errors into account, i.e.

$$\left(\sum_i \frac{R_i^2}{\Delta_{Li}^2}\right) - \left(\sum_i \frac{L_i R_i}{\Delta_{Li}^2}\right)\hat{T} = -\left(\sum_i \frac{L_i R_i}{\Delta_{Ri}^2}\right)\hat{T}^3 + \left(\sum_i \frac{L_i^2}{\Delta_{Ri}^2}\right)\hat{T}^4 \ . \quad (3.13)$$

Note that the FD thermometry scheme reduces to the proposal by Jason and Ho in the limit of infinite window sizing, i.e. $\xi \to \infty$.

3.2.2 Window sizing

Accurate determination of temperature relies heavily on the noise control of $R_\xi(\rho)$ with a correct window size of ξ. Due to a lack of knowledge of the density-density correlation length, the optimal choice for ξ is unknown at first which is to be determined through a systematic approach as illustrated in figure 3.4. In this approach, ξ is gradually increased from 0 until it exceeds the density-density correlation length, indicated by the linearity of the $L(\rho)$-$R(\rho)$ plot. Increasing ξ further will smear out the linearity due to increasing statistical noise in $R(\rho)$. This approach illustrates how the density-density correlation length could be found in an experimental system. In this example, with a temperature of $T/t = 1$, the optimal window size of $\xi = 3$ is sufficient to capture (almost) all the correlations. Using $\xi = 3$ as the standard for $T/t = 1$ and higher temperatures, we show the

System	nr of shots	
	ξ=3	ξ=∞
$U/t = 10$, $T/t = 1$	20	$\mathcal{O}(10^4)$
$U/t = 10$, $T/t = 3$	14	$\mathcal{O}(10^4)$
$U/t = 50$, $T/t = 1$	21	$\mathcal{O}(10^4)$
$U/t = 50$, $T/t = 3$	12	$\mathcal{O}(10^4)$

Table 3.1: Number of uncorrelated measurements needed to determine the temperature accurately within 5% error for 3D ^{87}Rb optical lattice experiments trapping 125,000 bosons. The variance reduction through window-sizing leads to orders of magnitudes improvement, and thus making FD thermometry scheme as a feasible tool for accurate temperature determination. The parameters are the same as in figure 3.3.

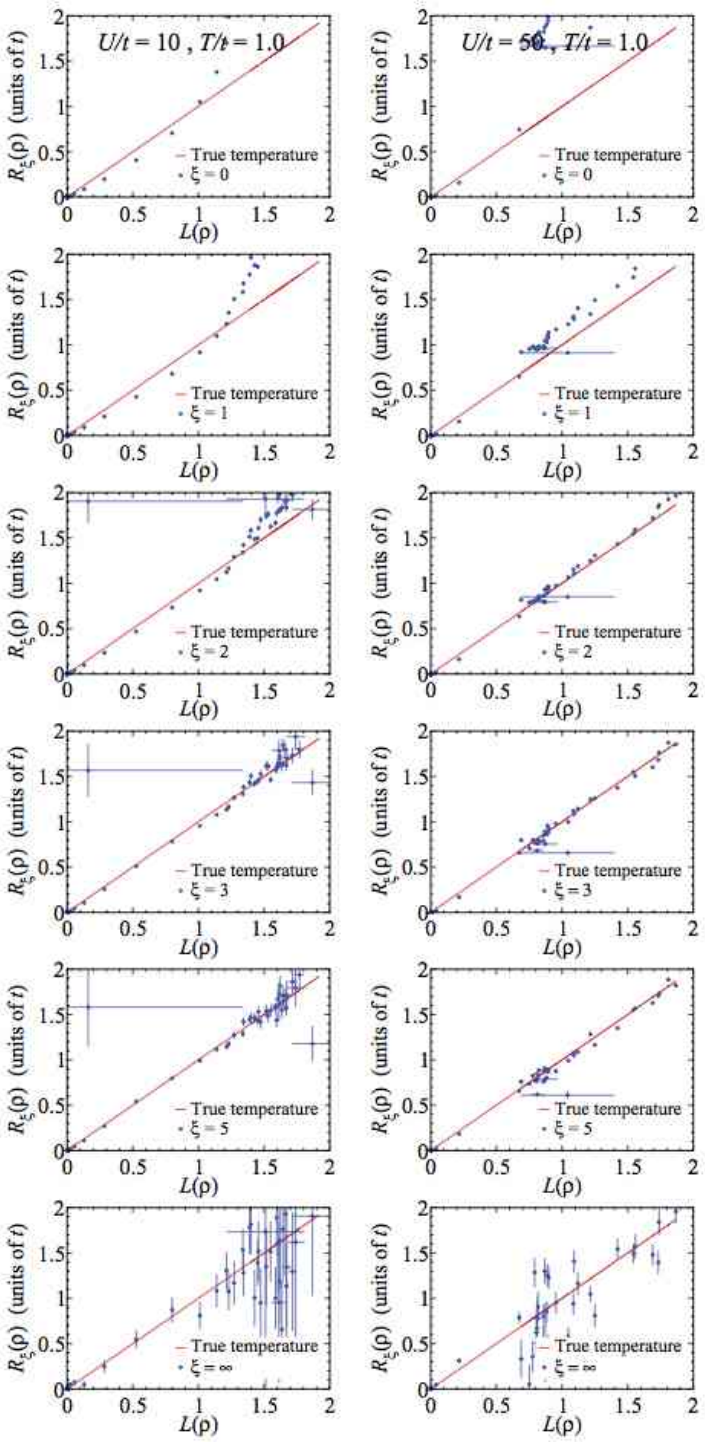

Figure 3.4: Illustration of the FD thermometry scheme by showing different $L(\rho) - R_\xi(\rho)$ plots at various window sizes $\xi = 0, 1, 2, 3, 5, \infty$. This approach illustrates how the density-density correlation length can be found in an experimental system. When the window size is smaller than density-density correlation length, systematic errors set in, and this results in nonlinear $L(\rho) - R(\rho)$ behaviour, while for ξ larger than the denisty-density correlation length, the behaviour of $L(\rho) - R(\rho)$ is linear. However, statistical noise also increases with increasing window size. The parameters are the same as in figure 3.3.

number of independent measurements needed to estimate the temperature within 5% error in Table 3.1. The enormous variance reduction through window sizing turns the FD thermometry scheme into a feasible tool for ultracold bosonic optical lattice experiments.

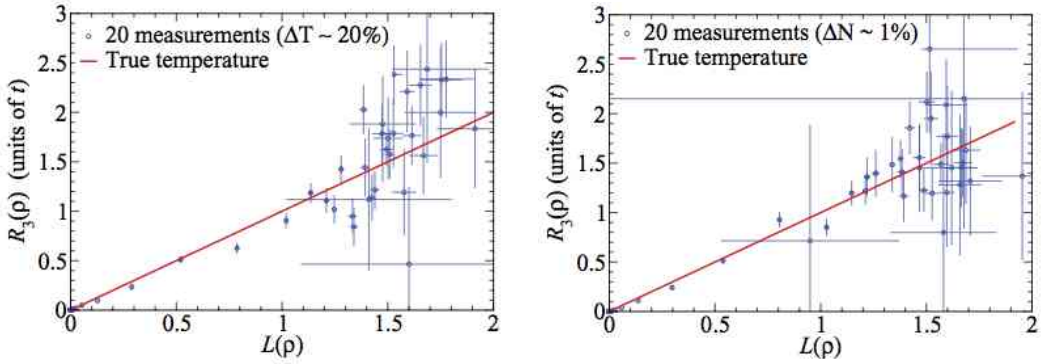

Figure 3.5: The FD thermometry scheme remains valid over 20% spread in temperature T (left), and 1% spread in the particle number N (right). The parameters for the 3D bosonic ^{87}Rb system are $N = 125000$, $U/t = 10$, $T/t = 1$, $V_T/t = 0.0091$. Here, the optimal window size is $\xi = 3$, and 20 independent measurements are obtained from a QMC simulation for accurate temperature determination within 5% error.

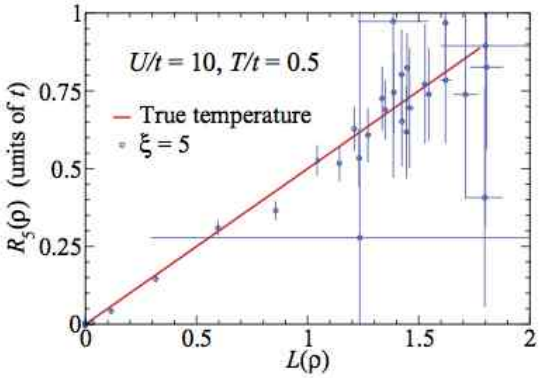

Figure 3.6: FD thermometry scheme at slightly lower temperature, for a 3D bosonic ^{87}-Rb optical lattice with parameters $N = 125000$, $U/t = 10$, $T/t = 0.5$, $V_T/t = 0.0091$. Here, the optimal window size is $\xi = 5$, and the data is obtained by averaging over 100 independent measurements from a QMC simulation.

With 20 independent measurements uniformly distributed over 20% spread in T

and 1% spread in N, the FD thermometry scheme remains applicable. See figure 3.5. At lower temperature, the scheme remains valid, although a larger ξ is needed, and the statistical noise will inevitably grow. See figure 3.6. In this example, with a temperature of $T/t = 0.5$, the optimal window size is $\xi = 5$, and 100 independent measurements are required to attain an accurate temperature estimate within 5% error.

3.2.3 Experimental imperfections

Density imaging with few-sites resolution

Although we aim at single-site resolution detection tools in the analysis of the FD thermometry scheme in this chapter, the scheme remains applicable when the resolution is just a few sites, therefore giving some room for possible experimental imperfections. See figure 3.7. Here, we simulate such experiments with different resolutions up to 5 sites, by varying the bin. The FD thermometry scheme suffers from increasing systematic errors in the dissipation term $L(\rho)$ both for $U/t = 10$ and for $U/t = 50$ at $T/t = 1$. Yet, a relatively linear $L(\rho)$-$R(\rho)$ relationship could still be observed on average. For these cases alone, the estimated temperatures do not deviate more than 10% as shown in Table 3.2 . However, when the resolution is worse than 5 sites, uncontrolled systematic errors dominate, and the scheme fails.

n-site resolution (binwidth)	estimated temperature (units of t)	
	(U/t=10 , T/t=1):	(U/t=50 , T/t=1):
1	0.977 ± 0.007	0.994 ± 0.008
2	0.990 ± 0.006	1.014 ± 0.007
3	0.997 ± 0.006	1.032 ± 0.007
4	1.016 ± 0.007	1.045 ± 0.008
5	1.048 ± 0.007	1.094 ± 0.008

Table 3.2: Estimated temperatures.

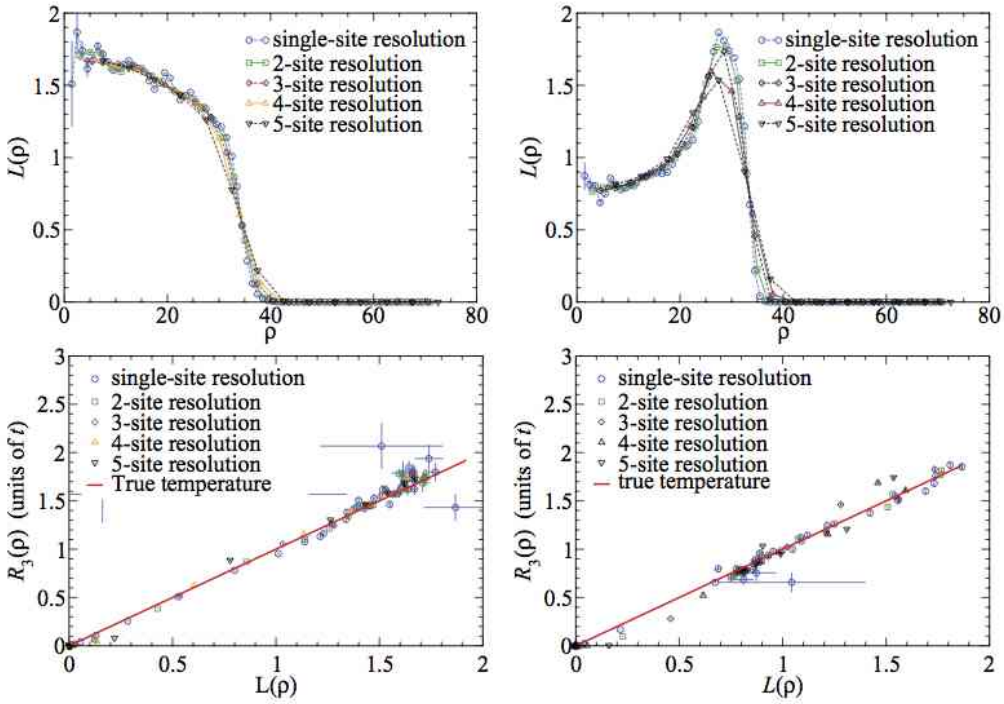

Figure 3.7: The FD thermometry scheme remains applicable to in-situ density experiments, which have a resolution of a few sites. The system consists of a 3D optical lattice with $N = 125000$ bosonic ^{87}Rb atoms. Increasing the bin width increases the systematic error in the dissipation term $L(\rho)$, but the temperature estimate remains reliable. The parameters are the same as in figure 3.3. Here, the optimal window size is $\xi = 3$, and 1000 independent measurements are averaged out from a QMC simulation.

Density imaging with doublon-hole indistinguishability

Current single-site addressability experiments using fluorescence techniques can only measure the parity (even-odd) of the occupation number per site [36]. This experimental imperfection affects the FD thermometry scheme. Figure 3.8 illustrates the effect of double-hole indistinguishability.

An inspection of the $L(\rho)$-$R_\xi(\rho)$ plot shows a group of data points that fall on the linear slope. These points correspond to the bosons at the edges. Deep in the edges, the number of doublons is very low compared to the number of holes due to the low overall density and the high potential-energy cost of creating a doublon. By selecting those points in the $L(\rho)$-$R_\xi(\rho)$ plot that are on the linear slope, we

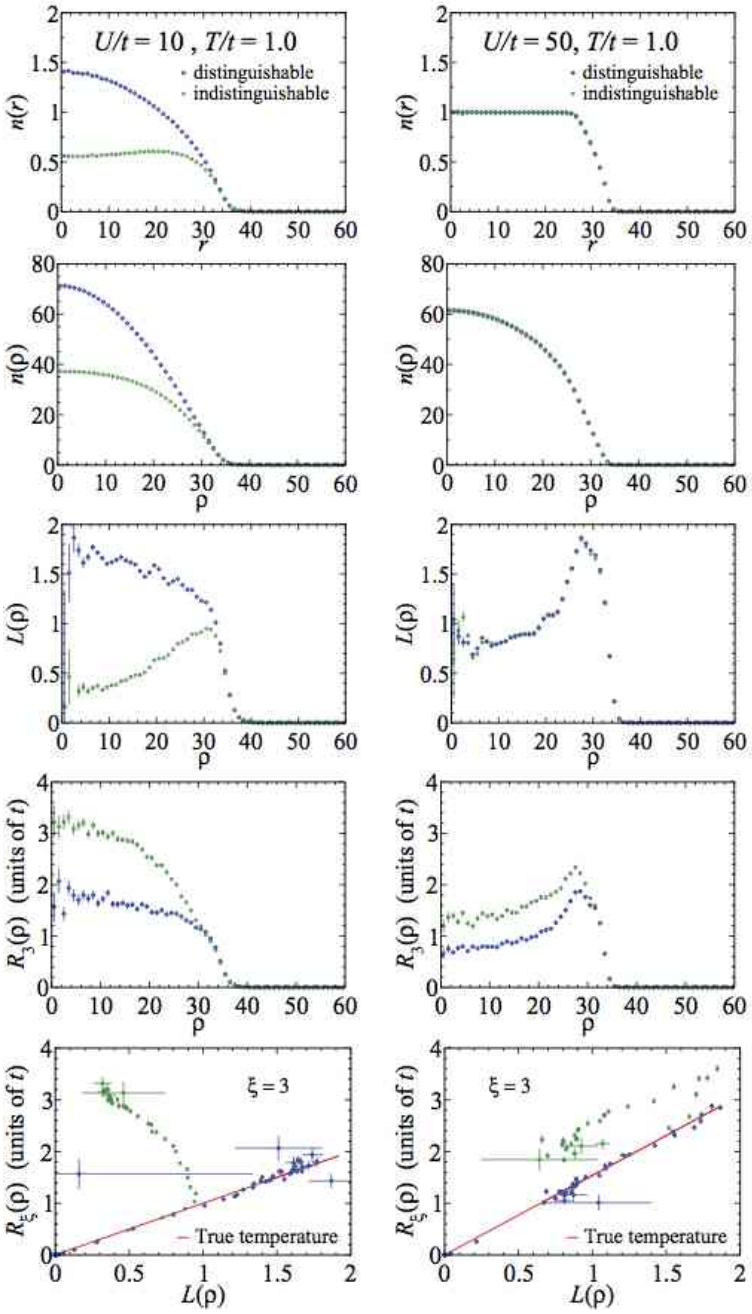

Figure 3.8: FD thermometry scheme in the presence of double-hole indistinguishability. The parameters are the same as in figure 3.3. Blue circles (green squares) show the curve where doublons can (cannot) be distinguished from holes.

could still obtain an acceptable estimate of the temperature.

The estimated temperatures for this example are tabulated as follows.

System	estimated temperature (units of t)
$U/t = 10$, $T/t = 1$	0.985 ± 0.008
$U/t = 50$, $T/t = 1$	1.003 ± 0.012

3.3 Wing thermometry

3.3.1 Theory

Deep in the edges, or *wings*, there will always be a normal region for any temperature T/t and interaction strength U/t where the system is well described by the second-order high temperature expansion (HTE2).

In this section, we shall formulate the theory. Note that a slightly different notation from the paper will be used in this section for the sake of convenience.

The partition function of the system is

$$Z = \mathrm{Tr}\, e^{-\beta(\hat{H}-\mu N)} = \mathrm{Tr}\, e^{-\beta(D+\hat{V})} \tag{3.14}$$

where the diagonal/offdiagonal part reads

$$D = \frac{U}{2}\sum_i n_i(n_i-1) - \sum_i \mu_i n_i \tag{3.15}$$

$$\hat{V} = -t\sum_{\langle i,j\rangle} \hat{b}_i^\dagger \hat{b}_j \ . \tag{3.16}$$

Since

$$\begin{aligned}\left[\sum_k \mu_k n_k\,,\,\sum_{\langle i,j\rangle}\hat{b}_i^\dagger\hat{b}_j\right] &= \sum_k\sum_{\langle i,j\rangle}\mu_k\left[\hat{b}_k^\dagger\hat{b}_k\,,\,\hat{b}_i^\dagger\hat{b}_j\right]\\ &= \sum_k\sum_{\langle i,j\rangle}\mu_k\left\{\hat{b}_i^\dagger\left[\hat{b}_k^\dagger\hat{b}_k\,,\,\hat{b}_j\right]+\left[\hat{b}_k^\dagger\hat{b}_k\,,\,\hat{b}_i^\dagger\right]\hat{b}_j\right\}\\ &= \sum_k\sum_{\langle i,j\rangle}\mu_k\left\{-\hat{b}_i^\dagger\hat{b}_k\delta_{kj}+\hat{b}_k^\dagger\hat{b}_j\delta_{ki}\right\}\\ &= \sum_{\langle i,j\rangle}(\mu_i-\mu_j)\,\hat{b}_i^\dagger\hat{b}_j \end{aligned} \tag{3.17}$$

$$\begin{aligned}\left[\sum_k n_k^2\,,\,\sum_{\langle i,j\rangle}\hat{b}_i^\dagger\hat{b}_j\right] &= \sum_k\sum_{\langle i,j\rangle}\left\{n_k\left[\hat{b}_k^\dagger\hat{b}_k\,,\,\hat{b}_i^\dagger\hat{b}_j\right]+\left[\hat{b}_k^\dagger\hat{b}_k\,,\,\hat{b}_i^\dagger\hat{b}_j\right]n_k\right\}\\ &= \sum_{\langle i,j\rangle}\left\{(n_i-n_j)\hat{b}_i^\dagger\hat{b}_j+\hat{b}_i^\dagger\hat{b}_j(n_i-n_j)\right\}\\ &= \sum_{\langle i,j\rangle}\hat{b}_i^\dagger\hat{b}_j(n_i-n_j+2)\;, \end{aligned} \tag{3.18}$$

we derive the following important commutator

$$\left[D\,,\hat{V}\right]=-t\sum_{\langle i,j\rangle}\hat{b}_i^\dagger\hat{b}_j\gamma_{ij} \tag{3.19}$$

where

$$\gamma_{ij}=U(n_i-n_j)+U-(\mu_i-\mu_j)\;. \tag{3.20}$$

The following are immediate consequences.

$$\left[D\,,\,\left[D\,,\hat{V}\right]\right] = -t\sum_{\langle i,j\rangle}\hat{b}_i^\dagger\hat{b}_j\gamma_{ij}^2 \tag{3.21}$$

$$\left[D\,\left[D\,,\,\left[D\,,\hat{V}\right]\right]\right] = -t\sum_{\langle i,j\rangle}\hat{b}_i^\dagger\hat{b}_j\gamma_{ij}^3 \tag{3.22}$$

Using the relation

$$e^{\tau D}\,\hat{V}\,e^{-\tau D}=\hat{V}+\tau\left[D\,,\,\hat{V}\right]+\frac{\tau^2}{2!}\left[D\,,\,\left[D\,,\hat{V}\right]\right]+\cdots \tag{3.23}$$

we arrive at

$$e^{\tau D}\,\hat{V}\,e^{-\tau D} = -t\sum_{\langle i,j\rangle}\hat{b}_i^\dagger\hat{b}_j e^{\tau\gamma_{ij}}\ . \tag{3.24}$$

Next, we expand the partition function up to second order in $\hat{V}$, i.e.

$$Z = \mathrm{Tr}\,e^{-\beta D} + \int_0^\beta d\tau_1\int_0^{\tau_1} d\tau_2\,\mathrm{Tr}\,e^{-\beta D}\,e^{\tau_1 D}\,\hat{V}\,e^{-\tau_1 D}\,e^{\tau_2 D}\,\hat{V}\,e^{-\tau_2 D}\ . \tag{3.25}$$

Zeroth order

Defining

$$Z^{(0)} = \mathrm{Tr}\,e^{-\beta D}\ , \tag{3.26}$$

we have

$$Z^{(0)} = \sum_{\{n_i\}}\prod_i e^{-\beta D_i} = \prod_i\sum_{n_i} e^{-\beta D_i} = \prod_i Z_i^{(0)} \tag{3.27}$$

where

$$Z_i^{(0)} = \sum_{n_i=0}^{\infty} e^{-\beta D_i} \tag{3.28}$$

$$D_i = \frac{U}{2}n_i(n_i-1) - \mu_i n_i \tag{3.29}$$

The zeroth-order density is therefore

$$\langle n_i^{(0)}\rangle = \frac{1}{Z^{(0)}}\mathrm{Tr}\,n_i\,e^{-\beta D} = \frac{1}{Z_i^{(0)}}\sum_{n_i=0}^{\infty} n_i\,e^{-\beta D_i}\ . \tag{3.30}$$

Second order

Expressing

$$Z \approx Z^{(0)}(1+Z^{(2)}) \tag{3.31}$$

such that

$$Z^{(2)} = \frac{1}{Z^{(0)}}\left(\int_0^\beta d\tau_1\int_0^{\tau_1} d\tau_2\,\mathrm{Tr}\,e^{-\beta D}\,e^{\tau_1 D}\,\hat{V}\,e^{-\tau_1 D}\,e^{\tau_2 D}\,\hat{V}\,e^{-\tau_2 D}\right)\ , \tag{3.32}$$

we arrive at

$$\begin{aligned} Z^{(2)} &= (-t)^2\sum_{\langle i,j\rangle}\frac{1}{Z_i^{(0)}}\frac{1}{Z_j^{(0)}}\int_0^\beta d\tau_1\int_0^{\tau_1} d\tau_2\left[\sum_{n_i^\delta=n_i-1}\sum_{n_j^\delta=n_j+1} n_i n_j^\delta e^{-\beta D_i}e^{-\beta D_j}e^{\tau_1\gamma_{ij}^\delta}e^{\tau_2\gamma_{ji}}\right. \\ &\quad\left. + \sum_{n_j^\delta=n_j-1}\sum_{n_i^\delta=n_i+1} n_j n_i^\delta e^{-\beta D_i}e^{-\beta D_j}e^{\tau_1\gamma_{ji}^\delta}e^{\tau_2\gamma_{ij}}\right]\ . \end{aligned} \tag{3.33}$$

Next, we perform the integrals. If $\gamma_{ij}^{\delta} = \gamma_{ji} = 0$,

$$\int_0^{\beta} d\tau_1 \int_0^{\tau_1} d\tau_2 \, e^{\tau_1 \gamma_{ij}^{\delta}} e^{\tau_2 \gamma_{ji}} = \frac{\beta^2}{2} \ , \tag{3.34}$$

otherwise,

$$\int_0^{\beta} d\tau_1 \int_0^{\tau_1} d\tau_2 \, e^{\tau_1 \gamma_{ij}^{\delta}} e^{\tau_2 \gamma_{ji}} = \beta^2 \left[\frac{1 - e^{\beta\gamma_{ij}^{\delta}}}{(\beta\gamma_{ij}^{\delta})(\beta\gamma_{ji})} - \frac{1 - e^{\beta\gamma_{ij}^{\delta} + \beta\gamma_{ji}}}{(\beta\gamma_{ij}^{\delta} + \beta\gamma_{ji})(\beta\gamma_{ji})} \right] \tag{3.35}$$

Defining

$$\Gamma_{ij}^{\delta} = \frac{1 - e^{\beta\gamma_{ij}^{\delta}}}{(\beta\gamma_{ij}^{\delta})(\beta\gamma_{ji})} - \frac{1 - e^{\beta\gamma_{ij}^{\delta} + \beta\gamma_{ji}}}{(\beta\gamma_{ij}^{\delta} + \beta\gamma_{ji})(\beta\gamma_{ji})} \ , \tag{3.36}$$

we have

$$Z^{(2)} = \sum_{\langle i,j \rangle} \frac{(-\beta t)^2}{Z_i^{(0)} Z_j^{(0)}} \left[\sum_{n_i n_j}^{(-,+)} n_i n_j^{\delta} e^{-\beta(D_i + D_j)} \Gamma_{ij}^{\delta} \ + \ \sum_{n_i n_j}^{(+,-)} n_i^{\delta} n_j e^{-\beta(D_i + D_j)} \Gamma_{ji}^{\delta} \right] \tag{3.37}$$

where $(-,+)$ stands for $(n_i^{\delta} = n_i - 1,\, n_j^{\delta} = n_j + 1)$, and vice-versa for $(+,-)$.

Since

$$\langle n_i \rangle = -\frac{1}{\beta} \frac{\partial}{\partial \mu_i} \log Z \ , \tag{3.38}$$

we have

$$\langle n_i \rangle \approx -\frac{1}{\beta} \frac{\partial}{\partial \mu_i} \left[\log Z^{(0)} + \log(1 + Z^{(2)}) \right] \approx \langle n_i^{(0)} \rangle - \frac{1}{\beta} \frac{\partial Z^{(2)}}{\partial \mu_i} \ . \tag{3.39}$$

After differentiation, the density, up to the second order, is

$$\begin{aligned} \langle n_i \rangle \ &= \ \langle n_i^{(0)} \rangle + \sum_{\langle i,j \rangle} \frac{(-\beta t)^2}{Z_i^{(0)} Z_j^{(0)}} \\ &\quad \times \left[\sum_{n_i n_j}^{(-,+)} \left(n_i - \langle n_i^{(0)} \rangle + \frac{\chi_{ij}^{\delta}}{\Gamma_{ij}^{\delta}} \right) n_i n_j^{\delta} e^{-\beta(D_i + D_j)} \Gamma_{ij}^{\delta} \right. \\ &\quad \left. + \sum_{n_i n_j}^{(+,-)} \left(n_i - \langle n_i^{(0)} \rangle + \frac{\chi_{ji}^{\delta}}{\Gamma_{ji}^{\delta}} \right) n_i^{\delta} n_j e^{-\beta(D_i + D_j)} \Gamma_{ji}^{\delta} \right] \end{aligned} \tag{3.40}$$

where

$$\chi_{ij}^{\delta} = \frac{e^{\beta\gamma_{ij}^{\delta}}}{(\beta\gamma_{ij}^{\delta})(\beta\gamma_{ji})} + \frac{1 - e^{\beta\gamma_{ij}^{\delta} + \beta\gamma_{ji}}}{(\beta\gamma_{ij}^{\delta} + \beta\gamma_{ji})(\beta\gamma_{ji})^2} - \frac{(1 - e^{\beta\gamma_{ij}^{\delta}})(\beta\gamma_{ij}^{\delta} - \beta\gamma_{ji})}{(\beta\gamma_{ij}^{\delta})^2 (\beta\gamma_{ji})^2} \ . \tag{3.41}$$

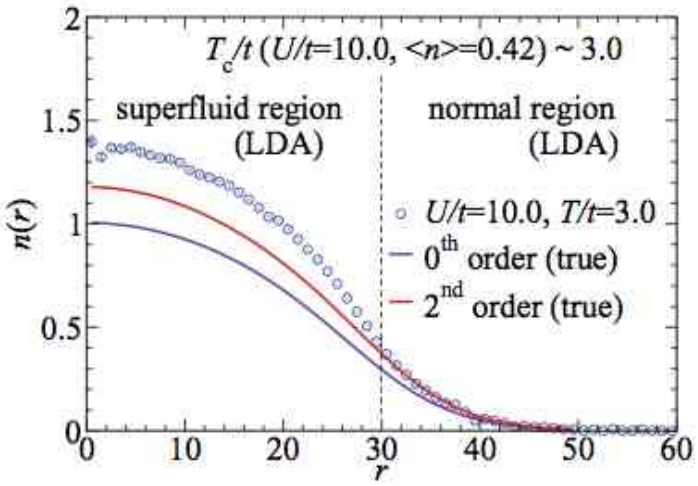

Figure 3.9: Illustrating the concept of wing thermometry for a 3D bosonic ^{87}Rb optical lattice system, *ie.,* describing the normal state by high temperature series expansions. Blue circles: In-situ density profile obtained from 100 uncorrelated measurements obtained by a QMC simulation with parameters $U/t = 10$, $T/t = 3$, $N = 125,000$. The superfluid-normal phase boundary occurs at the density $\langle n \rangle = 0.42$ or chemical potential $\mu/t = -2.75$. The second order series captures all the physics in the normal regime, whereas the zeroth order has a very small validity range.

3.3.2 Advantages and limitations

Figure 3.9 illustrates the concept of wing thermometry.

1. The zeroth order expansion does a poor job in describing the densities at the edges of the system, as also indicated in reference [50].
2. The second order expansion gives a fairly accurate description of the densities over the edges if they exhibit normal behaviour. The second order expansion captures the entire physics in the normal regime.

As illustrated in the example, the second order densities match almost exactly with the in-situ density profile, obtained from 100 independent measurements of a QMC simulation, over the entire normal region. Here, the superfluid-normal phase boundary is determined from LDA calculations.

In the extreme case where the entire region is normal, the HTE2 thermometry scheme becomes an extremely powerful thermometer. See figure 3.10. In fact, only a single measurement is sufficient to accurately estimate both the temperature

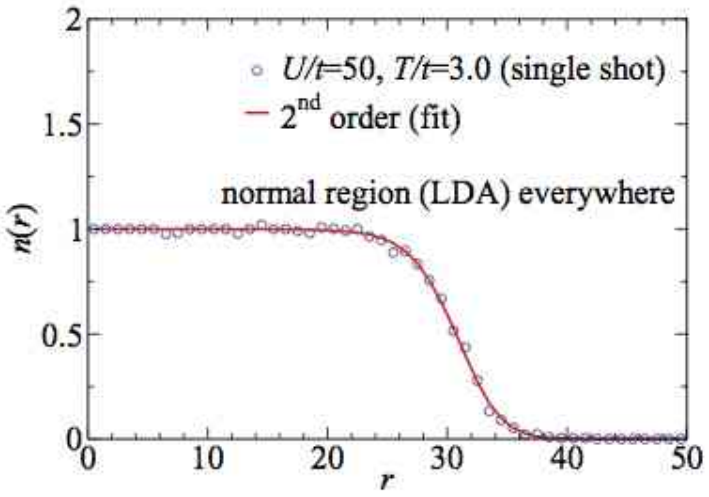

Figure 3.10: Second order high temperature series expansion thermometry scheme for a bosonic system that is entirely in the normal phase. No more than a single shot of cross-sectional density is needed to estimate the temperature and chemical potential within 10% accuracy. We take a 3D optical lattice system with bosonic ^{87}Rb atoms and parameters $N = 125,000$, $\mu/t = 25.97$, $U/t = 50$, $T/t = 3$. The blue circles are obtained from a single measurement in a QMC simulation; and the red line is a least-square fit over the entire normal region where $\mu_{\text{fit}}/t = 25.92$ and $T_{\text{fit}}/t = 2.824$ nK.

T and chemical potential μ up to 10% error within the HTE2 thermometry scheme.

In the limit of very low temperatures where the normal wings become too narrow, it may be that the density in the edges is so low that it cannot be measured due to low signal-to-noise ratio. When this happens, HTE2 thermometry scheme becomes infeasible. It is possible to use higher-order thermometry schemes, but the gain is minimal compared to the additional effort.

Chapter 4

Quantitative simulations

This chapter is devoted to quantitative simulations of bosons trapped in an actual-size 3D optical lattice with simulation parameters mimicked as realistically to the experiments as possible, which are quantitatively modelled by the boson Hubbard model [34], i.e.

$$\hat{H} - \mu N = -\sum_{\langle i,j \rangle} t_{ij}\, \hat{b}_i^\dagger \hat{b}_j + \sum_i \frac{U_i}{2} n_i(n_i - 1) - \sum_i \mu_i n_i \ , \tag{4.1}$$

and efficiently solved by the Quantum Monte Carlo (directed) worm algorithm [41] ([42]). The spirit behind this algorithm has been discussed in detail previously in Chapter 2, and its implementation fully outlined in Appendix A.

This chapter is based on one of my publications [51], which highlights this state-of-art algorithmic implementation to be one of the fastest, if not the fastest, in the world till date. In particular, current simulations are ultra robust, which are capable of handling up to 10 million lattice sites. Of which, some manage to converge results in no longer than a couple of hours.

4.1 Mimicking the experiments

Mimicking the experiments by Bloch [32], the optical lattice anisotropy gives rise to direction-dependent band structure parameters (refer to appendix A.1), i.e.

$$\begin{aligned} t_{ij} &= t_x \ , \ t_y \ , \text{or } t_z \\ U_i &= U \\ \mu_i &= \mu - (V_{Tx} x_i^2 + V_{Ty} y_i^2 + V_{Tz} z_i^2) \end{aligned}$$

which become increasingly valid in the close vicinity towards the centre of the optical lattice trap.

4.1.1 Momentum distribution and time-of-flight image

The momentum distribution of bosons in an optical lattice at equilibrium is

$$\begin{aligned} \langle n(\vec{k})\rangle &= \langle \hat{\psi}^\dagger(\vec{k})\hat{\psi}(\vec{k})\rangle \\ &= \frac{1}{L^3}\int d\vec{r}\, d\vec{r}'\, \langle \hat{\psi}^\dagger(\vec{r})\hat{\psi}(\vec{r}')\rangle\, e^{i\vec{k}\cdot(\vec{r}-\vec{r}')} \\ &= \frac{1}{L^3}\sum_{i,j}\int d\vec{r}\, d\vec{r}'\, w(\vec{r}-\vec{r}_i)\, e^{i\vec{k}\cdot(\vec{r}-\vec{r}_i)}\, w(\vec{r}'-\vec{r}_j)\, e^{i\vec{k}\cdot(\vec{r}'-\vec{r}_j)}\, \langle \hat{b}_i^\dagger \hat{b}_j\rangle\, e^{i\vec{k}\cdot(\vec{r}_i-\vec{r}_j)} \ . \end{aligned} \tag{4.2}$$

Defining the Fourier transform of the wannier function $w(\vec{r})$ as

$$\tilde{w}(\vec{k}) = \frac{1}{\sqrt{L^3}}\int d\vec{r}\, w(\vec{r})\, e^{-i\vec{k}\cdot\vec{r}} \ , \tag{4.3}$$

and the interference term

$$S(\vec{k}) = \sum_{i,j}\langle \hat{b}_i^\dagger \hat{b}_j\rangle\, e^{i\vec{k}\cdot(\vec{r}_i-\vec{r}_j)} \tag{4.4}$$

the momentum distribution becomes

$$\langle n(\vec{k})\rangle = |\tilde{w}(\vec{k})|^2 S(\vec{k}) \ . \tag{4.5}$$

which is indirectly probed in experiements by a time-of-flight image [32], i.e.

$$\langle n_f(\vec{k})\rangle \approx |\tilde{w}(\vec{k})|^2 \sum_{i,j}\langle \hat{b}_i^\dagger \hat{b}_j\rangle\, e^{i\vec{k}\cdot(\vec{r}_i-\vec{r}_j)-i\gamma_f(r_i^2-r_j^2)} \ , \tag{4.6}$$

having time-of-flight phase $\gamma_f = \frac{m}{2\hbar t_f}$ with t_f being the actual time of flight. (See Appendix A.2 for its derivation.)

Exploiting the symmetries

$$\langle n_f(\vec{k})\rangle = \langle n_f(-\vec{k})\rangle \tag{4.7}$$

$$\langle \hat{b}_i^\dagger \hat{b}_j\rangle = \langle \hat{b}_j^\dagger \hat{b}_i\rangle \tag{4.8}$$

equation 4.6 reduces to

$$\langle n_f(\vec{k})\rangle \approx |\tilde{w}(\vec{k})|^2 \sum_{|r_\alpha|\geq 0} g_f(\vec{r}_\alpha)\cos(\vec{k}\cdot\vec{r}_\alpha) \ , \tag{4.9}$$

with time-of-flight Green function defined as

$$g_f(\vec{r}_\alpha) = \sum_{i,j\,:\,\vec{r}_i-\vec{r}_j=\pm\vec{r}_\alpha} \langle \hat{b}_i^\dagger \hat{b}_j\rangle \cos(\gamma_f(r_i^2-r_j^2)) \ . \tag{4.10}$$

Last but not least, the time-of-flight image observed in experiments are column-integrated along the line-of-sight, say the z-direction:

$$\langle n_f(k_x, k_y)\rangle = \int dk_z \langle n_f(\vec{k})\rangle \ , \tag{4.11}$$

as illustrated in figure 4.1.

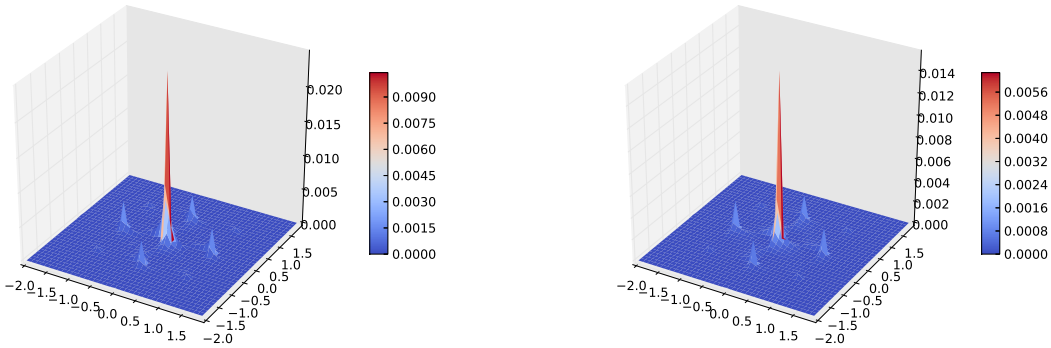

Figure 4.1: Time of flight images (equation 4.11) obtained from QMC-DWA simulations mimicking optical lattice experiments as realistically as possible, with interaction strength $U/t = 8.11$ (left) , 27.5 (right) at temperature $T/t = 1$. The anisotropic optical lattice, with lattice strength $\vec{V}_0 = (8.8E_{rx}, 8E_{ry}, 8E_{rz})$ (left), $(12.64E_{rx}, 11.75E_{ry}, 11.75E_{rz})$ (right), and laser wavelength $\vec{\lambda} = (765, 843, 843)$nm, confines 2.8×10^5 (left), 9.4×10^4 (right) bosons in a parabolic trap $\vec{V}_T = (17.1, 10.9, 11.3)$Hz (left), $(19.9, 13.0, 13.4)$Hz (right). The horizontal axes are k_x and k_y in units of 2π, and the vertical axis is the time-of-flight distribution $\langle n_f(k_x, k_y)\rangle$ in unit of inverse momentum area resolution $(\Delta k_x \Delta k_y)^{-1}$, taking experimental value $(\Delta k_x \Delta k_y) \approx 0.1^2$ in units of $(2\pi)^2$. See appendix A.3 for further details.

Important quantities that derive from the time-of-flight distribution include the condensate fraction

$$f_c = \langle n_f(0,0)\rangle \ , \tag{4.12}$$

and the visibility

$$\mathcal{V} = \frac{\langle n_f(0,0)\rangle - \langle n_f(\pi,\pi)\rangle}{\langle n_f(0,0)\rangle + \langle n_f(\pi,\pi)\rangle} \ . \tag{4.13}$$

4.1.2 Density profile

The density profile of bosons in an optical lattice at equilibrium

$$\langle n(\mathbf{r})\rangle = \frac{1}{Z}\,\mathrm{Tr}\, n(\mathbf{r})\exp[-\beta(\hat{H}-\mu N)] \tag{3.1}$$

is usually measured cross-sectional $\langle n(x,y,z=0)\rangle$, or column-integrated

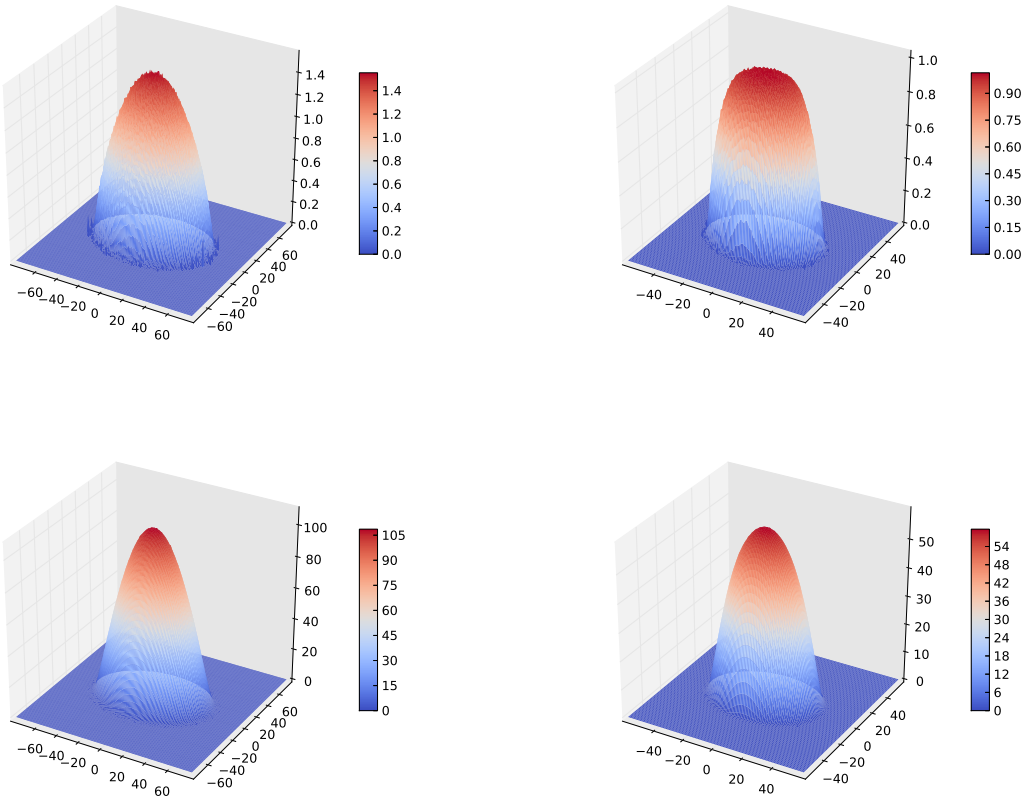

Figure 4.2: Cross-sectional (top) and column-integrated (bottom) density profiles obtained from QMC-DWA simulations mimicking optical lattice experiments as realistically as possible, with interaction strength $U/t = 8.11$ (left) , 27.5 (right) at temperature $T/t = 1$. The anisotropic optical lattice experiments take the same setup parameters as in figure 4.1. See appendix A.4 for further details.

$$\langle n(x,y)\rangle = \int \langle n(\vec{r})\rangle\, dz \tag{4.14}$$

in experiments, as illustrated in figure 4.2.

4.2 Beyond parabolic trapping

In this section, we attempt to quantify the non-parabolic effect of gaussian traps due to the $1/e^2$-waist.

4.2.1 Quantifying error budgets

The first step is to quantify the error budgets for a certain 3D optical lattice experiemnt due to the various imperfections, as illustrated in table 4.1.

$\pm 5\%$ fluctuations in	estimated fluctuation in				
	$\langle E \rangle$	$\langle n(0,0,0) \rangle$	$\langle n(0,0) \rangle$	f_c	$\mathcal{V}$
$\langle N \rangle$	$< 6\%$	$< 3\%$	$< 3\%$	$< 4\%$	$< 1\%$
$^*a$	$< 2\%$	$< 5\%$	$< 2\%$	$< 5\%$	$< 1\%$
$^*V_{0x}$	$< 1\%$	$< 3\%$	$< 1\%$	$< 4\%$	$< 1\%$
$^*\lambda_x$	$< 1\%$	$< 2\%$	$< 1\%$	$< 6\%$	$< 1\%$

Table 4.1: Quantifying error budgets in energy $\langle E \rangle$, density at trap centre $\langle n(0,0,0) \rangle$, column-integrated density at trap centre $\langle n(0,0) \rangle$, condensate fraction f_c, and visibility $\mathcal{V}$, for a $\pm 5\%$ fluctuation in total particle number $\langle N \rangle$, s-wave scattering length a, lattice strength V_{0x}, and laser wavelength λ_x. The anisotropic optical lattice experiments take the same setup parameters as in figure 4.1. The estimated fluctuation is computed via QMC-DWA simulations, where the simulations indicated by (*) are performed such that the total particle number is fixed at $\langle N \rangle = 2.8 \times 10^5$. See appendix A.5 for further details.

4.2.2 A first remark of waist correction

The three-dimensional optical lattice is radially confined by the trapping envelope

$$V_0 \exp\left(-\frac{2r^2}{w_0^2}\right) \tag{1.4}$$

of waist (or $1/e^2$-radius) w_0 [28]. Consider the same experiment as figure 4.1, where a bosonic cloud spans over a radius $L \sim 50$ in an optical lattice with spacing $d \sim 400$nm. A Gaussian trap with a typical waist of $w_0 \sim 150\mu$m will induce an approximate 4.5% change over the lattice strength V_0 from the trap centre. Table 4.1 gives us a first idea of the most extreme variations over the physical observables we may measure in the experiments. Special attention should be paid to the spatial dependence of the lattice strength V_0, and thus also the interaction

strength U/t, in particularly to the next generation of experiments which involve a bigger bosonic cloud size whereby the spatial dependence cannot be neglected anymore.

In this chapter, however, we confine ourselves in the regime of current experiments, where we neglect the spatial dependence of V_0 due to Gaussian beam waist.

4.2.3 Corrections to parabolic trapping

For isotropic optical lattices, the correction to the trapping potential due to waist effects is

$$\Delta V_T(\vec{r}) = V_0 - \frac{2V_0}{w_0^2} r^2 - V_0 e^{-\frac{2r^2}{w_0^2}} \ , \tag{4.15}$$

which has minimal effect on the measurements for current experiments, as illustrated in figure 4.3 for instance. However, the waist effects will become more prominent in future experiments that involve bigger bosonic clouds.

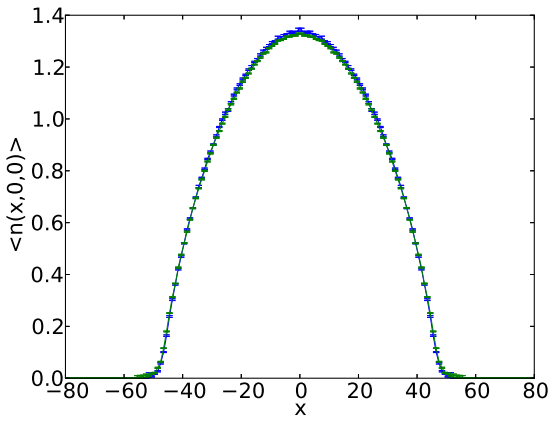

Figure 4.3: Cross-sectional density profiles obtained from QMC-DWA simulations for 2.8×10^5 bosons trapped in an isotropic optical lattice with interaction strength $U/t = 8.1$ at temperature $T/t = 1$. The lattice strength is taken to be 8.35 E_r, the laser wavelength 843 nm, and the s-wave scattering length 101 a_B. Blue: The trapping potential is assumed to be parabolic, with trapping frequency 10.5 Hz. Red: The trapping potential is corrected according to equation 4.15 with $w_0 = 150\mu m$. Waist correction reduces the density at the trap center $\langle n(0,0,0)\rangle$ by approximately 1%, therefore only spreading out slightly in the wings of the bosonic cloud which is however statistically irrelevant.

Chapter 5

Density functional theory

5.1 General formalism

5.1.1 Hohenberg-Kohn theorems

The foundation of density function theory is given by the following two Hohenberg-Kohn theorems [53].

Theorem I:
The non-degenerate ground state density $\rho(\mathbf{r})$ of interacting particles is uniquely determined by the external potential $V(\mathbf{r})$.[1]

Corollary I:
The non-degenerate ground state density $\rho(\mathbf{r})$ is mapped one-to-one to the many-particle wavefunction $\Psi(\mathbf{r})$ of the interacting system.

Theorem II:
There exists a functional $E[\rho]$ that depends only on the density $\rho(\mathbf{r})$, such that the minimum $E[\rho_0]$ is exactly the ground state energy.

1

Proof. Suppose there exists another external potential $V'(\mathbf{r})$ that gives $\rho(\mathbf{r})$. Denoting the hamiltonians $\hat{H}$ and $\hat{H}'$ repectively such that $\hat{H}|\Psi\rangle = E|\Psi\rangle$ and $\hat{H}'|\Psi'\rangle = E'|\Psi'\rangle$, the density can now be written as $\rho(\mathbf{r}) = |\Psi(\mathbf{r})|^2 = |\Psi'(\mathbf{r})|^2$ by assumption. Now,

$$\begin{aligned} \langle\Psi'|\hat{H}|\Psi'\rangle - \langle\Psi'|\hat{H}'|\Psi'\rangle &= \int d\mathbf{r}\,(V(\mathbf{r}) - V'(\mathbf{r}))\,\rho(\mathbf{r}) \\ \langle\Psi|\hat{H}'|\Psi\rangle - \langle\Psi|\hat{H}|\Psi\rangle &= \int d\mathbf{r}\,(V'(\mathbf{r}) - V(\mathbf{r}))\,\rho(\mathbf{r}) \end{aligned}$$

therefore $E+E' = \langle\Psi'|\hat{H}|\Psi'\rangle + \langle\Psi|\hat{H}'|\Psi\rangle > \langle\Psi|\hat{H}|\Psi\rangle + \langle\Psi'|\hat{H}'|\Psi'\rangle = E+E'$ due to the variational principle, resulting in a contradiction! □

Instead of solving the Schrödinger equation for N interacting particles, the ground state density and energy can be obtained exactly from a 3-dimensional minimization of the corresponding functional $E[\rho]$ if the latter is known. In practice, one has to resort to reasonable approximation schemes for $E[\rho]$. This drastic reduction in computational costs without much penalty to the accuracy is the main reason why density functional theory is used as a workhorse in the field of conventional material science today

5.1.2 Hohenberg-Kohn formalism

Following Hohenberg and Kohn (HK) [53], the exact ground state energy E and ground state density $\rho(\mathbf{r})$ can be determined by minimizing an energy functional of the density:

$$E\left[\rho\right] = \int d\mathbf{r}\, V(\mathbf{r})\rho(\mathbf{r}) + F[\rho]; \tag{5.1}$$

where the first term is the potential energy due to the external potential $V(\mathbf{r})$. The second term is an unknown but *universal* functional which includes the interaction and kinetic energies, but does not explicitly depend on $V(\mathbf{r})$. The generalization to potentially spin-polarized systems one introduces separate densities of the two spin components $\rho_\uparrow$ and $\rho_\downarrow$:

$$E\left[\rho_\uparrow, \rho_\downarrow\right] = \int d\mathbf{r}\, V(\mathbf{r})\left[\rho_\uparrow\left(\mathbf{r}\right) + \rho_\downarrow\left(\mathbf{r}\right)\right] + F\left[\rho_\uparrow, \rho_\downarrow\right], \tag{5.2}$$

An explicit (but rather inaccurate) expression for $F\left[\rho_\uparrow, \rho_\downarrow\right]$ is given by the Hohenberg-Kohn local spin density approximation (HK-LSDA)

$$F\left[\rho_\uparrow, \rho_\downarrow\right] = \int d\mathbf{r}\, \epsilon(\rho_\uparrow(\mathbf{r}), \rho_\downarrow(\mathbf{r})), \tag{5.3}$$

where $\epsilon\left(\rho_\uparrow, \rho_\downarrow\right)$ is the ground-state energy density of a homogeneous Fermi gas with the given spin densities[2]. In practice, $\epsilon\left(\rho_\uparrow, \rho_\downarrow\right)$ is obtained from accurate Quantum Monte Carlo calculations, and takes the form of equation B.5. (See appendix B.)

[2]The Thomas-Fermi (TF) approximation is recovered as a mean field approximation for $\epsilon\left(\rho_\uparrow, \rho_\downarrow\right)$. Here, the TF energy density is given by

$$\epsilon_{TF}(\rho_\uparrow, \rho_\downarrow) = \frac{3}{5}\rho_\uparrow E_{F\uparrow} + \frac{3}{5}\rho_\downarrow E_{F\downarrow}\ , \tag{5.4}$$

whereby only for the noninteracting case would the spin-up (down) Fermi energy be expressed as

$$E_{F\uparrow(\downarrow)} = \frac{\hbar^2 k_{F\uparrow(\downarrow)}^2}{2m} = \frac{\hbar^2}{2m}(6\pi^2\rho_{\uparrow(\downarrow)})^{2/3} \tag{5.5}$$

5.1.3 Kohn-Sham formalism

The kinetic part is usually highly non-local and cannot be treated well under the local approximation. Therefore, Kohn and Sham [54] proposed a more accurate functional by explicitly including the exact kinetic energy T_0 of non-interacting fermions. What is left is the interaction energy E_{HXC}, combining the usual Hartree (mean field term) E_H and the exchange-correlation correction E_{XC}:

$$F\left[\rho_{\uparrow},\rho_{\downarrow}\right]=T_0\left[\rho_{\uparrow},\rho_{\downarrow}\right]+E_{\mathrm{HXC}}\left[\rho_{\uparrow},\rho_{\downarrow}\right]. \tag{5.6}$$

A simple yet often reliable treatment of E_{HXC} is the *local spin-density approximation* (LSDA)

$$E_{\mathrm{HXC}}\left[\rho_{\uparrow},\rho_{\downarrow}\right]=\int d\mathbf{r}\,\epsilon_{\mathrm{HXC}}\left(\rho_{\uparrow}\left(\mathbf{r}\right),\rho_{\downarrow}\left(\mathbf{r}\right)\right), \tag{5.7}$$

where the functional is replaced by an integral over the interaction energy density[3] of a uniform system with the same local density. The objective is now to minimize the total energy

$$E=\int d\mathbf{r}\,\left(T_0\left[\rho_{\uparrow},\rho_{\downarrow};\mathbf{r}\right]+V(\mathbf{r})\big(\rho_{\uparrow}(\mathbf{r})+\rho_{\downarrow}(\mathbf{r})\big)+\epsilon_{\mathrm{HXC}}\left[\rho_{\uparrow},\rho_{\downarrow};\mathbf{r}\right]\right) \tag{5.9}$$

with respect to the spin densities ($\sigma=\uparrow,\downarrow$)

$$\rho_{\sigma}\left(\mathbf{r}\right)=\int\mathcal{D}\mathbf{r}_j\,\delta\left(\mathbf{r}-\mathbf{r}_1\right)\left|\prod_{\sigma'=\uparrow,\downarrow}det\left[\phi_n^{\sigma'}\left(\mathbf{r}_j\right)\right]\right|^2=\sum_{n\sigma}^{\mathrm{occ}}\left|\phi_n^{\sigma}\left(\mathbf{r}\right)\right|^2\ , \tag{5.10}$$

where $\phi_n^{\sigma}\left(\mathbf{r}\right)$ are normalized single-quasiparticle spin-orbitals filled to the Fermi level. Minimizing equation 5.9 with respect to the complex conjugate quasiparticle spin orbital $\phi_n^{\sigma *}\left(\mathbf{r}\right)$ subjected to the normalization constraint $\int d\mathbf{r}\left|\phi_n^{\sigma}\left(\mathbf{r}\right)\right|^2=1$, we arrive at the coupled Kohn-Sham (KS) eigenvalue equations [52]

$$\left(-\frac{\hbar^2}{2m}\nabla^2+V(\mathbf{r})+V_{\sigma}^{\mathrm{HXC}}\left(\rho_{\uparrow},\rho_{\downarrow};\mathbf{r}\right)\right)\phi_n^{\sigma}=\epsilon_n^{\sigma}\,\phi_n^{\sigma} \tag{5.11}$$

where the Langrange multiplier ϵ_n^{σ} is in fact the KS quasiparticle energy. Here, the hartree-exchange-correlation potential is

$$V_{\sigma}^{\mathrm{HXC}}\left(\rho_{\uparrow},\rho_{\downarrow};\mathbf{r}\right)=\frac{\delta}{\delta\rho_{\sigma}(\mathbf{r})}\left[\epsilon_{\mathrm{HXC}}(\rho_{\uparrow},\rho_{\downarrow};\mathbf{r})\right] \tag{5.12}$$

[3]

$$\epsilon_{\mathrm{HXC}}\left(\rho_{\uparrow},\rho_{\downarrow}\right)=\epsilon\left(\rho_{\uparrow},\rho_{\downarrow}\right)-\frac{3}{5}\rho_{\uparrow}\frac{\hbar^2}{2m}(6\pi^2\rho_{\uparrow})^{2/3}-\frac{3}{5}\rho_{\downarrow}\frac{\hbar^2}{2m}(6\pi^2\rho_{\downarrow})^{2/3} \tag{5.8}$$

It is convenient to define the KS single-quasiparticle hamiltonian

$$\hat{H}^{\sigma}_{\mathrm{KS}} = -\frac{\hbar^2}{2m}\nabla^2 + V^{\mathrm{eff}}_{\sigma}\left(\rho_{\uparrow}, \rho_{\downarrow}; \mathbf{r}\right) \tag{5.13}$$

where the effective potential is $V^{\mathrm{eff}}_{\sigma}(\rho_{\uparrow}, \rho_{\downarrow}; \mathbf{r}) = V(\mathbf{r}) + V^{\mathrm{HXC}}_{\sigma}(\rho_{\uparrow}, \rho_{\downarrow}; \mathbf{r})$.

5.2 KS-DFT for fermionic optical lattice

5.2.1 Lattice translational symmetry

In an optical lattice with periodicity $\mathbf{d}$, *i.e.* $V(\mathbf{r}+\mathbf{d}) = V(\mathbf{r})$, we shall make use of Bloch's theorem [29] to rewrite the KS quasiparticle orbitals as

$$\phi^{\sigma}_{n\mathbf{k}}\left(\mathbf{r}\right) = e^{2\pi i \mathbf{k}\cdot\mathbf{r}} u^{\sigma}_{n\mathbf{k}}\left(\mathbf{r}\right) \ , \tag{5.14}$$

with periodic Bloch orbitals $u^{\sigma}_{n\mathbf{k}}\left(\mathbf{r}\right)$. The wavevectors $\mathbf{k}$ run over the first Brillouin zone of the reciprocal lattice. Working in the units of lattice spacing $d = \frac{\lambda}{2}$ and recoil energy $E_R = \frac{\hbar^2}{2m}\left(\frac{2\pi}{\lambda}\right)^2$ ($\hbar$ is the reduced Planck constant and m the atomic mass), the coupled Kohn-Sham eigenvalue equations 5.11 become

$$\left[\frac{1}{\pi^2}\left(-i\nabla + 2\pi\mathbf{k}\right)^2 + V^{\mathrm{eff}}_{\sigma}\left(\rho_{\uparrow}, \rho_{\downarrow}; \mathbf{r}\right)\right] u^{\sigma}_{n\mathbf{k}}\left(\mathbf{r}\right) = \epsilon^{\sigma}_{n\mathbf{k}} u^{\sigma}_{n\mathbf{k}}\left(\mathbf{r}\right) \ . \tag{5.15}$$

They must be solved self-consistently with the ground state densities

$$\rho_{\sigma}\left(\mathbf{r}\right) = \sum_{n\mathbf{k}} \left|u^{\sigma}_{n\mathbf{k}}\left(\mathbf{r}\right)\right|^2 \Theta\left(\mu - \epsilon^{\sigma}_{n\mathbf{k}}\right) \tag{5.16}$$

where $\Theta(\cdots)$ is the Heaviside function. The total ground state energy is calculated from the set of all quasiparticle energies $\epsilon^{\sigma}_{n\mathbf{k}}$ as

$$E = \sum_{n\mathbf{k}\sigma} \epsilon^{\sigma}_{n\mathbf{k}} \Theta\left(\mu - \epsilon^{\sigma}_{n\mathbf{k}}\right) \tag{5.17}$$

up to the Fermi level. The Bloch orbitals are next expanded in the plane wave basis

$$u^{\sigma}_{n\mathbf{k}}\left(\mathbf{r}\right) = \sum_{\mathbf{G}} c^{\sigma}_{n\mathbf{k}}\left(\mathbf{G}\right) \exp\left(2\pi i \mathbf{G}\cdot\mathbf{r}\right) \ , \tag{5.18}$$

the KS equation (5.15) becomes a coupled set of matrix eigenvalue equations

$$4\left(\mathbf{G}+\mathbf{k}\right)^2 c^{\sigma}_{n\mathbf{k}}\left(\mathbf{G}\right) + \sum_{\mathbf{G}'} V^{\mathrm{eff}}_{\mathbf{G}-\mathbf{G}'} c^{\sigma}_{n\mathbf{k}}\left(\mathbf{G}'\right) = \epsilon^{\sigma}_{n\mathbf{k}} c^{\sigma}_{n\mathbf{k}}\left(\mathbf{G}\right) \tag{5.19}$$

for reciprocal vectors $\mathbf{G}$. As a remark, the effective potential possesses both translational and inversion symmetry, and therefore its Fourier components

$$V_{\mathbf{G}}^{\text{eff}} = \frac{1}{M^3} \int_{\text{unitcell}} V^{\text{eff}}(\mathbf{r}) \exp(-2\pi i \mathbf{G} \cdot \mathbf{r})\, d\mathbf{r} \tag{5.20}$$

must be real and related by $V_{\mathbf{G}}^{\text{eff}} = V_{-\mathbf{G}}^{\text{eff}}$.

5.2.2 Simple cubic lattice (O_h symmetry)

An isotropic three dimensional optical lattice with simple cubic (sc) geometry possesses O_h point group symmetry [55], therefore likewise for the corresponding reciprocal lattice and its band structure [29]. With M×M×M being the dimensions of the lattice, the reciprocal lattice basis vectors read

$$\mathbf{b}_1 = \hat{\mathbf{x}}\ ,\ \mathbf{b}_2 = \hat{\mathbf{y}}\ ,\ \mathbf{b}_3 = \hat{\mathbf{z}} \tag{5.21}$$

and the reciprocal lattice vectors are

$$\mathbf{G} = \frac{m_1}{M}\mathbf{b}_1 + \frac{m_2}{M}\mathbf{b}_2 + \frac{m_3}{M}\mathbf{b}_3 \tag{5.22}$$

where $m_1, m_2, m_3 = 0, \pm 1, \pm 2, \cdots$. Knowing the point group symmetry of the band structure reduces computational efforts greatly. The O_h point group possesses, for instance, inversion (J) and reflection (σ_h, σ_d) symmetries [55], thus giving rise to the following 48-fold degeneracy for the quasiparticle energies $\epsilon_{n\mathbf{k}}^{\sigma}$:

1. J-symmetry:

$$\epsilon_{n(k_x,k_y,k_z)}^{\sigma} = \epsilon_{n(-k_x,-k_y,-k_z)}^{\sigma} \tag{5.23}$$

2. σ_h-symmetry:

$$\epsilon_{n(k_x,k_y,k_z)}^{\sigma} = \epsilon_{n(\pm k_x,\pm k_y,\pm k_z)}^{\sigma} \tag{5.24}$$

3. σ_d-symmetry:

$$\epsilon_{n(k_x,k_y,k_z)}^{\sigma} = \epsilon_{n(k_y,k_x,k_z)}^{\sigma} \tag{5.25}$$
$$\epsilon_{n(k_x,k_y,k_z)}^{\sigma} = \epsilon_{n(k_x,k_z,k_y)}^{\sigma} \tag{5.26}$$
$$\epsilon_{n(k_x,k_y,k_z)}^{\sigma} = \epsilon_{n(k_z,k_y,k_x)}^{\sigma}\ . \tag{5.27}$$

Note that the same degeneracy exists likewise for the norm of quasiparticle orbitals $|\phi_n^{\sigma}(\mathbf{r})|^2$, therefore reducing computational efforts further.

The high-symmetry k-points in the band structure of the sc lattice are

Notation	**k**-point
Γ	(0, 0, 0)
X	(1/2, 0, 0)
M	(1/2, 1/2, 0)
R	(1/2, 1/2, 1/2)

In the event of anistropy along the z-direction, some of the degeneracies within the O_h point group are lifted, thus resulting in a D_{4h} point group. Its symmetry can be easily worked out from the respective character table [55].

5.2.3 Face centered cubic lattice

A primitive cell, consisting of two adjacent lattice sites within simple cubic (sc) geometry, translates to form a face centered cubic (fcc) lattice, therefore resulting in a body centered cubic (bcc) reciprocal lattice [29]. With $M \times M \times M$ being the dimensions of the **optical lattice**, the reciprocal lattice basis vectors read

$$\mathbf{b}_1 = \frac{1}{2}(\hat{\mathbf{x}} + \hat{\mathbf{y}} - \hat{\mathbf{z}}) \ , \ \mathbf{b}_2 = \frac{1}{2}(\hat{\mathbf{x}} - \hat{\mathbf{y}} + \hat{\mathbf{z}}) \ , \ \mathbf{b}_3 = \frac{1}{2}(-\hat{\mathbf{x}} + \hat{\mathbf{y}} + \hat{\mathbf{z}}) \tag{5.28}$$

and the reciprocal lattice vectors are

$$\mathbf{G} = \frac{m_1}{M}\mathbf{b}_1 + \frac{m_2}{M}\mathbf{b}_2 + \frac{m_3}{M}\mathbf{b}_3 \tag{5.29}$$

where $m_1, m_2, m_3 = 0, \pm 1, \pm 2, \cdots$. The band structure still possesses O_h point group symmetry which facilitates the reduction of computational efforts greatly. The high symmetry **k**-points in the band structure of the fcc lattice are

Notation	**k**-point
Γ	(0, 0, 0)
X	(1/2, 0, 0)
W	(1/4, 1/2, 0)
L	(1/4, 1/4, 1/4)

For two identical sites within the primitive cell of a fcc lattice, its band structure is in fact equivilant to the band structure of a sc lattice. More specifically in this scenario, each energy band of a sc lattice are folded into two bands of a fcc lattice about some highly symmetric **k**-planes.

5.3 Remarks

5.3.1 Validity of Kohn-Sham density functional theory

The validity of Kohn-Sham density functional theory (DFT) for fermionic optical lattices can be tested through quantitative comparisons with direct Quantum Monte Carlo (QMC) simulations[4]. The excellent agreement, as illustrated in figure 5.1, demonstrates that DFT calculations with an LSDA functional are extremely reliable in weak and moderate optical lattices, therefore justifying its validity.

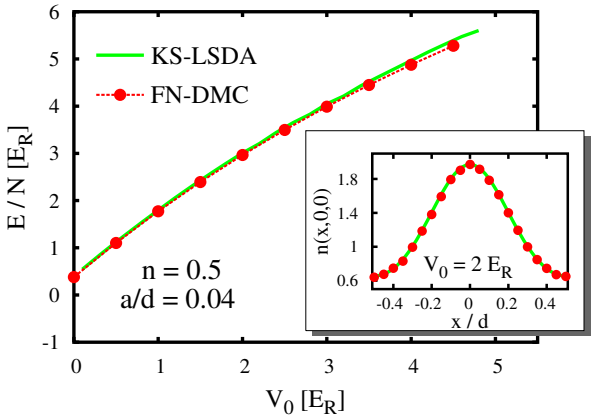

Figure 5.1: **Comparison of DFT results to QMC**. Main panel: energy per particle E/N vs. optical lattice intensity V_0, at quarter-filling $n = \rho d^3 = 0.5$ with scattering length $a = 0.04d$. The green curve is the results of Kohn-Sham DFT within the local spin-density approximation, the red points to Fixed-Node Diffusion Monte Carlo simulations. Inset: cross-sectional density profile on one lattice site, particularly at the lattice intensity of $V_0 = 2.0E_R$.

[4]We perform fixed-node diffusion Monte Carlo simulations for fermionic optical lattice, extended from the previous study of the homogeneous system [70]. To simulate Fermi gases in an optical lattice of sinple cubic geometry, we employ the trial wave function (B.1) using the Bloch states (5.14) (obtained by solving the equation (5.11) for different lattice depths $V(\mathbf{r})$ without scattering, i.e. $a = 0$) as single-particle orbitals. The Bloch states are expanded in a plane-wave basis, as in equation (5.18), using up to 13^3 states. Unlike other Monte Carlo techniques for the single-band Fermi-Hubbard model which are in principle reliable only for deep lattices, this current version of continuous-space fixed-node diffusion Monte Carlo method allows one to simulate also moderate and shallow lattices. It is analogous to a recent bosonic Monte Carlo method based on the ground-state Path-Integral Monte Carlo algorithm, which has been used to perform a continuous-space simulation of the superfluid-to-insulator transition of hard-sphere bosons in optical lattices, going beyond the single-band approximation [79].

5.3.2 Kohn-Sham band structure

Finally, we give an example of diagonalizing the Kohn-Sham hamiltonian 5.15 self-consistently for a fermionic optical lattice with lattice depth $V_0 = 3E_R$, scattering length $a = 0.04d$, and density at half-filling $n = 1$, of simple cubic geometry. The energy band structure is given in figure 5.2.

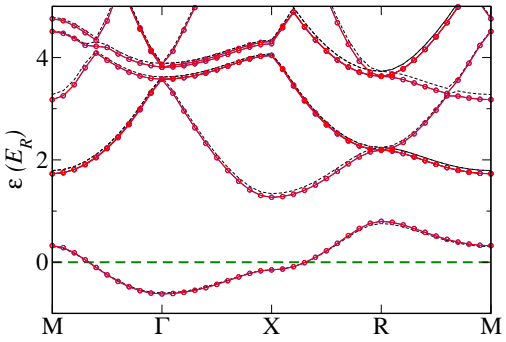

Figure 5.2: Kohn-Sham band structure of fermionic optical lattice with lattice depth $V_0 = 3E_R$, scattering length $a = 0.04d$, and density at half-filling $n = 1$, of simple cubic geometry. The dotted curves correspond to the band structure of free fermions. (The fermi energy is set to be zero by convention.) The ground state band is well separated from the excited bands, as evident in a finite band-gap $\Delta > 0$.

In fact, the band structure $\epsilon_n^\sigma(\mathbf{k})$ completely determines the physics of atomic Fermi gases in weak to moderate optical lattice, in analog to weakly-correlated electrons in material science. An important quantity that derives from the band structure is the density of states

$$D^\sigma(\epsilon) = \sum_{n\mathbf{k}} \delta(\epsilon - \epsilon_n^\sigma(\mathbf{k})) \tag{5.30}$$

which, for instance, could be used as an input into dynamical mean-field theory simulations [56] to improve the accuracy of Kohn-Sham calculations.

Chapter 6

Magnetism in optical lattice

6.1 Introduction

> " ... loadstone attracts iron because it has a soul."
>
> — Thales of Miletus, $\sim$ *585 B.C.*

The peculiar phenomenon of magnetism has been intriguing mankind ever since the times of Thales from Miletus [57]. It took till the year of 1887 for James Clerk Maxwell to summarize all of classical electromagnetism macroscopically in his four equations [2], which motivated Albert Einstein in his theory of special relativity in 1905 [58]. Its enormous success firmly lay the fundamental basis for the entire electrical and electronic engineering today. Microscopically, nature is governed by the laws of quantum mechanics [3], which successfully explain the atomic origin of magnetism. On the weak side, diamagnetism (paramagnetism) is the consequence of orbital (spin) angular momentum coupling in electrons (unpaired electrons) with external magnetic fields [10]. On the strong side, ferromagnetism is a consequence of exchange interactions between electrons [59]. In a tight binding solid without charge degree of freedom, ferromagnetism has been theoretically explained by the Heisenberg model with qualitative success. Besides ferromagnetism, other types of magnetism, such as antiferromagetism and ferrimagnetism, have been discovered over the recent decades to exist in some solids at room temperature [20].

Not only in solids, exotic ferromagnetism has been recently discovered in 2009 to exist in ultracold atomic Fermi gases at extremely low temperatures below 1 nK [60], giving direct experimental evidence to the theoretical prediction for itinerent ferromagnetism described by the Stoner model [59], i.e.

$$\hat{H} = \sum_{\mathbf{k},\sigma} \epsilon_{\mathbf{k}} \hat{c}^{\dagger}_{\mathbf{k}} \hat{c}_{\mathbf{k}} + \frac{1}{2}\frac{U}{N} \sum_{\substack{\mathbf{k}_1\mathbf{k}_2 \\ \mathbf{q}\neq 0}} \hat{c}^{\dagger}_{\mathbf{k}_1+\mathbf{q}\uparrow} \hat{c}^{\dagger}_{\mathbf{k}_2-\mathbf{q}\downarrow} \hat{c}_{\mathbf{k}_2\downarrow} \hat{c}_{\mathbf{k}_1\uparrow} \ . \tag{6.1}$$

It is obvious that solids favour ferromagnetism over gases. Indeed, as will be shown later in this chapter, itinerant ferromagnetism of atomic Fermi gases is stabilized by an optical lattice with increasing laser intensity V_0. Furthermore, calculations from density functional theory recover the antiferromagnetic state towards the Hubbard limit at half-filling, therefore justifying the validation of our theory.

This chapter is based on one of my publications [52].

6.2 Ferromagnetism in optical lattice

6.2.1 Probing ferromagnetism by Kohn-Sham DFT

Calculating the ground-state polarization

$$P = \frac{\rho_\uparrow - \rho_\downarrow}{\rho_\uparrow + \rho_\downarrow} \tag{6.2}$$

for a range of lattice depths V_0, band fillings n, and interaction strengths a/d based on Kohn-Sham density functional theory 5.15, we obtain the phase diagrams shown in figure 6.1.

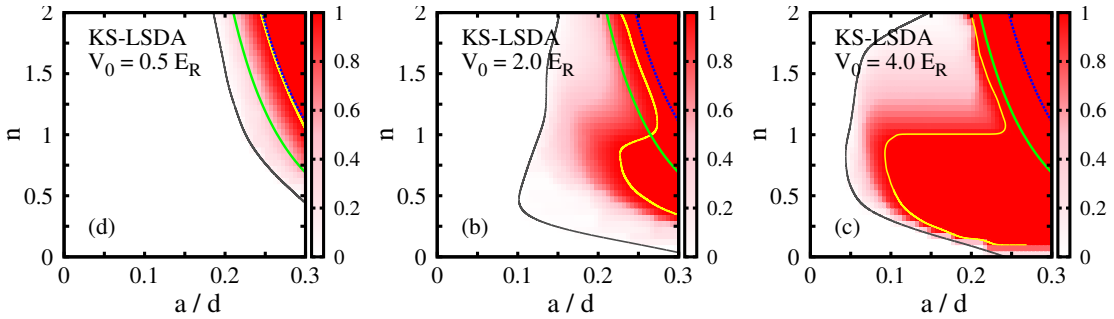

Figure 6.1: **Phase diagrams at fixed optical lattice intensity V_0.** The red-color intensity indicates the polarization P for optical lattice depths (a) $V_0 = 0.5E_R$, (b) $V_0 = 2E_R$, (c) $V_0 = 4E_R$. The green and blue curves indicate, respectively, the transitions to partially and fully polarized phases in homogeneous systems ($V_0 = 0$). The gray and yellow curves indicate the corresponding transitions in the optical lattice. Ferromagnetism dominates in the region of large optical lattice intensity V_0 and scattering length a, where the non-trivial phase boundary arises due to the Kohn-Sham band theory.

In a shallow lattice with $V_0 = 0.5E_R$ (figure 6.1(a)) we see three phases: a paramagnetic phase at weak interactions (white), partially polarized (shown as pink gradations), and fully polarized (ferromagnetic, shown in solid red). The phase boundaries in this shallow lattice are similar to those of the homogeneous system $V_0 = 0$ [70], indicated by the green and blue lines. In deeper optical lattices ($V_0 = 2E_R$ in figure 6.1(b) and $V_0 = 4E_R$ in figure 6.1(c)) polarization sets in at much weaker interactions, indicating that the optical lattice strongly favours itinerant ferromagnetism.

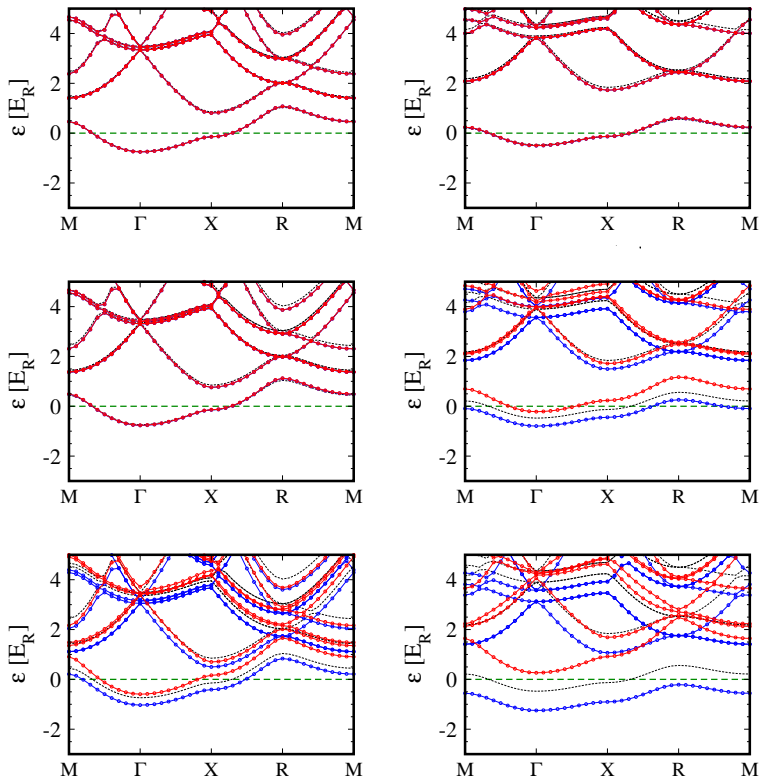

Figure 6.2: **Band structure.** Shown are band structures for two lattice depths, $V_0 = 2E_R$ in the left column and $V_0 = 4E_R$ in the right column, and three values of scattering length ($a = 0.04, 0.08, 0.16\,d$ from top to bottom) at half-filling $n = 1$. The blue and red curve corresponds to the majority and minority spin-component respectively. The black curve is the result for an unpolarized noninteracting gas. Energies are given relative to the chemical potential, shown as a dashed green line at 0. The wave-vector values (given on the x-axis in units of scan a curve which goes through the high symmetry points $\Gamma = (0, 0, 0)$, $\mathrm{X} = (0, \pi/d, 0)$, $\mathrm{R} = (\pi/d, \pi/d, \pi/d)$ and $\mathrm{M} = (\pi/d, \pi/d, 0)$ of the first Brillouin zone.

We can see two prominent features due to the presence of an optical lattice. The first is the much bigger extent of the polarized phases, which is due to the higher local density at the potential minima in the optical lattice, which increases the local density beyond the critical value for polarization. A second striking effect is the non-monotonic behavior of the phase boundary: there is a large fully polarized region at densities up to half filling ($n \leq 1$), which rapidly shrinks at higher filling. This phenomenon is due to band structure effects and a gap between up-spin and down-spin subbands.

Thus we next calculate the detailed band structure of the interacting system, shown in the left panels of figure 6.2, for a weak optical lattice ($V_0 = 2E_R$) without a band gap and on the right for a moderate optical lattice with a band gap ($V_0 = 4E_R$). Weak interactions ($a = 0.04d$) change the band structure only slightly. Increasing the interaction to $a = 0.08d$ (second row) we find a partially polarized state in the deeper lattice: the two spin subbands split and the band structure is substantially changed. At even stronger interaction $a = 0.16d$ (third row) the gas is partially polarized also in the shallower lattice, and becomes fully polarized in the deeper lattice. Note that here the fermions are fully polarized up to half band filling $n = 1$, since only the up-spin subband gets occupied. Notice also that in the fully polarized state the first band is fully occupied and the system is insulating due to the gap between the first and second subbands. Filling the bands further puts fermions in the next band with opposite spin, resulting in a partially polarized state. This explains the sharp feature around $n = 1$ in the phase diagram in figure 6.1(c). To recover full polarization for $n > 1$ one needs to increase either interaction strength or lattice depth to push the energy of the lowest down-spin subband above the second up-spin subband.

6.2.2 Inadequetcy of Hohenberg-Kohn DFT

Figure 6.3(a) and (b) illustrate the inadequetcy of Hohenberg-Kohn density functional theory, where it fails to capture the non-trivial phase boundary for moderate optical lattices that arises due to the Kohn-Sham band structure effects.

The complete absence of band structure effects in HK-LSDA also largely handicaps itself to estimate correctly the density of states of the system as illustrated in figure 6.4.

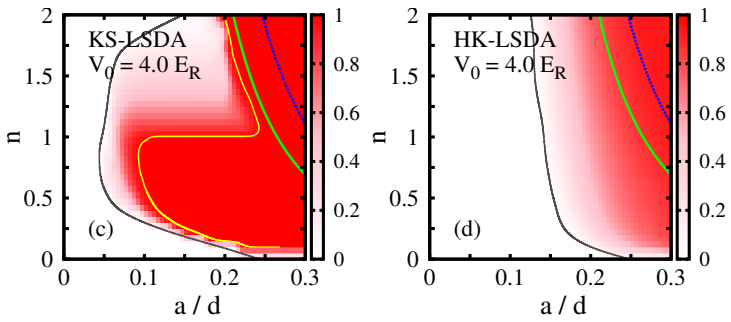

Figure 6.3: **KS-LSDA vs. HK-LSDA phase diagrams at fixed optical lattice intensity V_0.** The red-color intensity indicates the polarization P for optical lattice depths $V_0 = 4E_R$ calculated by (a) KS-LSDA, and by (b) HK=LSDA density functional theory. The green and blue curves indicate, respectively, the transitions to partially and fully polarized phases in homogeneous systems ($V_0 = 0$). The gray and yellow curves indicate the corresponding transitions in the optical lattice. Ferromagnetism dominates in the region of large scattering length a, where the non-trivial phase boundary arises due to the Kohn-Sham band theory, which cannot be captured using HK-LSDA.

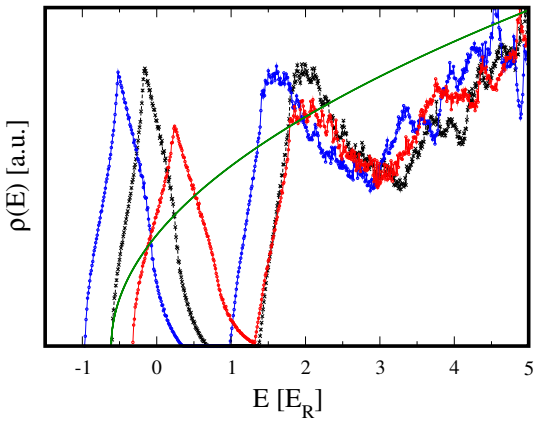

Figure 6.4: **Density of states**. Results of Kohn-Sham DFT calculations at half-filling $n = \rho d^3 = 1$ with optical lattice intensity $V_0 = 3E_R$ and scattering length $a = 0.12d$ are shown indicated by the blue (red) symbols for the majority (minority) spin component. The density of states of the interacting gas is compared to that of non-interacting species (black crosses), and that obtained in the HK-LSDA method (green line), which shows no band gap. The Fermi level is at $E = 0$.

6.3 Antiferromagnetism in optical lattice

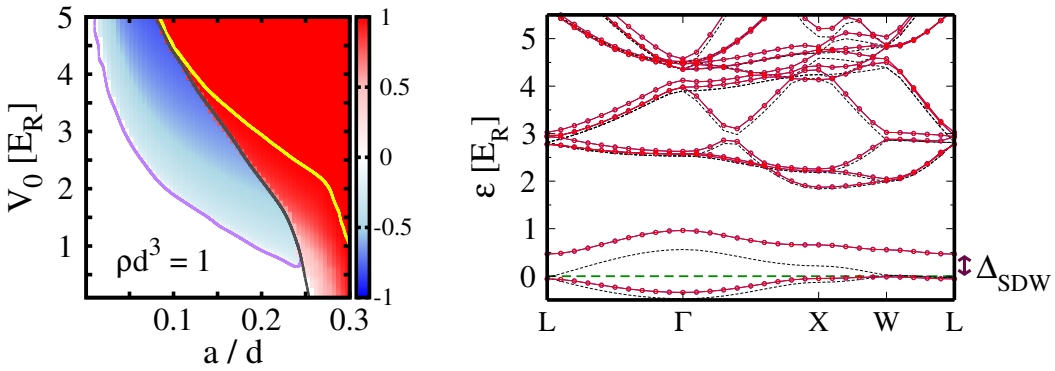

Figure 6.5: **Phase diagram and antiferromagnetic (AF) band structure at half filling** $n = \rho d^3 = 1$**.** Left: Ferromagnetic (antiferromagnetic) phases are indicated by the red-colored polarization (blue-colored staggered polarization). As the scattering length a increases, the fermionic optical lattice undergoes phase transitions from an unpolarized to an antiferromagnetic and finally to ferromagnetic phase. Right: To observe antiferromagnetism, the unit cell has to be doubled, resulting in a face centered cubic (fcc) lattice. A spin-density-wave gap Δ_{SDW} shows up in the antiferromagnetic state of an optical lattice with laser intensity $V_0 = 4E_R$ and scattering length $a = 0.08d$. Here, the high symmetry points are $\Gamma = (0, 0, 0)$, $X = (0, \pi/d, 0)$, $L = (\pi/2d, \pi/2d, \pi/2d)$ and $W = (\pi/2d, \pi/d, 0)$.

To see antiferromagnetism competing with ferromagnetism at half band filling $n = 1$ we need to consider a unit cell consisting of two lattice sites, and compare the energies of antiferromagnetic and uniform configurations. We find, as shown in figure 6.5(a), that antiferromagnetic ordering is preferred at intermediate interaction strengths and half band filling, matching with the single band Hubbard model physics that becomes valid in the upper left hand corner of the shown phase diagram.

Last but not least, antiferromagnetic symmetry breaking opens up an additional spin-density-wave (SDW) gap Δ_{SDW} in the folded ground-state band as shown in figure 6.5(b). This provides experimentalists an indirect method to probe for antiferromagnetism in fermionic optical lattices.

Chapter 7

Conclusion and outlook

This thesis explores the bridge between the theories and experiments of three-dimensional optical lattices, through large-scale computational numerics in the quantitative aspect.

Experiments with bosons at equilibrium have been largely successful in developing state-of-art techniques to probe for time-of-flight images [32], as well as in-situ density profiles up to the precision of single-site resolution [36]. On the other hand, the theoretical picture of describing by the boson Hubbard model has been quantitatively confirmed with numerical-exact large scale Quantum Monte Carlo simulations implemented in the directed worm algorithm [41, 42], at least for the time-of-flight images [32]. New theoretical proposals are currently made feasible due to the high precision in experiments, in particularly the fluctuation-dissipation thermometry scheme [49, 47]. In this thesis, we perfected this concept proposed by Zhou and Ho [49] for bosonic optical lattices in reality by reducing the undesirable noise through window sizing technique. This modified scheme has been numerically tested to give realiable estimates of the thermodynamic temperature even in the presence of various experimental imperfections, therefore proving itself to be a feasible quantitative thermometer for optical lattices. Highlighted in this thesis is also the wing thermometry scheme which is numerically tested to work for large enough normal-wings of the bosonic cloud. As the bosonic cloud increases in size for future experiments, the normal-wings get spread out due to waist effects, therefore enhancing the feasibility of the wing thermometry scheme in the soon coming future.

Future experiments with bosons will involve a much bigger bosonic cloud with different lattice geometries at lower temperatures, thereby challenging the theoretical limits of numerical computation for direct quantitative validations. Facing this challenge, we need therefore an ultra-robust implementation of the QMC di-

rected worm algorithm [42] that can handle simulations of that monstrous scale. For the benefit of the scientific community, we decide to publish our code[1] which has been designed for such purposes. Its performance is ultra-robust, such that it could handle simulations of up to some 10 million lattice sites numerical-exactly, and some of which manage to converge in a couple of hours. In fact, this is definitely one of the fastest, if not the fastest, in the world till date.

Luck, on the other hand, is not (yet) with the fermions. Current experiments with fermions are still relatively hot to realize the conjectured antiferromagnetic or superconducting phases predicted from theory. While the experimentalists are tediously cooling the fermions, the theoreticians are also questing to solve the Hubbard model which is believed to be the theory behind high-Tc superconductors as well as other strongly-correlated materials. Handicapped by the notorious negative-sign problem for fermions, Quantum Monte Carlo methods prove to be pretty undesirable. Motivated by the success of density functional theory for conventional materials, we apply it for the first time to ultracold fermions in a shallow optical lattice. We find that Stoner ferromagnetism, which was recently discovered to exist in ultracold fermionic gases [60], gets stablized by the optical lattice due to band structure effects. Besides, the antiferromagnetic phase is recovered qualitatively in the Hubbard model limit at half-filling by density functional theory, in which we find the existence of a spin-density-wave gap that could be used as an indirect probe for antiferromagentism in future experiments.

Perhaps not in the distant future would optical lattices be eventually realized as quantum emulators, thereby solving the long theoretical puzzle of strongly-correlated physics. Only by then could new materials with surprisingly exotic properties be predicted and engineered, which is in fact the ultimate aim of the optical lattice emulator (OLE) project. Today, optical lattices provide a vast unprecented opportunity to explore also the non-equilibrium dynamics of quantum many-body systems, and it is the view of the author that we will embrace a new era of quantum engineering for our human civilization in the coming decades.

[1]The DWA code is published in reference [61] as a part of the ALPS project. It is written in C++ for maximal performance, and interfaced in Python for easy data management and analysis. It has been designed for easy automation of large-scale simulation chains. With ALPS, the DWA code can now handle robustly large datasets, as well as lattice geometries of all kinds.

Appendix A

Implementing quantitative simulations

A.1 Optical lattice bandstructure

A three-dimensional optical lattice is setup by 3 pairs of counter-propagating laser beams in orthogonal directions with lattice intensity $\vec{V_0} = (V_{0x}, V_{0y}, V_{0z})$ and wavelength $\vec{\lambda} = (\lambda_x, \lambda_y, \lambda_z)$. In units of lattice spacing $\vec{d} = \vec{\lambda}/2$, and recoil energy $\vec{E}_R = \frac{h^2}{2m}\left(\frac{1}{\lambda_x^2}, \frac{1}{\lambda_y^2}, \frac{1}{\lambda_z^2}\right)$, the single particle Bloch hamiltonian [38] reads

$$\hat{H}_k = \frac{1}{\pi^2}\left(-i\nabla + 2\pi\vec{k}\right)^2 + \sum_{\alpha=x,y,z} V_{0\alpha}\sin^2(\pi x_\alpha) \tag{A.1}$$

which is clearly separable. Along a direction, say x, the eigenvalue problem is reduced to

$$\left[\frac{1}{\pi^2}\left(-i\partial_x + 2\pi k_x\right)^2 + V_{0x}\sin^2(\pi x)\right] u_{k_x}(x) = \epsilon_{k_x} u_{k_x}(x) \tag{A.2}$$

with $k_x = 0, \frac{1}{L}, \cdots, \frac{L-1}{L}$ for a periodic lattice of size L^3. Expanding in the plane wave basis,

$$u_{k_x}(x) = \frac{1}{\sqrt{L}} \sum_{G=0,\pm1,\pm2\cdots} c_G^{(k_x)} e^{i2\pi G x} \ , \tag{A.3}$$

equation A.4 becomes the following tridiagonal eigenvalue problem

$$\left(4\left(G + k_x\right)^2 + \frac{V_{0x}}{2}\right) c_G^{(k_x)} - \frac{V_{0x}}{4} c_{G-1}^{(k_x)} - \frac{V_{0x}}{4} c_{G+1}^{(k_x)} = \epsilon_{k_x} c_G^{(k_x)} \ . \tag{A.4}$$

The wannier function is defined as

$$w_x(x) = \frac{1}{\sqrt{L}} \sum_{k_x} u_{k_x}(x) e^{i2\pi k_x x} = \frac{1}{L} \sum_{k_x} \sum_{G} c_G^{(k_x)} e^{i2\pi(G+k_x)x} \ . \tag{A.5}$$

Important bandstructure parameters are the hopping strength

$$t_x = -\frac{1}{L}\sum_{k_x} \epsilon_{k_x} e^{-i2\pi k_x} \tag{A.6}$$

(likewise for t_y and t_z), and the onsite interaction strength

$$U = g\int |w(\vec{r})|^4\, d\vec{r} = \frac{4\pi a_s \hbar^2}{m}\int |w(\vec{r})|^4\, d\vec{r} \tag{A.7}$$

where a_s is the s-wave scattering length easily tunable via Feshbach resonance technique. Finally, the Fourier transform of the wannier function is

$$\tilde{w}_x(q_x) = \frac{1}{\sqrt{L}}\int w_x(x) e^{-i2\pi q_x x}\, dx = \frac{1}{\sqrt{L}}\sum_{k_x}\sum_{G} c_G^{(k_x)} \delta_{q_x, G+k_x}\ . \tag{A.8}$$

Easy implementation is available in the Python interface, for example:

```
>>> import numpy;
>>> import pyalps.dwa;
>>>
>>> V0   = numpy.array([8.805, 8. ,  8. ]); #lattice strength [Er]
>>> wlen = numpy.array([765., 843., 843.]); #laser wavelength [nm]
>>> a    = 101;    #s-wave scattering length [bohr radius]
>>> m    = 86.99;  #mass [a.m.u.]
>>> L    = 160;    #lattice of size L^3
>>>
>>> band = pyalps.dwa.bandstructure(V0, wlen, a, m, L);
>>>
>>> band

Optical lattice:
================
V0    [Er] = 8.805  8   8
lamda [nm] = 765    843 843
Er2nK      = 188.086    154.89  154.89
L          = 160
g          = 5.51132

Band structure:
===============
t [nK] : 4.77257    4.77051 4.77051
U [nK] : 38.7027
U/t    : 8.1094 8.1129  8.1129
```

A.2 Expression for finite time-of-flight

To probe for momentum distribution, the optical lattice is momentarily turned off, and the bosons expand freely with momentum gained from the previous lattice momentum. Measurements are performed in our classical world, and therefore semiclassical treatment is already sufficient, i.e.

$$\hbar\vec{k} = m\left(\frac{\vec{r}}{t_f}\right) \tag{A.9}$$

where t_f is the actual time of flight taken by the bosons to move from the origin (experiment) to the detector probe at position $\vec{r}$. Here, we assume that

1. there is no interaction and collision among the bosons as they fly apart;
2. the bosons move at constant speed during their entire flight.

In the limit of infinite t_f, the time-of-flight image captures

$$\langle n_f(\vec{r})\rangle = \left(\frac{m}{\hbar t_f}\right)^3 \left|\tilde{w}\left(\frac{m}{\hbar t_f}\vec{r}\right)\right|^2 S(\vec{k}) \ . \tag{A.10}$$

To start with the correction due to dynamics, we consider the time evolution of the time-dependent wannier wavepacket that orginates from site j

$$\mathcal{W}_j(\vec{r}, t_f) = \left(\frac{m}{\hbar t_f}\right)^{3/2} \tilde{w}\left(\frac{m}{\hbar t_f}(\vec{r} - \vec{r}_j)\right) \exp\left(-\frac{i\epsilon_k t_f}{\hbar}\right) \ , \tag{A.11}$$

where

$$\epsilon_k = \frac{\hbar^2 k^2}{2m} = \frac{\hbar^2}{2m}\left(\frac{m}{\hbar t_f}\right)^2 (\vec{r} - \vec{r}_j)^2 \ . \tag{A.12}$$

Ignoring the initial-site dependence on the wannier enveloped function, the time-of-flight image captures

$$\begin{aligned} \langle n_f(\vec{r})\rangle \ \approx \ & \left(\frac{m}{\hbar t_f}\right)^3 \left|\tilde{w}\left(\frac{m}{\hbar t_f}\vec{r}\right)\right|^2 \sum_{i,j}\langle \hat{b}_i^\dagger \hat{b}_j\rangle \\ & \times \exp\left(-\frac{i}{\hbar}\frac{\hbar^2}{2m}\left(\frac{m}{\hbar t_f}\right)^2 (\vec{r} - \vec{r}_i)^2 t_f\right) \\ & \times \exp\left(\frac{i}{\hbar}\frac{\hbar^2}{2m}\left(\frac{m}{\hbar t_f}\right)^2 (\vec{r} - \vec{r}_j)^2 t_f\right) \end{aligned} \tag{A.13}$$

at finite t_f, therefore arriving at the final expression

$$\langle n_f(\vec{k})\rangle \approx |\tilde{w}(\vec{k})|^2 \sum_{i,j} \langle \hat{b}_i^\dagger \hat{b}_j \rangle \, e^{i\vec{k}\cdot(\vec{r}_i-\vec{r}_j)-i\gamma_f(r_i^2-r_j^2)} \ . \tag{4.6}$$

The time-of-flight phase γ_f can be easily evaluated in Python, for example:

```
>>> import pyalps.dwa
>>> pyalps.dwa.tofPhase(time_of_flight=15.5, wavelength
    =[843,765,765], mass=86.99)
[0.007850080468935228, 0.006464602556863682, 0.006464602556863682]
```

A.3 Obtaining time-of-flight image

This section illustrates how one can easily obtain the time-of-flight images, say figure 4.1 for example, using the Python interface.

```
import numpy;
import numpy.fft;
import pyalps;
import pyalps.dwa;
import matplotlib.pyplot;
from mpl_toolkits.mplot3d.axes3d import Axes3D;

resultFile       = pyalps.getResultFiles()[0];
L                = int(pyalps.getParameters(resultFile)[0]['L']);
green_tof        = pyalps.getMeasurements(resultFile, observable='
    Green Function:TOF')[0]['mean']['value'].reshape([L,L,L]);
momentum_density = numpy.fft.fftn(green_tof).real;

V0   = numpy.array([8.8, 8.,  8.]);
wlen = numpy.array([765., 843., 843.]);
a    = 101;
m    = 86.99;
band = pyalps.dwa.bandstructure(V0, wlen, a, m, L);

q_z   = numpy.array(band.q(2));
wk2_z = numpy.array(band.wk2(2));
wk2_z = numpy.array([q_z, wk2_z]).transpose();
wk2_z0= wk2_z[wk2_z[:,0] == 0.][0][1];
wk2_z = numpy.transpose(wk2_z[wk2_z[:,1]/wk2_z0 > 1e-4]);
q_z   = wk2_z[0]
wk2_z = wk2_z[1]

momentum_density = numpy.tile(momentum_density, reps=(1,1,2*((q_z[
    q_z[:] >= 0].size / L)+1)));
```

```
dummy = numpy.zeros(momentum_density.shape[2]);
dummy[dummy.size/2:dummy.size/2 + q_z[q_z[:] >= 0].size] = wk2_z[
    q_z[:] >= 0]
dummy[dummy.size/2-q_z[q_z[:] < 0].size:dummy.size/2]  = wk2_z[q_z
    [:] < 0]

momentum_density = numpy.tensordot(momentum_density, dummy, axes
    =([2],[0]))
momentum_density = numpy.tile(momentum_density, reps=(4,4));

q_x   = numpy.array(band.q(0));
wk2_x = numpy.array(band.wk2(0));
wk2_x = wk2_x[(q_x[:] >= -2.)*(q_x[:] < 2.)];
q_x   = q_x[(q_x[:] >= -2.)*(q_x[:] < 2.)]

q_y   = numpy.array(band.q(1));
wk2_y = numpy.array(band.wk2(1));
wk2_y = wk2_y[(q_y[:] >= -2.)*(q_y[:] < 2.)];
q_y   = q_y[(q_y[:] >= -2.)*(q_y[:] < 2.)]

wk2 = numpy.outer(wk2_x, wk2_y);

q_x = numpy.array([q_x] * wk2.shape[1], float);
q_y = numpy.array([q_y] * wk2.shape[0], float).transpose();
tof_image = wk2 * momentum_density;

mag = L/10;
q_x = q_x[0:q_x.shape[0]:mag, 0:q_x.shape[1]:mag];
q_y = q_y[0:q_y.shape[0]:mag, 0:q_y.shape[1]:mag];
tof_image = tof_image[0:tof_image.shape[0]:mag, 0:tof_image.shape
    [1]:mag] * mag * mag

fig = matplotlib.pyplot.figure();
ax = fig.add_subplot(1, 1, 1, projection='3d')
surf = ax.plot_surface( q_y, q_x, tof_image,
                        rstride=1, cstride=1, cmap=matplotlib.cm.
                            coolwarm, linewidth=0, antialiased=
                            False)
fig.colorbar(surf, shrink=0.5, aspect=10);
fig.show();
```

Further detailed information can be found in reference [61].

A.4 Obtaining density profile

This section illustrates how one can easily obtain the density profiles, say figure 4.2 for example, using the Python interface.

```
import numpy;
import pyalps;
import pyalps.dwa;
import matplotlib.pyplot;
from mpl_toolkits.mplot3d.axes3d import Axes3D;

resultFile = pyalps.getResultFiles()[0];
L          = int(pyalps.getParameters(resultFile)[0]['L']);
density    = pyalps.getMeasurements(resultFile, observable='Local
    Density')[0]['mean']['value'].reshape([L,L,L]);
cross_section_density = density[:,:,L/2];
column_integrated_density = numpy.sum(density, axis=2);
x = numpy.array([range(L)] * L, float) - (L-1)/2.;
y = numpy.transpose(x);

# Plotting cross sectional density profile
fig1 = matplotlib.pyplot.figure();
ax = fig1.add_subplot(1, 1, 1, projection='3d')
surf = ax.plot_surface( x, y, cross_section_density,
                        rstride=1, cstride=1, cmap=matplotlib.cm.
                            coolwarm, linewidth=0, antialiased=
                            False)
fig1.colorbar(surf, shrink=0.5, aspect=10);
fig1.show();

# Plotting column integrated density profile
fig2 = matplotlib.pyplot.figure();
ax = fig2.add_subplot(1, 1, 1, projection='3d')
surf = ax.plot_surface( x, y, column_integrated_density,
                        rstride=1, cstride=1, cmap=matplotlib.cm.
                            coolwarm, linewidth=0, antialiased=
                            False)
fig2.colorbar(surf, shrink=0.5, aspect=10);
fig2.show();
```

Further detailed information can be found in reference [61].

A.5 Fixing $\langle N \rangle$ by tuning chemical potential

In this section, we shall work through part of the example of quantifying the error budget due to a $\pm 5\%$ fluctuation in lattice strength V_{0x} to illustrate how easily the chemical potential can be conviently tuned in the Python interface. (See table 4.1.)

A.5.1 Initial simulations

The first step is to scan a certain range of chemical potentials μ in the initial simulations.

The following prepares the parameter files for the initial simulations in the Python interface:

```
import numpy;
import pyalps;
import pyalps.dwa;

tof_phase = pyalps.dwa.tofPhase(time_of_flight=15.5, wavelength
    =[765,843,843], mass=86.99)

ps = [];
for ratio in [0.96, 0.97, 0.98, 0.99, 1.00, 1.01, 1.02, 1.03,
    1.04]:
  V0   = numpy.array([ratio*8.805, 8. ,  8. ]);
  wlen = numpy.array([765., 843., 843.]);
  a    = 101;
  m    = 86.99;
  L    = 160;

  band = pyalps.dwa.bandstructure(V0, wlen, a, m, L);
  p = {};
  p.update({'ratio_V0x' : ratio , 'U' : band.Ut()[2] , 'tx_t' :
      band.t()[0]/band.t()[2]})
  ps.append(p);

params=[]
for p in ps:
  for ratio in [0.8, 0.82, 0.84, 0.88, 0.9, 0.92, 0.94, 0.96,
      0.98, 1.00, 1.02, 1.04, 1.06, 1.08, 1.10, 1.12, 1.14, 1.16,
      1.18, 1.2]:
    params.append(
      { 'LATTICE'          : 'inhomogeneous simple cubic lattice'
      , 'MODEL'            : 'boson Hubbard'
      , 'L'                : 160
      , 'Nmax'             : 20
```

```
      , 'ratio_V0x'        : p['ratio_V0x']
      , 't'                : 1.
      , 'tx_t'             : p['tx_t']
      , 'U'                : p['U']
      , 'T'                : 1.
      , 'mu_homogeneous'   : ratio*4.0265
      , 'mu'               : 'mu_homogeneous - (0.0073752*(x-(L-1)
          /2.)*(x-(L-1)/2.) + 0.0036849*(y-(L-1)/2.)*(y-(L-1)/2.)
          + 0.0039068155*(z-(L-1)/2.)*(z-(L-1)/2.))'
      , 'tof_phase'        : str(tof_phase)
      , 'SWEEPS'           : 100000
      , 'SKIP'             : 100
      }
    )

h5_infiles = pyalps.writeInputH5Files("errorbudget.V0",params);
```

The next step is thermalization, i.e.

```
for taskfile in h5_infiles:
  pyalps.dwa.recursiveRun(
    "pyalps.runApplication('dwa', taskfile)" ,
    cmd_lang = 'python' ,
    follow_up_script = "pyalps.dwa.extract_worldlines(infile=
        pyalps.input2output(taskfile), outfile=taskfile)" ,
    break_if = "pyalps.dwa.thermalized(pyalps.input2output(
        taskfile), 'Total Particle Number', simplified=True)" ,
    write_status = "pyalps.dwa.write_status(pyalps.input2output(
        taskfile), 'Thermalizing')" ,
    loc = locals()
  );
```

followed by convergence of $\langle N \rangle$, i.e.

```
for taskfile in h5_infiles:
  pyalps.dwa.recursiveRun(
    "pyalps.runApplication('dwa', pyalps.input2output(taskfile))"
        ,
    cmd_lang = 'python' ,
    break_if = "pyalps.dwa.converged(pyalps.input2output(taskfile)
        , 'Total Particle Number', simplified=True)" ,
    write_status = "pyalps.dwa.write_status(pyalps.input2output(
        taskfile), 'Converging')" ,
    loc = locals()
  );
```

A.5.2 Tuning chemical potential

Next, we prepare the new parameter files for a new interpolated value of chemical potentials:

```
resultFiles = pyalps.getResultFiles(prefix='errorbudget.V0');
data = pyalps.loadMeasurements(resultFiles, 'Total Particle Number
    ');
params = pyalps.paramsAtFixedY(data, x='mu_homogeneous', y='Total
    Particle Number', foreach=['ratio_V0x'], fixedY=280000);

h5_infiles = pyalps.writeInputH5Files("errorbudget.V0.1",params);
```

and we perform the new simulations similar to before. This process is repeated until one is satisfied with the accuray of the interpolated chemical potential.

A.5.3 Turning on measurements

After one is satisfied with the correct chemical potential, the measurements for density profile and green function can be turned on

```
for h5_infile in h5_infiles:
  pyalps.dwa.switchParameter(h5_infile, 'MEASURE[Local Density]',
      1);
  pyalps.dwa.switchParameter(h5_infile, 'MEASURE[Green Function]',
       1);
```

for the simulations to run and collect statistics till satisfaction.

Further detailed information can be found in reference [61].

Appendix B

Energy functional for repulsive Fermi gas

B.1 Energy functional

The objective is to determine the energy functional, or equation of state, of the homogeneous Fermi gas at zero temperature by Fixed-Node Diffusion Monte Carlo (FN-DMC) method. This technique has been popularly employed in several studies of the ground-state properties of resonantly interacting Fermi gases with balanced [62, 63] as well as imbalanced [64, 65, 66] populations of the two components. Despite the fact that – to circumvent the sign problem – one has to introduce the fixed-node constraint, meaning that the ground-state wave function is forced to have the same nodal surface as a trial wave function, FN-DMC has proven to be extremely accurate. It provides a rigorous upper bound for the ground-state energy, which is exact if the nodes of the trial wave function coincide with those of the exact ground state. Predictions for the ground-state energies obtained with this technique have been benchmarked against experimental results for the low temperature equations of state of both normal and superfluid atomic gases on the attractive branch of Feshbach resonances [67, 68]. In this appendix, we will extend the same technique to the repulsive branch [52].

Other than the fixed node approximation for interacting fermions, diffusion Monte Carlo is numerically exact with any suitable choice of initial trial wavefunction $\psi_T(\mathbf{r}_1^\uparrow, \cdots, \mathbf{r}_{N_\uparrow}^\uparrow, \mathbf{r}_1^\downarrow, \cdots, \mathbf{r}_{N_\downarrow}^\downarrow)$ (or simply $\psi_T(\{\mathbf{r}_i^\uparrow\}, \{\mathbf{r}_{i'}^\downarrow\})$ for $N_\uparrow$ spin-up and $N_\downarrow$ spin-down fermions [69]. We adopt the Jastrow-Slater form [70]

$$\psi_T(\{\mathbf{r}_i^\uparrow\}, \{\mathbf{r}_{i'}^\downarrow\}) = \prod_{i,i'} f(|\mathbf{r}_i^\uparrow - \mathbf{r}_{i'}^\downarrow|) \det(\phi_j^\uparrow(\mathbf{r}_i^\uparrow)) \det(\phi_{j'}^\downarrow(\mathbf{r}_{i'}^\downarrow)) \,; \tag{B.1}$$

where the positive-definite Jastrow correlation term $f(r)$ between unlike spin fermions is obtained from the solution of the two-body scattering problem in free space

$$-\frac{\hbar^2}{m}\frac{\partial^2}{\partial r^2}f(r) + V_{\rm int}(r)f(r) = \epsilon_{\rm int}f(r) \tag{B.2}$$

$(0 < r < L)$. Here, $V_{\rm int}(r)$ is chosen to be the hardcore scattering potential that reproduces the s-wave scattering length a_s at long range, and $f(r)$ is chosen correspondingly with the lowest positive eigenvalue $\epsilon_{\rm int}$ as well as its derivative $f'(r = L/2) = 0$. $\phi_j^{\uparrow}(\mathbf{r}_i^{\uparrow})$ and $\phi_{j'}^{\downarrow}(\mathbf{r}_{i'}^{\downarrow})$ are plane wave orbitals.

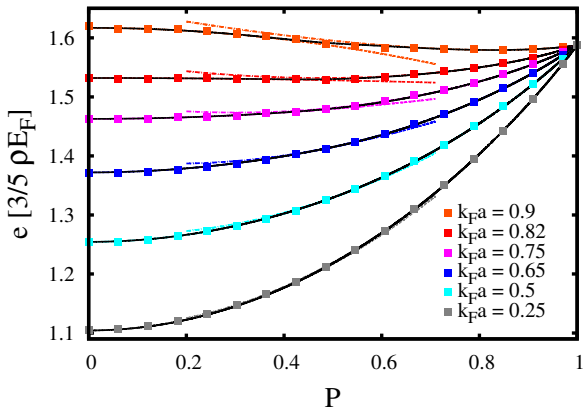

Figure B.1: (color on-line). Energy per volume as a function of the polarization for different values of the interaction parameter $k_F a$. Squares are Monte Carlo data, solid (black) lines the global energy function equation (B.5), dashed and dot-dashed lines represent the low-P and large-P expansions, equations (B.8) and (B.11), respectively.

The ground-state energy per volume of the repulsive Fermi gas $\epsilon = \epsilon(k_F a, P)$ is a functional in terms of the interaction parameter

$$k_F a = (3\pi^2\rho)^{1/3}a \tag{B.3}$$

(where $\rho = \rho_\uparrow + \rho_\downarrow$ is the total density), and the polarization

$$P = \frac{\rho_\uparrow - \rho_\downarrow}{\rho_\uparrow + \rho_\downarrow}\ . \tag{B.4}$$

The energy density $\epsilon(k_F a, P)$ interpolates between its small polarization limit $\epsilon_<(k_F a, P)$ and its large polarization limit $\epsilon_>(k_F a, P)$, i.e.

$$\epsilon(k_F a, P) = \Big(1 - f_{\rm damp}(P)\Big)\epsilon_<(k_F a, P) \ + \ \Big(f_{\rm damp}(P)\Big)\epsilon_>(k_F a, P)\ . \tag{B.5}$$

through a damping function

$$f_{\rm damp}(P) = \frac{1}{2}\Big(1 + \tanh\Big[2\pi C_{\rm damp1}\left(P - C_{\rm damp2}\right)\Big]\Big) \tag{B.6}$$

such that the coefficient $C_{\rm damp1} = 1.8$ determines the steepness, and $C_{\rm damp2} = 0.5$ is the center of the transition region. Figure B.1 illustrates the energy density (B.5), the small and large polarization limits. All raw quantum Monte Carlo data are reported in publication [52]. Finally, the hartree-exchange-correlation energy density is obtained by subracting the Thomas-Fermi components 5.8, i.e.

$$\epsilon_{\rm HXC}(k_F a, P) = \epsilon(k_F a, P) - \frac{3}{5}\rho_\uparrow E_{F\uparrow} - \frac{3}{5}\rho_\downarrow E_{F\downarrow}\ . \tag{B.7}$$

B.2 Analytic behavior at polarization limits

At small population imbalance, the energy density is quadratic in the polarization, i.e.

$$\epsilon_<(k_F a, P) = \frac{3}{5}\rho E_F\left[\epsilon_0\left(k_F a\right) + \frac{5}{9}P^2\chi^{-1}\left(k_F a\right)\right]\ . \tag{B.8}$$

In units of $\frac{3}{5}\rho E_F = \frac{3}{5}\rho\frac{\hbar^2 k_F^2}{2m}$, the energy of unpolarized Fermi gas is expressed in a

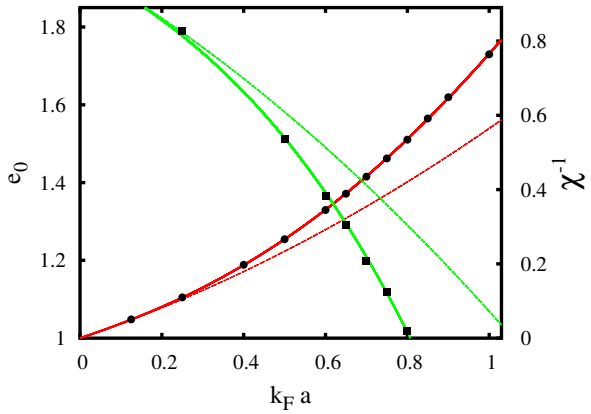

Figure B.2: (color on-line). Energy per volume (circles, left axis) and inverse magnetic susceptibility (squares, right axis) of the unpolarized Fermi gas. Units are the ideal Fermi gas values, $3/5\rho E_F$ and $\chi_0 = 3\rho/(2E_F)$, respectively. Solid lines are the fitting functions (B.9) in red and (B.10) in green, while the dashed lines correspond to second order perturbation theory.

Taylor expansion of $(k_F a)$ as

$$\epsilon_0(k_F a) = 1 + C_{E1}(k_F a) + C_{E2}(k_F a)^2 + C_{E3}(k_F a)^3 + C_{E4}(k_F a)^4\ , \tag{B.9}$$

and likewise for the inverse of the magnetic susceptibility

$$\chi^{-1}(k_F a) = 1 - C_{\chi 1} k_F a - C_{\chi 2}(k_F a)^2 - C_{\chi 3}(k_F a)^3 . \tag{B.10}$$

The coefficients $C_{E1} = 0.3536$, $C_{E2} = 0.1855$, $C_{\chi 1} = 0.6366$ and $C_{\chi 2} = 0.2911$ have been determined using second order perturbation theory [71, 72, 73, 74, 75], while we obtain $C_{E3} = 0.307(7)$, $C_{E4} = -0.115(8)$ and $C_{\chi 3} = 0.56(1)$ from a best-fit to the Monte Carlo results with zero or small population imbalance (in the range $k_F a \leq 1$ and $P \leq 0.5$). Figure The functions $\epsilon_0(k_F a)$ and $\chi^{-1}(k_F a)$ are shown in figure B.2.

At large population imbalance the behavior of a normal Fermi gas is well described by the Landau-Pomeranchuk hamiltonian [65, 76, 70]. In this approach, the minority component is regarded as a gas of weakly interacting quasiparticles, called Fermi polarons. In this limit, the energy density

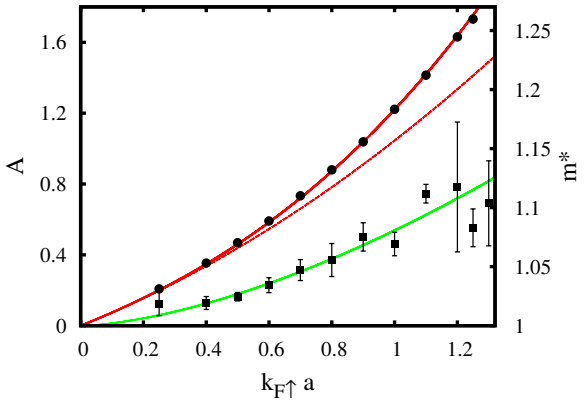

Figure B.3: (color on-line). Chemical potential at zero concentration (circles, left axis) and effective mass (squares, right axis) of the repulsive polaron. Units are $3/5 E_{F\uparrow}$ and bare atomic mass, respectively. Solid lines are the fitting functions (B.14) in red and (B.15) in green. The dashed line is the chemical potential in second order perturbation theory.

$$e_>(k_{F\uparrow} a, x) = \frac{3}{5}\rho_\uparrow E_{F\uparrow}\left[1 + A(k_{F\uparrow} a)x + F(k_{F\uparrow} a)x^2 + \frac{x^{5/3}}{m^*(k_{F\uparrow} a)}\right] \tag{B.11}$$

is characterized by the interaction parameter

$$k_{F\uparrow} a = (6\pi^2 \rho_\uparrow)^{1/3} a \tag{B.12}$$

of the majority component, and the concentration

$$x = \frac{1-P}{1+P} \tag{B.13}$$

of the minority compoent. In units of $\frac{3}{5}\rho_\uparrow E_{F\uparrow}$, $A(k_{F\uparrow}a)$ represents the polaron chemical potential at zero concentration, i.e.

$$A(k_{F\uparrow}a) = \frac{5}{3}\Big[C_{A1}(k_{F\uparrow}a) + C_{A2}\,(k_{F\uparrow}a)^2 + C_{A3}\,(k_{F\uparrow}a)^3\Big]\ . \tag{B.14}$$

Second order perturbation theory [76, 77, 78] gives the first two coefficients $C_{A1} = 0.4244$ and $C_{A2} = 0.2026$, while $C_{A3} = 0.105(2)$ results from a best-fit to Monte Carlo data for the energy of a single spin-down impurity immersed in the Fermi sea of spin-up (majority component) particles. The polaron effective mass m^* is extracted from the dispersion relation of an impurity with finite momentum. We parametrize the interaction parameter dependence of this effective mass (in units of the bare atomic mass) as

$$m^*(k_{F\uparrow}a) = 1 + C_{m^*1}(k_{F\uparrow}a)^{C_{m^*2}} \tag{B.15}$$

where $C_{m^*1} = 0.0807(50)$ and $C_{m^*2} = 1.59(15)$. The functions $A(k_{F\uparrow}a)$ and $m^*(k_{F\uparrow}a)$ are shown in fig. B.3. Parametrizing

$$F(k_{F\uparrow}a) = C_F(k_{F\uparrow}a)^2\ , \tag{B.16}$$

the coefficient $C_F = 0.419(4)$ is obtained from fitting the Monte Carlo data for a highly imbalanced Fermi gas ($x \lesssim 0.5$) via inserting equation B.14 and B.15 into the Landau-Pomeranchuck functional.

To facilitate the implementation of the functional, we summarize the values of all of the coefficients in the following table.

$C_{\text{damp1}} = 1.8$	$C_{\chi1} = 0.6366$	$C_{m^*1} = 0.0807$
$C_{\text{damp2}} = 0.5$	$C_{\chi2} = 0.2911$	$C_{m^*2} = 1.59$
$C_{E1} = 0.3536$	$C_{\chi3} = 0.56$	$C_F = 0.419$
$C_{E2} = 0.1855$	$C_{A1} = 0.4244$	
$C_{E3} = 0.307$	$C_{A2} = 0.2026$	
$C_{E4} = -0.115$	$C_{A3} = 0.105$	

Bibliography

[1] H. Goldstein, C. P. Poole, and J. L. Safko, *Classical mechanics*, Addison Wesley (2001).

[2] J. D. Jackson, *Classical electrodynamics*, Wiley (1998).

[3] F. Schwabl, *Quantum Mechanics*, Springer (2007).

[4] E. Schrödinger, *Quantisierung als Eigenwertproblem*, Annalen der Physik **79**, 361-376 (1926).

[5] M. Born, *Zur Quantenmechanik der Stoβvorgänge*, Z. Phys. **37**, 863 (1926).

[6] F. Schwabl, *Advanced Quantum Mechanics*, Springer (2008).

[7] S. N. Bose, *Plancks Gesetz und Lichtquantenhypothese*, Zeitschrift für Physik **26**, 178-181 (1924).

[8] E. Fermi, *Sulla quantizzazione del gas perfetto monoatomico*, Rendiconti Lincei **3**, 145-9 (1926).

[9] P. A. M. Dirac, *On the theory of quantum mechanics*, Proc. Royal Soc. A **112**, 661-77 (1926).

[10] R. K. Pathria, *Statistical mechanics*, Elsevier (2001).

[11] F. Bloch, *Über die Quantenmechanik der Elektronen in Kristallgittern*, Z. Phys. **52**, 555 (1928).

[12] S. M. Sze, K. K. Ng, *Physics of semiconductor devices*, John Wiley & Sons (2006).

[13] A. G. Levine, *John Bardeen, William Shockley, Walter BrattainÑInvention of the Transistor*, APS (2008).

[14] N. Chandler, *How transistors work*, http://electronics.howstuffworks.com/transistor4.htm (2012).

[15] S. J. Tans, A. R. M. Verschueren, and C. Dekker, *Room-temperature transistor based on a single carbon nanotube*, Nature **393**, 49-52 (1998).

[16] J. Bonnet, P. Yin, M. E. Ortiz, P. Subsoontorn, and D. Endy, *Amplifying genetic logic gates* Science 1232758 (2013).

[17] W. Kohn, and L. J. Sham, *Self-consistent equations including exchange and correlation effects*, Physical Review **140**, A1133-A1138 (1965).

[18] L. Hedin, *New method for calculating the one-particle Green's function with application to the electron-gas problem*, Phys. Rev. **139**, A796-A823 (1965).

[19] P. Fulde, *Electron correlations in molecules and solids*, Springer (2002).

[20] Wikipedia, *Ferromagnetism*, http://en.wikipedia.org/wiki/Ferromagnetism (2013).

[21] J. G. Bednorz, and K. A. Müller, *Possible high T_c superconductivity in the Ba-La-Cu-O system*, Z. Phys. B **64**, 189-193 (1986).

[22] A. Schilling, M. Cantoni, J. D. Guo, and H. R. Ott, *Superconductivity above 130 K in the Hg-Ba-Ca-Cu-O system*, Nature **363**, 56-58 (1993).

[23] Y. Kamihara, T. Watanabe, M. Hirano, and H. Hosono, *Iron-based layered superconductivity $La[O_{1-x}F_x]FeAs$ (x=0.05-0.12) with T_c = 26 K"*, Jour. Chem Soc. **130**, 3296-3297 (2008).

[24] J. Hubbard, *Electron correlations in narrow energy bands*, Proc. Roy. Soc. A **276**, 238 (1963).

[25] Defense Sciences Office, *Optical Lattice Emulator (OLE) Project*, http://www.darpa.mil/Our_Work/DSO/Programs/Optical_Lattice_Emulator_(OLE).aspx (2013).

[26] M. Yamashita, *Optical lattice*, Poster presentation (2011). http://www.brl.ntt.co.jp/group/ryousei-g/topics-img/Optical_Lattice_2-yamashita.png

[27] M. O. Scully, and M. S. Zubairy, *Quantum optics*, Cambridge (2008).

[28] M. Greiner, *Ultracold quantum gases in three-dimensional optical lattice potentials*, Ph.D thesis, Ludwig-Maximilians-Universität München (2003).

[29] G. Grosso, and G. P. Parravinci, *Solid State Physics*, Elsevier (2000).

[30] D. Jaksch, *Bose-Einstein Condensation and Applications*, Ph.D thesis, Universität Innsbruck (1999).

[31] C. Chin, R. Grimm, P. Julienne, E. Tiesinga, *Feshbach resonances in ultracold gases*, Rev. Mod. Phys. **82**, 1225 (2010).

[32] S. Trotzky, L. Pollet, F. Gerbier, U. Schnorrberger, I. Bloch, N. V. ProkofÕev, B. Svistunov, and M. Troyer, *Suppression of the critical temperature for superfluidity near the Mott transition*, Nature Physics **6**, 998-1004 (2010)

[33] M. Greiner, O. Mandel, T. Esslinger, T. W. Hänsch, and I. Bloch, *Quantum phase transition from a superfluid to a Mott insulator in a gas of ultracold atoms*, Nature **415**, 39-44 (2002).

[34] M. P. A. Fisher, P. Weichman, G. Grinstein, and D. S. Fisher, *Boson localization and the superfluid-insulator transition*, Phys. Rev. B **40**, 546 (1989).

[35] N. Gernelke, X. Zhang, C-L. Hung, and C. Chin, *In situ observation of incompressible Mott-insulating domains in ultracold atomic gases*, Nature **460**, 995 (2009).

[36] J. F. Sherson, C. Weitenberg, M. Endres, M. Cheneau, I. Bloch, and S. Kuhr, *Single-atom-resolved fluorescence imaging of an atomic Mott insulator*, Nature **467**, 68 (2010).

[37] S. Fang, C-M. Chung, P. N. Ma, P. Chen, and D-W. Wang, *Quantum criticality from in situ density imaging*, Phys. Rev. A **83**, 031605 (2011).

[38] D. Jaksch, C. Bruder, J. I. Cirac, C. W. Gardiner, and P. Zoller, *Cold bosonic atoms in optical lattices*, Phys. Rev. Lett. **81**, 3108 (1998).

[39] R. Staudt, M. Dzierzawa, and A. Muramatsu *Phase diagram of the three-dimensional Hubbard model at half filling*, Eur. Phys. Jour. B **17**, 411-415 (2000).

[40] R. Jördens, N. Strohmaier, K. Günter, H. Moritz, and T. Esslinger, *A Mott insulator of fermionic atoms in an optical lattice*, Nature **455**, 204-207 (2008).

[41] N. V. Prokof'ev, B. V. Svistunov, and I. S. Tupitsyn, *Exact, complete, and universal continuous-time worldline Monte Carlo approach to the statistics of discrete quantum systems*, Sov. Phys. JETP **87**, 310 (1998).

[42] L. Pollet, K. V. Houcke, and S. M. A. Rombouts *Engineering local optimality in Quantum Monte Carlo algorithms* J. Comp. Phys. **225/2**, 2249-2266 (2007).

[43] A. L. Fetter, and J. D. Walecka, *Quantum theory of many-particle systems*, Dover (2003).

[44] J. R. Norris, *Markov chains*, Cambridge University Press (1998).

[45] M. Taboga, *Lecture on probability theory and mathematical statistics*, Createspace (2012).

[46] N. Metropolis, A. W. Rosenbluth, M. N. Rosenbluth, A. H. Teller, and E. Teller, *Equation of state calculations by fast computing machines*, Jour. Chem. Phys. **21**, 1087 (1953).

[47] P. N. Ma, L. Pollet, and M. Troyer, *Measuring the equation of state of trapped ultracold bosonic systems in an optical lattice with in-situ density imaging*, Phys. Rev. A **82**, 033627 (2010).

[48] I. Bloch, J. Dalibard, and W. Zwerger, *Many body physics with ultracold gases*, Rev. Mod. Phys. **80**, 885 (2008).

[49] Q. Zhou, and T-L. Ho, *Universal thermometry foe quantum simulation*, Phys. Rev. Lett. **106**, 225301 (2011).

[50] Q. Zhou, Y. Kato, N. Kawashima, and N. Trivedi, *Direct mapping of the finite temperature phase diagram of strongly correlated quantum models*, Phys. Rev. Lett. **103**, 085701 (2009).

[51] P. N. Ma, L. Pollet, and M. Troyer, *Fast implemention of the directed worm algorithm for optical lattices*, in preparation (2013).

[52] P. N. Ma, S. Pilati, M. Troyer, and X. Dai, *Density functional theory for atomic Fermi gases*, Nature Phys. **8**, 601 (2012).

[53] P. Hohenberg, and W. Kohn, *Inhomogeneous electron gas*, Phys. Rev **136**, B864 (1964).

[54] W. Kohn, and L. J. Sham, *Self-consistent equations including exchange and correlation effects*, Phys. Rev. **140**, A1133 (1965).

[55] F. A. Cotton, *Chemical applications of group theory*, Wiley (1990).

[56] A. Georges, G. Kotliar, W. Krauth and M. J. Rozenberg, *Dynamical mean-field theory of strongly correlated fermion systems and the limit of infinite dimensions*, Rev. Mod. Phys. **68**, 13-125 (1996).

[57] M. Fowler, *Historical beginnings of theories of electricity and magnetism*, http://galileo.phys.virginia.edu/classes/109N/more_stuff/E&M_Hist.pdf, Uni. Virginia (1997).

[58] A. Einstein, *Zur Elektrodynamik bewegter Körper*, Ann. Phys. **322**, 891-921 (1905).

[59] K. Yosida, *Theory of magnetism*, Springer (1998).

[60] G. B. Jo, Y. R. Lee, J. H. Choi, C. A. Christensen, T. H. Kim, J. H. Thywissen, D. E. Pritchard, and W. Ketterle, *Itinerant ferromagnetism in a Fermi gas of ultracold atoms*, Science **325**, 1521 (2009).

[61] P. N. Ma, L. Pollet, and M. Troyer, *Simulating the boson Hubbard model using QMC Directed-Worm-Algorithm (DWA) code* The ALPS project, http://alps.comp-phys.org/mediawiki/index.php/ALPS_2_Tutorials:MC-09_Directed_Worm_Algorithm (2013).

[62] G. E. Astrakharchik, J. Boronat, J. Casulleras, and S. Giorgini, *Equation of state of a Fermi gas in the BEC-BCS crossover: A quantum Monte Carlo study*, Phys. Rev. Lett. **93**, 200404 (2004).

[63] S.Y.- Chang, V. R. Pandharipande, J. Carlson, and K. E. Schmidt, *Quantum Monte Carlo studies of superfluid Fermi gases*, Phys. Rev. A **70**, 043602 (2004).

[64] J. Carlson, and S. Reddy, *Asymmetric two-component fermion systems in strong coupling*, Phys. Rev. Lett **95**, 060401 (2005).

[65] C. Lobo, A. Recati, S. Giorgini, and S. Stringari, *Normal state of a polarized Fermi gas at unitarity*, Phys. Rev. Lett **97**, 200403 (2006).

[66] S. Pilati, and S. Giorgini, *Phase separation in a polarized Fermi gas at zero temperature*, Phys. Rev. Lett. **100** (030401) (2008).

[67] N. Navon, S. Nascimbene, F. Chevy, and C. Salomon, *The equation of state of a low-temperature Fermi gas with tunable interactions*, Science **328**, 729-732 (2010).

[68] S. Nascimbène, *et al. Fermi-liquid behavior of the normal phase of a strongly interacting gas of cold atoms.* Phys. Rev. Lett. **106**, 215303 (2011).

[69] W. M. C. Foulkes, L. Mitas, R. J. Needs and G. Rajagopal, *Quantum Monte Carlo simulations of solids*, Rev. Mod. Phys. **73**, 33-83 (2001).

[70] S. Pilati, G. Bertaina, S. Giorgini, and M. Troyer, *Itinerant ferromagnetism of a repulsive atomic Fermi gas: A Quantum Monte Carlo study*, Phys. Rev. Lett. **105**, 030405 (2010).

[71] K. Huang, and C. N. Yang, *Quantum-mechanical many-body problem with hard-sphere interaction*, Phys. Rev. **105**, 767-775 (1957).

[72] T. D. Lee, and C. N. Yang, *Many-body problem in quantum mechanics and quantum statistical mechanics*, Phys. Rev. **105**, 1119-1120 (1957).

[73] R. A. Duine, and A. H. MacDonald, *Itinerant ferromagnetism in an Ultracold atom Fermi gas*, Phys. Rev. Lett. **95**, 230403 (2005).

[74] A. Recati, and S. Stringari, *Spin fluctuations, susceptibility, and the dipole oscillation of a nearly ferromagnetic fermi gas*, Phys. Rev. Lett. **106**, 080402 (2011).

[75] S. Kanno, *Criterion for the ferromagnetism of hard sphere fermi liquid*, Prog. Theo. Phys. **44**, 813-815 (1970).

[76] C. Mora, and F. Chevy, *Normal phase of an imbalanced Fermi gas*, Phys. Rev. Lett. **104**, 230402 (2010).

[77] X. Cui, and H. Zhai, *Stability of a fully magnetized ferromagnetic state in repulsively interacting ultracold Fermi gases*, Phys. Rev. A **81**, 041602 (2010).

[78] A. Recati, *Private communication*, (2010).

[79] S. Pilati, and M. Troyer, *Bosonic superfluid-insulator transition in continuous space*, Phys. Rev. Lett. **108**, 155301 (2012).

List of Publications

1. **P. N. Ma**, *Numerical simulations of bosons and fermions in three dimensional optical lattices*, Ph.D thesis, ETH Zurich (2013).

2. **P. N. Ma**, S. Pilati, M. Troyer, and X. Dai, *Density functional theory for atomic Fermi gases*, Nature Phys. **8**, 601 (2012).

3. B. Bauer, et al. (ALPS Collaboration), *The ALPS project release 2.0: open source software for strongly correlated systems*, Jour. Stat. Mech: Theo. and Expt. **2011**, P05001 (2011).

4. S. Fang, C-M. Chung, **P. N. Ma**, P. Chen, and D-W. Wang, *Quantum criticality from in situ density imaging*, Phys. Rev. A **83**, 031605 (2011).

5. **P. N. Ma**, L. Pollet, and M. Troyer, *Measuring the equation of state of trapped ultracold bosonic systems in an optical lattice with in-situ density imaging*, Phys. Rev. A **82**, 033627 (2010).

6. **P. N. Ma**, *Numerical exact simulations of actual-size bosonic optical lattice systems*, M. Phil thesis, HKU (2009).

7. **P. N. Ma**, K. Y. Yang, L. Pollet, J. V. Porto, M. Troyer, and F. C. Zhang, *Influence of the trap shape on the detection of the superfluid-Mott-insulator transition*, Phys. Rev A **78**, 023605 (2008).

8. **P. N. Ma**, L. Pollet, M. Troyer, and F. C. Zhang, *A classical picture of the role of vacancies and interstitials in Helium-4*, J. Low. Temp. Phys. **152** 156-163 (2007).

Curriculum Vitae

Personal Data

Name:	Ping Nang MA
Date of birth:	May 27, 1982 (Hong Kong)
Nationality:	Hong Kong
Marital status:	Divorced
First language:	English, Chinese
Foriegn language:	German

Education

2009-2013	Ph.D. (Computational Physics) Supervisor: Prof. Matthias Troyer	Theoretishe Physik, ETH Zurich
2007-2009	M.Phil (Theoretical Physics) Supervisor: Prof. Fu Chun Zhang	Hong Kong University
2004-2007	B.Sc. Hon. (Physics/ Chemistry)	Hong Kong University
2000-2001	GCE A. Levels	Victoria Junior College, Singapore
1996-1999	GCE O. Levels	Anglican High School, Singapore

Experience

2001-2004	Combat military service in the Singapore Armed Forces

Acknowledgements

Venturing into the research frontier of quantum engineering truly gives me an exciting sense of satisfaction, especially when our research becomes directly relevant to the scientific community in their quest towards the unknown. This opportunity could not be made possible for me without my respectable supervisor, Prof. Matthias Troyer. His ambient guidance has cultivated both my thinking and knowledge over these years, and I am deeply influenced by his humble character in the acquisition of knowledge. I have benefited tremendously from his vast experience in computer science, particularly in appreciating the art of modern programming.

An equivilently important person who has influenced my life is my former supervisor, Prof. Fu Chun Zhang. Perhaps my interest for strongly correlated physics started with his motivating lectures on quantum mechanics during my undergraduate studies. Indebted to his generous opportunity to send me here at ETH Zurich in 2006, my entire vision of numerics and scientific computing had since widened and resulted in my love for them. Without his support all these years, I would not be whom I am today. Here, I want to reemphasize my appreciation for him as my role model in scientific research.

Special appreciation is given to my closest collaborators: Prof. Lode Pollet, who selflessly imparts the essence of QMC directed wom algorithm to me; and Dr. Sebastiano Pilati, who shares his vast knowledge in diffusion Monte Carlo with me. Special thanks are given to Prof. Xi Dai who shares with me his experience of working with DFT electronic structure calculations. Not to forget my bosonic collaborators in the earlier days, who include Prof. Daw-Wei Wang, Prof. Po-Chung Chen, Shiang Fang, and Chia-Ming Chung. Fruitful discussions with Prof. T-L. Ho, and Dr. Qi Zhou, on thermometry concepts; Prof. Phillip Werner, Prof. Takashi Oka, Dr. Naoto Tsuji, and Dr. Lei Wang, on diagrammatic corrections beyond DFT, are deeply appreciated.

Academic visits cannot be made possible without certain important people. I

would like to express my deepest gratitudes to Prof. Immanuel Bloch for inviting me to the Max Planck Institute, Prof. Hideo Aoki to Tokyo University, Prof. Fu Chun Zhang to Hong Kong University, Prof. Xi Dai to the Chinese Academy of Science, Prof. Daw-Wei Wang to the National Center for Theoretical Sciences of Taiwan, and Prof. Jian-Sheng Wang to the National University of Singapore. Special thanks are also given to Prof. Dielthem Wurtz for inviting me twice to his financial engineering workshop in Meielisalps, whom I met there Dominik Locher and Yangyang.

Sincere gratitudes are expressed to my German tutors, Paulina Velasco, Andreas Hehn, and Lea Kraemer (in addition for her help with the Zusammenfassung in this thesis). In addition, Dr. Phillip Carboz, Dr. Bela Bauer, Jan Gukelberger, and Michele Dolfi have helped me a lot with administrative issues that pop up unexpectedly during my academic research. It is worth also mentioning Dr. Zhenya Kozik, Dr. Juan Carlos, and Dr. Peter Anders for bringing so much fun to my research in the earlier days. Here, I want to express my thanks to all present colleagues at ETH Zurich, as well as all former colleagues at Hong Kong University, for shaping me into whom I am today.

This scientific research can not be possible with the funding from Swiss National Foundation and ETH Zurich. Besides, I must also thank the Brutus cluster of ETH Zurich as well as its support team for working so hard for my project with thousands of CPU processors.

Last but not least, I have to express my gratitude to my parents who gave me such wonderfully intelligent genes. Their love and support have always been with me since my very first day on Earth. And how could I dare to forget you, Yangyang, the only one whom I love most? Yes, that's right! You are most appreciated.